

# Numerical Simulations of Subcritical and Supercritical Flows in Shallow Waters

Shooka Karimpour Ghannadi

Doctor of Philosophy

Department of Civil Engineering and Applied Mechanics

McGill University

Montreal, Quebec

2015-03-20

A thesis submitted to McGill University in partial fulfilment of the requirements  
for the degree of Doctor of Philosophy

©Copyright Shooka Karimpour Ghannadi 2015

## DEDICATION

To my family.

## ACKNOWLEDGEMENTS

First, I wish to express my deep gratitude to my supervisor, Professor Vincent H. Chu, for guidance, dedication during the course of this research, and for believing in my analytical and numerical skills.

I would like to acknowledge the funding provided by the Brace Water Resources. I also like to thank members of staff in Department of Civil Engineering and Applied Mechanics who provided constant technical and administrative support during my graduate study. I specially want to thank Professor Babarutsi for support and encouragement in the past years.

My deep gratitude goes to my parents and my brothers who always have had faith in me throughout my life and continually supported me during my studies.

Finally, to my husband, Navid, it is difficult to express my appreciation because it is so boundless. The completion of this thesis was possible with your unfailing love, support and understanding.

## ABSTRACT

The formation of shock waves as the currents make transition from supercritical to subcritical flow are common in many environmental science and hydro-technical engineering applications. The numerical challenge for simulation of the supercritical-to-subcritical flow transitions is capturing the depth and velocity discontinuity across the shock waves. Total Variation Diminishing (TVD) methods are one of the most conventional methods to manage the spatial integrations in the vicinity of large gradients. TVD methods however are limited to no more than second or third order of accuracy. There are on the other hand Essentially Non-Oscillatory (ENO) schemes that can be extended to have infinite order of accuracy. ENO compared to the conventional TVD schemes reduces the computational effort with minimum undesirable numerical dissipation. In this thesis a Finite Volume Method (FVM) is developed to simulate subcritical and supercritical flows in shallow waters. The performance of a large numbers of shock capturing strategies is evaluated through grid-refinement studies and comparison with available analytical solutions. The investigation for shock-capturing capability of the numerical scheme in supercritical to subcritical transition has been carried out for (i) The transverse dam-break wave, (ii) the linear development of shear instability and (iii) the non-linear transition to turbulence in shallow water.

The first application of the numerical method is the diversion of water from a main channel to the side through a weir. Calculations have been conducted for subcritical to supercritical approaching main flows with Froude numbers ranging from

$Fr_o = 0.03$  to  $2.0$ . Results are presented in the framework of the classical solution of Ritter's. In the limiting case of supercritical main flow, the results are consistent with Prandtl-Meyer expansion, developed originally for gas dynamics. The results obtained over the entire range of Froude numbers are presented in a unified manner for comparison with available experimental data.

Using this numerical method, hydrodynamic instability investigation is conducted without making the assumption of the normal mode. The direct numerical simulation for this problem has been carried out for a base flow with hyperbolic tangent velocity profile, covering a range of convective Froude numbers from  $0.1$  to  $2.0$ . The results obtained from simulation of the subcritical shallow waters are consistent with the analogous instability studies previously considered in gas dynamics. The supercritical instability on the other hand is associated with entrapment and radiation of waves that are beyond the classical description of the normal mode.

The direct numerical simulations allow the continuation of the stability calculation to the non-linear stage of development. The analyses have shown how the presence of shock waves can influence the formation of eddies and shocklets. Reduced mixing layer growth is in agreement with the experimental investigation in gas dynamics. Furthermore in the simulation of the non-linear instability and the study of energy dissipation, shock waves are observed at intermediate convective Froude number of  $0.75$ . Investigation also suggests a drastic drop of lateral to longitudinal velocity fluctuation with rise in Froude number.

Grid refinement studies for convergence to analytical solution and the validation of the numerical method using available experimental data are carried out in

the implementation of the numerical method to the three fundamental problems considered in this thesis. These convergence studies have shown the numerical calculations across the sharp gradients can be managed to gain the needed computational stability and produce results approaching the accuracy of analytical methods.

## ABRÉGÉ

La formation d'ondes de choc issue des courants en transition d'un écoulement fluvial supercritique à un coulement souscritique est commune à plusieurs sciences de l'environnement et applications de génie hydro-technique. Le défi numérique pour la simulation des transitions de flux supercritiques à sous-critiques est la capture des discontinuités en profondeur et en vitesse des ondes de choc. Les méthodes de diminution de variation totale (TVD ou Total Variation Diminishing) est l'une des méthodes classiques pour gérer les intégrations spatiales dans le voisinage des gradients importants. Cependant, les méthodes TVD sont limitées à un niveau de précision de second ou troisième ordre sans plus. Des systèmes essentiellement non-oscillants (ENO ou Essentially Non-Oscillatory), par contre, peuvent être prolongés afin d'obtenir un calibre de précision infini. Par rapport aux régimes de TVD classiques, ENO réduit l'effort de calcul avec une dissipation numérique indésirable minimale. Dans cette thèse une méthode en volume finis (FVM) a été développée pour simuler les écoulements fluviaux et torrentiels dans les eaux peu profondes. Un grand nombre de stratégies de capture de choc a été effectué et évalué à travers une grille de raffinement constituée à partir d'études et de comparaisons avec les solutions analytiques disponibles. L'enquête sur la capacité de la méthode numérique à capturer le choc dans la transition supercritique à sous-critique a été réalisée pour (i) L'onde transversale de rupture de barrage, (ii) le développement linéaire de l'instabilité de cisaillement et (iii) la transition non-linéaire à la turbulence en eau peu profonde.

La première application de la méthode numérique est le détournement de l'eau

d'un canal principal par le moyen d'un déversoir. Les calculs ont été effectués pour l'approche de flux principaux sous-critiques à supercritiques avec des nombres de Froude allant de  $Fr_o = 0.03$  à  $2.0$ . Les résultats sont présentés dans le cadre de la solution classique de Ritter. Dans le cas limite de l'écoulement principal supercritique, les résultats sont cohérents avec l'expansion de Prandtl-Meyer, développée à l'origine pour la dynamique des gazs. Les résultats obtenus sur toute la plage de nombres de Froude sont présentés d'une manière unifiée afin d'être comparés avec les données expérimentales disponibles.

En utilisant cette méthode numérique, l'enquête de l'instabilité hydrodynamique est réalisée sans faire l'hypothèse du mode normal. La simulation numérique directe de ce problème a été effectuée pour un débit de base avec une fonction tangente hyperbolique de vitesse, couvrant une gamme de nombres de Froude convectifs de  $0.1$  à  $2.0$ . Les résultats obtenus par la simulation de l'instabilité sous-critique dans les eaux peu profondes sont cohérents avec les études d'instabilité analogues déjà pris en considération dans la dynamique des gazs. L'instabilité supercritique sur la main est associée avec le piégeage et le rayonnement des ondes qui sont au-delà de la description classique du mode normal.

Les simulations numériques directes permettent la poursuite du calcul de la stabilité l'étape non-linéaire du développement. Les analyses ont montré que la présence d'ondes de choc peut influencer la formation de tourbillons et de petits chocs. La croissance réduite de la couche de mélange correspond à l'étude expérimentale de la dynamique des gazs. En outre, dans la simulation de l'instabilité non-linéaire et l'étude de la dissipation d'énergie, les ondes de choc sont observées au nombre

convectif intermédiaire de Froude de 0.75. L'enquête suggère également une baisse drastique de la fluctuation de vitesse latérale à longitudinale avec une hausse du nombre de Froude.

Les études de grille de raffinement pour la convergence à la solution analytique et la validation de la méthode numérique utilisant les données expérimentales disponibles sont réalisées dans la mise en œuvre de la méthode numérique aux trois problèmes fondamentaux considérés dans cette thèse. Ces études de convergence ont démontré que les calculs numériques à travers les gradients saillants peuvent être gérés pour gagner la stabilité de calcul nécessaire et produire des résultats qui approchent la précision des méthodes analytiques.

## TABLE OF CONTENTS

DEDICATION		ii
ACKNOWLEDGEMENTS		iii
ABSTRACT		iv
ABRÉGÉ		vii
LIST OF TABLES		xiii
LIST OF FIGURES		xiv
LIST OF SYMBOLS		xxii
1	INTRODUCTION	1
1.1	Motivations and Objectives	1
1.2	Computational schemes for high-speed shallow waters	4
1.3	Literature Review for Compressible Mixing Layers	7
1.4	Thesis Organization	11
2	HIGH-ORDER INTERPOLATION SCHEMES FOR SHEAR INSTABILITY SIMULATIONS	15
2.1	Abstract	15
2.2	Introduction	16
2.3	Shallow-water Equations	18
2.4	Formulation on Staggered Grid	19
	2.4.1 Interpolation on the Staggered Grid	19
	2.4.2 Flux-Limiting Schemes	23
	2.4.3 Advance in Time by the Runge-Kutta Method	30
2.5	Simulation for the Shear Instabilities	31
	2.5.1 Grid Refinement and Convergence	36
2.6	Nonlinear Development	39

2.7	Summary and Conclusion . . . . .	45
3	TRANSVERSE DAM-BREAK WAVES . . . . .	48
3.1	Abstract . . . . .	48
3.2	Introduction . . . . .	49
3.3	Numerical Simulation . . . . .	51
3.4	Transient Development toward the Steady State . . . . .	53
	3.4.1 1D Dam-break Waves of Ritter . . . . .	56
	3.4.2 Discharge Coefficient of the 2D TDWs . . . . .	57
3.5	Transverse Dam-break Waves on a Flat Bed in Steady State . . . . .	59
	3.5.1 Prandtl-Meyer Expansion for TDWs with $Fr_o > 1$ . . . . .	61
	3.5.2 Prandtl-Meyer Expansion in Terms of Ritter's Similarity Variable . . . . .	63
	3.5.3 Transverse Dam-break Waves for Subcritical Main Flow . . . . .	64
3.6	Discharge Coefficient over Weir and Flat Bed . . . . .	64
	3.6.1 Discharge Coefficient for Diversion over Weir . . . . .	66
	3.6.2 Laboratory Experimental Investigation . . . . .	67
3.7	Conclusion . . . . .	68
4	LINEAR INSTABILITIES IN SHALLOW FLOW . . . . .	69
4.1	Abstract . . . . .	69
4.2	Introduction . . . . .	70
4.3	Direct Numerical Simulation . . . . .	72
4.4	Fractional Growth Rate . . . . .	76
4.5	Constant Structure of Subcritical Instabilities . . . . .	77
4.6	Consistent Structure for Supercritical Instabilities . . . . .	78
4.7	Entrapment and Radiation of Waves . . . . .	84
4.8	Summary and Conclusion . . . . .	88
	Appendix: Numerical Computation . . . . .	89
5	WAVE AND ENERGY DISSIPATION IN SUBCRITICAL AND SUPERCRITICAL MIXING LAYERS . . . . .	91
5.1	Abstract . . . . .	91
5.2	Introduction . . . . .	92
5.3	Formulation and Numerical Methods . . . . .	93
5.4	General Results . . . . .	95
5.5	Mixing Layer and Growth . . . . .	99

5.6	Kinetic and Potential Energy . . . . .	104
5.7	Disturbance Kinetic Energy . . . . .	110
5.8	Anisotropy . . . . .	117
5.9	Conclusion . . . . .	119
6	CONCLUSION . . . . .	121
6.1	Contributions to Knowledge . . . . .	122
6.2	Recommendations to Future Work . . . . .	123
	REFERENCES . . . . .	124

LIST OF TABLES

<u>Table</u>	<u>page</u>
2-1 DWF formulae in the non-monotonic ( $NV < 1$ ), monotonic ( $0 < NV < 1$ ) and non-monotonic ( $NV > 1$ ) regions for the six flux-limiting strategies; Co = Courant number . . . . .	26
2-2 Grid size, fractional error and order of convergence obtained from the simulations of the linear shear instabilities using the 5 <sup>th</sup> -order WENO, 3 <sup>rd</sup> -order ULTRA-QUICK and 2 <sup>nd</sup> -order MINMOD. The boldface numbers in the table are the values obtained from the extrapolation to $\Delta x \rightarrow 0$ . . . . .	37
2-3 Grid size, fractional error and order of convergence obtained for the momentum thickness from simulations of nonlinear shear instabilities using 5 <sup>th</sup> -order WENO, 3 <sup>rd</sup> -order ULTRA-QUICK and 2 <sup>nd</sup> -order MINMOD. The boldface numbers in the table are the values obtained from the extrapolation to $\Delta x \rightarrow 0$ . . . . .	44
4-1 The level of normal disturbance kinetic energy growth. The initial disturbance perturbs depth at a magnitude of $h'/\delta_{\omega o} = 1E-10$ . For the supercritical $Fr_c = 1.4$ , it takes about $t\hat{U}_y = 250$ to reach the linear consistent structure. . . . .	75
4-2 The convergence of averaged growth rate $\bar{\alpha}/\hat{U}_y$ . . . . .	90
5-1 Specification of direct numerical simulation databases: convective Froude number, domain and grid size. . . . .	94

LIST OF FIGURES

<u>Figure</u>	<u>page</u>
1-1 The main stencil and three substencils arrangement in 5 <sup>th</sup> order WENO scheme by Shu (2009). . . . .	7
1-2 Supercritical expansion fan formation in $Fr_o = 0.48$ and $1.92$ , reported in chapter 3. . . . .	13
2-1 (a) finite volume for the calculation of $h_{(i,j)}$ using the continuity equation, (b) finite volume for the calculation of $q_{x(i,j)}$ using the $x$ -momentum equation, (c) finite volume for the calculation of $q_{y(i,j)}$ using the $y$ -momentum equation, (d) locations where nonlinear fluxes $(\mathcal{F}_{(i,j)}^{uq_x}, \mathcal{F}_{(i,j)}^{vq_x}, \mathcal{F}_{(i,j)}^{uq_y}, \mathcal{F}_{(i,j)}^{vq_y})$ and depths $(h_{(i,j)}^{q_x}, h_{(i,j)}^{q_y})$ are determined by interpolation. . . . .	20
2-2 The $uu$ -node, $u$ -node, $c$ -node, $d$ -node and $dd$ -node used in the upwinding interpolation for value $\phi_f$ between the $c$ -node and $d$ -node.	22
2-3 The DWF-NV diagram of Leonard & Mokhtari (1990) delineating the monotonic region and its relation in the diagram to various interpolation schemes including FOU, CD, SOU, FOD and QUICK. The thick solid line defines the flux limiter ULTRA-QUICK. . . . .	24
2-4 The TVD region (gray) in the DWF- $\Theta$ diagram of Sweby (1984). The upper boundary of TVD region is SUPERBEE and the lower boundary is MINMOD. . . . .	27
2-5 (a) Computational domain for simulation of the shear instabilities with periodic boundary condition in $x$ direction and radiating boundary conditions at $y = -5\lambda_x$ and $y = +5\lambda_x$ . (b) TANH velocity profile. . . . .	32

2-6	(a) Contours of the disturbances' kinetic energy $K'/\overline{K'}$ on the $x$ - $y$ plane obtained for $k_x = 0.893$ and $\text{Fr}_c = 0.1$ at $t\hat{U}_y = 75$ in the initial stage, when the development is governed by linear equations. (b) The growth of $\sqrt{\overline{K'}}/(U_1 - U_2)$ with time $t\hat{U}_y$ on a semi-logarithmic scale. The red portion of the line delineates the fractional growth rate $\alpha$ . Results are obtained for $\lambda_x/\Delta x = 128$ , using 5 <sup>th</sup> -order WENO reconstruction scheme. . . . .	34
2-7	The growth rate $\alpha/\hat{U}_y$ versus wave number $k$ in the linear stage of the shear-layer development for $\text{Fr}_c = 0.1$ ( $\circ$ ) and $\text{Fr}_c = 0.8$ ( $\Delta$ ). Results for $\text{Fr}_c = 0.1$ and $0.8$ are obtained for $\lambda_x/\Delta x = 128$ and $256$ respectively, using 5 <sup>th</sup> -order WENO reconstruction scheme. The open symbols represent current numerical simulation and dashed lines are the linear stability analysis obtained for compressible gas for convective Mach numbers $\text{Ma}_c = 0.01$ and $\text{Ma}_c = 0.8$ by Sandham & Reynolds (1990). . . . .	35
2-8	The convergence of the maximum growth rate $\hat{\alpha}$ at the wave number $k_x = 2\pi\delta_{\omega o}/\lambda_x = 0.51$ for $\text{Fr}_c = 0.8$ (top row), and the maximum rate $\hat{\alpha}$ at $k_x = 0.89$ for $\text{Fr}_c = 0.1$ (bottom row). The fractional errors are plotted versus the grid size for the fifth-order WENO (left), third-order ULTRA-QUICK (centre) and second-order MINMOD (right) schemes. . . . .	40
2-9	The maximum growth of the instability to form an eddy at $k_x = 0.89$ for $\text{Fr}_c = 0.1$ . (a) Disturbance kinetic energy ( $\sqrt{\overline{K'}}/(U_1 - U_2)$ ) versus time $t\hat{U}$ in semi-logarithmic scale. (b) Momentum Thickness, $\delta_\theta/\delta_{\theta o}$ . (c) Vorticity contour on the $x$ - $y$ plane at the times $t_1$ , $t_2$ and $t_3$ as marked in (b) of the figure. The first pinnacle of the momentum thickness $\hat{\delta}_\theta$ in the nonlinear stage occurs at time $t_3$ . . . . .	41
2-10	The maximum growth of the instability to produce a shocklet at $k_x = 0.51$ for $\text{Fr}_c = 0.8$ . (a) Disturbance kinetic energy ( $\sqrt{\overline{K'}}/(U_1 - U_2)$ ) versus time $t\hat{U}$ in semi-logarithmic scale. (b) Momentum Thickness $\delta_\theta/\delta_{\theta o}$ . (c) Vorticity contour on the $x$ - $y$ plane at the times $t_1$ , $t_2$ and $t_3$ as marked in (b) of the figure. Shock waves with a sudden jump in depth and velocity are observed in the shocklet as the momentum thickness reaches its first pinnacle at time $t_3$ . . . . .	42

- 2–11 The convergence of the nonlinear simulation for the momentum thickness by five progressively less accurate interpolation schemes. From the left to right in the figure are the results obtained by WENO, QUICK, ULTRA-QUICK, SUPERBEE, MINMOD. The top row shows results for  $Fr_c = 0.8$  and the bottom row for  $Fr_c = 0.1$ . 46
- 3–1 Transverse dam-break waves over a length of  $L$  on the side of the open-channel main flow. (a) The arrows show the velocity vector  $(u, v)$ . The sharp change in dilation  $(\partial u/\partial x + \partial v/\partial y)$  from blue to red marks the hydraulics jump as the outflow changes from supercritical to subcritical. The flow pattern shown is obtained from a simulation for the main-flow Froude number  $Fr_o = 0.63$ . The length along the opening of the supercritical outflow upstream of the jump is  $L_{super}$ . The length of the subcritical outflow is  $L_{sub}$ . (b) Cross-sectional profile of water depth and bottom elevation over a weir of height  $H_w$  and width  $W_w$ . . . . . 50
- 3–2 Transient development of TDWs on a flat bed for  $Fr_o = 0.03$  over the period from time  $t/t_s = 0.25$  to 3.00. (a) The depth and (b) lateral discharge (bottom left) profiles are obtained at the center of the opening where  $x = L/2$ . The contour lines in the images (c) define the local Froude number  $Fr = \sqrt{u^2 + v^2}/\sqrt{gh}$ . The red color marks the region of the supercritical flow ( $Fr > 1$ ). . . . . 54
- 3–3 Transient development of TDWs on a flat bed for  $Fr_o = 0.63$  over the period from time  $t/t_s = 0.25$  to 3.00. (a) The depth and (b) lateral discharge (bottom left) profiles are obtained at the center of the opening where  $x = L/2$ . The contour lines in the images (c) define the local Froude number  $Fr = \sqrt{u^2 + v^2}/\sqrt{gh}$ . The red color marks the region of the supercritical flow ( $Fr > 1$ ). . . . . 55
- 3–4 The discharge coefficient,  $Q^*(t, Fr_o)$ , and its dependence on the time  $t/t_s$  and on the main-flow Froude number  $Fr_o$ : (a) subcritical main flow with  $Fr_o < 1$ , (b) supercritical main flow with  $Fr_o > 1$ . The flow is considered to have reached steady state at time  $t = 10 t_s$  as the total flow rate  $Q^*$  has closely approached its asymptote at this time. . . . . 58

3–5	The TDWs on a flat bed at the steady state when time $t = 10t_s$ . The main-flow Froude numbers are (a) $Fr_o = 0.03$ , (b) $Fr_o = 0.48$ , (c) $Fr_o = 0.80$ , (d) $Fr_o = 1.00$ , (e) $Fr_o = 1.28$ and (f) $Fr_o = 1.92$ . The contour values are the local Froude numbers. Dashed lines in (d), (e) and (f) indicate the “Froude line” between the undisturbed main flow and the diversion expansion fan. . . . .	60
3–6	The length fraction $L_{\text{super}}/L$ of the supercritical flow expansion. . . .	61
3–7	Depth $h$ -profile (left) and lateral discharge $q_y$ -profile (right) of the TDWs in the steady state for (a) $Fr_o = 3.2$ , (b) $Fr_o = 1.0$ and (c) $Fr_o$ $= 0.48$ . The dashed lines and the solid lines are the Prandtl-Meyer profiles for the limiting cases of $Fr_o = 1$ and $Fr_o \rightarrow \infty$ , respectively.	62
3–8	Dependence of steady-state discharge coefficient on the main-flow Froude number. The solid symbols denote the discharge coefficient obtained from the simulations over a flat bed. The open symbols denote the simulated outflow over weirs of $W_w/H_w = 16, 8$ and $4$ , respectively. The solid line is the Prandtl-Meyer solution for the expansion. The + symbol represents the laboratory data obtained by Mizumura <i>et al.</i> (2003). The red dashed lines are the empirical Equations (3.12) and (3.13) derived from laboratory experiments over a sharp-crested weir by Subramanya & Awasthy (1972). . . . .	65
4–1	(a) TANH base-flow velocity profile. (b) Computational domain defined in the $x$ -direction from $x = 0$ to $\lambda_x$ and in the lateral $y$ -direction from $y = y^-$ to $y = y^+$ . The dashed lines mark the returning surfaces where the current speed matches the gravity-wave speed. . . . .	71
4–2	The growth of the perturbations’ kinetic energy, $\overline{K'}/(U_1 - U_2)$ , with time $t\hat{U}_y$ on the semi-logarithmic scale for (a) subcritical instabilities with $Fr_c = 0.95$ , $k_x = 2\pi/\lambda_x = 0.40$ (b) supercritical instabilities with $Fr_c = 1.2$ , $k_x = 0.35$ and (c) supercritical instabilities with $Fr_c = 1.4$ , $k_x = 0.35$ . The fractional growth rates are respectively $\alpha/\hat{U}_y = 0.0407$ and $\bar{\alpha}/\hat{U}_y = 0.01365, 0.0094$ . . . . .	74

4-3	Disturbance potential energy to kinetic energy ratio $(\overline{P'}/H\overline{K'})$ for (a) $Fr_c = 0.95$ , $k_x = 2\pi/\lambda_x = 0.40$ , (b) $Fr_c = 1.2$ , $k = 0.35$ and (c) $Fr_c = 1.4$ , $k_x = 0.35$ . The dashed and solid lines in (b) and (c) represent the results obtained from two computational domain sizes of $y^+ = -y^- = \lambda_x$ and $y^+ = -y^- = 2\lambda_x$ , respectively. . . . .	75
4-4	(a) vorticity fluctuation $\zeta'\delta_{\omega o}/\sqrt{\overline{K'}}$ and (b) disturbance kinetic energy $\overline{K'}/\overline{K'}$ for the subcritical instability with $Fr_c = 0.7$ , $k_x = 0.60$ . . . . .	78
4-5	Fractional growth rate of the subcritical instability obtained from DNS for two convective Froude numbers $Fr_c = 0.1$ and $0.8$ . The dashed lines are the results obtained from for convective Mach number $Ma_c = 0.01$ and $0.8$ by Sandham and Reynolds (1990) for ideal gas. . . . .	79
4-6	Averaged fractional growth rate $\overline{\alpha}/\hat{U}_y$ of the supercritical instability for convective Froude numbers $Fr_c = 1.2, 1.4$ . The dashed line is the relation for the ideal gas with the Mach number of $Ma_c = 1.2$ obtained by Sandham and Reynolds (1990). . . . .	79
4-7	(a) Lateral vorticity fluctuation profiles, $\zeta'\delta_{\omega o}/\sqrt{\overline{K'}}$ , at $x = \lambda_x/4, \lambda_x/2, 3\lambda_x/4$ and $\lambda_x$ ; and (b) lateral profile for the disturbance kinetic energy, $\overline{K'}/\overline{K'}$ (blue solid line) and normal reynold's stress $\overline{u'u'}/2\overline{K'}$ (dashed line), of the supercritical instability at $Fr_c = 1.40$ and $k_x = 0.35$ at $\frac{1}{4}T$ (top), $\frac{1}{2}T$ (top-centre) and $\frac{3}{4}T$ (top-bottom) and $T$ (bottom). The lateral extent of the shear instability over a distance of one vorticity thickness is marked by the black vertical dashed lines. The locations of the returning surfaces at $y/\delta_{\omega o} = \pm 0.147$ is marked by the red vertical dashed lines. . . . .	80
4-8	Lateral distribution of (a) disturbance potential energy $gh' h' /(2H\overline{K'})$ ; (b) disturbance streamwise velocity $u' u' /(2\overline{K'})$ and (c) disturbance lateral velocity $v' v' /(2\overline{K'})$ for $Fr_c = 1.4$ and $k_x = 0.35$ over at $\frac{1}{4}T$ (top), $\frac{1}{2}T$ (top-centre) and $\frac{3}{4}T$ (top-bottom) and $T$ (bottom). Vertical dashed lines define the returning surfaces. The streamwise velocity fluctuation $u' u' /(2\overline{K'})$ inbetween the returning surfaces reaches 1.30, 1.66, 0.96 and 0.06 at $\frac{1}{4}T, \frac{1}{2}T, \frac{3}{4}T$ and $\frac{3}{4}T$ , respectively. . . . .	82

4-9	Ratio of averaged disturbance potential energy to averaged total disturbance kinetic energy ( $\overline{P'}/H\overline{K'}$ ) and its dependence on the convective Froude number. . . . .	83
4-10	The lateral distribution of the wave power $P_y(y, t)/[H\sqrt{gH}\overline{K'}(t - y/\sqrt{gH})]$ for (a) $Fr_c = 0.7$ , $k_x = 0.6$ and (b) $Fr_c = 1.4$ , $k_x = 0.35$ . The blue lines mark the vorticity thickness and the red dashed lines the returning surfaces. . . . .	86
4-11	Radiation at $y = \pm 6\delta_{\omega_0}$ , for $\overline{P}_y(\pm 6\delta_{\omega_0}, t)/[H\sqrt{gH}\overline{K'}(t - 6\delta_{\omega_0}/\sqrt{gH})]$ for (a) $Fr_c = 0.95$ ; (b) $Fr_c = 1.20$ and (c) $Fr_c = 1.4$ . . . . .	86
4-12	Wave radiation power and its dependence on the convective Froude Number. The symbol $\bullet$ defines the averaged value of the normalized power. . . . .	87
4-13	Frequency of the modulation $\omega_M/\hat{U}_y$ and its dependence on the wave number $k_x$ in the waves trapped between the returning surfaces for $Fr_c = 1.2, 1.4$ and $2.0$ . . . . .	88
4-14	Estimated fractional error for the averaged growth rate, $\bar{\alpha}/\hat{U}_y$ , obtained from the calculations of the fractional growth rate for the supercritical instability with convective Froude number equal to $Fr_c = 1.2$ (left) and $Fr_c = 1.4$ (right) at $k_x = 0.35$ . The levels of error at $N = 256$ are 0.03% and 0.33% for $Fr_c = 1.2$ and $1.4$ , respectively. . . . .	89
5-1	Vorticity evolution in the transition from linear to non-linear stages $t_1$ to $t_3$ for (a) $Fr_c = 0.1$ , (b) $Fr_c = 0.8$ and (c) $Fr_c = 1.1$ . . . . .	96
5-2	The relative depth ( $h/H_0$ ) evolution in the transition from linear to non-linear at stages $t_1$ to $t_3$ for (a) $Fr_c = 0.1$ , (b) $Fr_c = 0.8$ and (c) $Fr_c = 1.1$ . . . . .	97
5-3	Evolution of local Froude number over transition from linear to non-linear instability. The top row identifies stages $t_1$ to $t_3$ in $Fr_c = 1.1$ and the bottom row, identifies these stages in $Fr_c = 0.8$ . . . . .	98

5-4	Vorticity thickness evolution for (a) $Fr_c = 0.1$ and (b) $Fr_c = 0.8$ and momentum thickness evolution for (c) $Fr_c = 0.1$ and (d) $Fr_c = 0.8$ . In (a) and (b) three points are marked that represent the initiation, inflection and saturation stages in non-linear development. In (c) and (d) the growth rate of momentum thickness is marked with red line. Growth rate of the momentum thickness, $4\dot{\delta}_\theta$ drops from 0.076 to 0.061 from $Fr_c = 0.1$ to $Fr_c = 0.8$ . . . . .	100
5-5	(a) Dependence of the fractional thickness growth rate with $Fr_c$ for momentum, $\delta_\theta$ , and vorticity thickness, $\delta_\omega$ . (b) The ratio of the growth rate to dilation free growth rate, is plotted versus $Fr_c$ and compared with experimental and numerical observations in flows with high Reynolds numbers in gas dynamics. . . . .	102
5-6	The error in energy dissipation using in $Fr_c = 0.8$ using (a) 5 <sup>th</sup> order WENO scheme and (b) MINMOD. WENO exhibits significantly lower level of numerical dissipation compared to MINMOD. . . . .	107
5-7	The distribution of three terms in Equation (5.15) for (a) $Fr_c = 0.6$ at stage $t_3$ , (b) $Fr_c = 0.8$ at stage $t_2$ , (c) $Fr_c = 0.8$ at stage $t_3$ and (d) $Fr_c = 1.1$ at stage $t_3$ . The integration is made over the area of a control volume with the area of $\Delta x \Delta y$ . The left column represents the rate of change on energy ( $\frac{\partial}{\partial t} \int_A E dA$ ), centre column energy flux ( $\oint_s h(gH_t) \vec{U} \cdot \hat{n} ds$ ) and the right column energy dissipation ( $\int_A \epsilon dA$ ). . . . .	109
5-8	The temporal evolution of (a) normal energy rate; (b) normal energy flux and (c) the total energy dissipation as they appear in Equation (5.18) for $Fr_c = 0.8$ . The interrogation regions are limited to $ y^+ = y^-  = \frac{5}{16}\lambda_x, \frac{15}{16}\lambda_x$ and $\frac{25}{16}\lambda_x$ . . . . .	111
5-9	Dependence of peak energy dissipation on convective Froude number. The maximum dissipations plotted in this graph occur at the fully saturated stage of $t_3$ . The maximum dissipation and the maximum thickness are synchronized and emerge simultaneously. . . . .	112

5–10	The production flux and radiation dissipation through transition from linear to non-linear instability. The level of production is constant in two convective Froude numbers, however the radiation dissipation increases from $Fr_c = 0.1$ (left) to $Fr_c = 0.8$ (right). The maximum production in both cases occur right at the inflection point ( $t_2$ ). . . . .	115
5–11	The production flux and radiation dissipation through transition from linear to non-linear instability for $Fr_c = 1.1$ . The radiation dissipation increases further from $Fr_c = 0.8$ to $Fr_c = 1.1$ . . . . .	115
5–12	Dependence of the overall relative radiation dissipation at the inflection point of $t_2$ on convective Froude number. . . . .	116
5–13	Distribution of normal Reynolds stresses, $\overline{u'u'}$ (red lines) and $\overline{v'v'}$ (black lines) for 3 stages of development of $t_1$ , $t_2$ and $t_3$ for $Fr_c = 0.1$ in (a), (b) and (c) and $Fr_c = 1.1$ in (d), (e) and (f). . . . .	118
5–14	Variation of the ratio of normal averaged Reynolds stresses, $\overline{v'v'}/\overline{u'u'}$ with convective Froude number. . . . .	120

## LIST OF SYMBOLS

### Roman Symbols

$c$	wave speed or phase speed
$c_1$	wave speed of free stream 1
$c_2$	wave speed of free stream 2
$C_d$	discharge coefficient
$E$	total energy
$Fr$	Froude number
$Fr_c$	convective Froude number
$Fr_o$	main flow Froude number
$g$	gravity acceleration
$g'$	reduced gravity
$h$	total water depth
$h'$	depth fluctuation
$H$	mean water depth
$H_o$	initial water depth
$H_d$	downstream water depth
$H_t$	hydraulic head
$H_w$	height of the weir
$k$	wave number
$k_x$	wave number in $x$ -direction
$k_y$	wave number in $y$ -direction
$K$	total kinetic energy
$K_m$	mean kinetic energy
$K'$	disturbance kinetic energy
$L$	length of the domain

$Ma_c$	convective Mach number
$P_y$	total energy flux
$P_k$	order of convergence
$P'$	disturbance potential energy
$Q$	total discharge
$Q^*$	total dimensionless discharge
$r$	grid refinement ratio
$\overline{R}$	radiation damping
$\overline{S}$	Shear production
$t$	time
$t_s$	time scale
$u$	velocity in $x$ -direction
$u'$	velocity fluctuation in $x$ -direction
$\overline{u'u'}$	normal Reynolds stress in $x$ -direction
$U$	mean velocity in $x$ -direction
$U_1$	streamwise velocity of free stream 1
$U_2$	streamwise velocity of free stream 2
$\vec{U}$	velocity vector
$\hat{U}_y$	mean velocity gradient at the inflection
$v$	velocity in $y$ -direction
$v'$	velocity fluctuation in $y$ -direction
$\overline{v'v'}$	normal Reynolds stress in $y$ -direction
$W_w$	width of the weir
$x$	streamwise coordinate
$y$	lateral coordinate
$z_o$	bottom elevation

### Greek Symbols

$\alpha$	linear growth rate
$\beta$	smoothness indicator
$\delta_\theta$	momentum thickness
$\delta_\omega$	vorticity thickness
$\Delta U$	streamwise velocity difference
$\Delta x$	grid size in $x$ -direction

$\Delta y$	grid size in $y$ -direction
$\epsilon$	energy dissipation
$\zeta$	vorticity
$\zeta'$	vorticity fluctuation
$\theta$	angular coordinate
$\lambda_x$	wave length in $x$ -direction
$\rho$	density
$\omega_M$	modulation frequency

### Subscripts

critical	critical value
$c$	central node
$d$	downwind node
$dd$	downstream of the downwind node
$o$	initial value
max,min	maximum and minimum values
PM1	Prandtl-Meyer value at main flow Froude number of 1
PM $\infty$	Prandtl-Meyer value at main flow Froude number of infinity
Ritter	Ritter's value
super	supercritical value
$u$	upwind node
$uu$	upstream of the upwind node

### Accents

$\overline{()}$	averaged in $x$ -direction
$\overline{\overline{()}}$	averaged over area

# CHAPTER 1

## INTRODUCTION

### 1.1 Motivations and Objectives

In many environmental science and hydro-technical engineering applications, transition from supercritical to subcritical flow in shallow waters are common occurrence. Water depth jumps from the supercritical flow to the subcritical flow. The breaking waves produced by the jumps are responsible for significant sediment suspension and air entrainment into the flow. These breaking waves are ubiquitous in steep flows through man-made channels, irrigation systems, and mountainous streams and in the density-stratified flows. The depth and velocity discontinuities across a hydraulic jump are the center of focus in numerical simulations. Simulation of the supercritical to subcritical transition is required in the design of energy dissipaters and water diversion structure. Uplifting, cavitation and vibration due to the supercritical to subcritical transitions create unique engineering challenges for the design of such hydraulic structures. Flows overtopping dikes and embankments often are supercritical. Structural design has to be made for the structure to withstand erosion and wave forces. The supercritical to subcritical flow transition is also encountered in density-stratified currents, through the formation of internal hydraulic jumps when the densimetric Froude number exceeds unity in part of the currents.

This phenomenon has been observed in coastal disposal of wastewater (Chu & Vanvari 1976; Chu & Baddour 1984; Chu & Jirka 1986). Hydraulic jumps and surges also have been observed in shallow seas due to the tidal flow interaction with the sea bottom topography. Internal hydraulic jumps can also occur in lakes (Linkens 2010) and examples of such flows are reported by Cortés *et al.* (2014). Despite the frequent observation of supercritical to subcritical transition, the impacts of this sharp transition on many flow processes are not well understood.

Formation of supercritical regime in shallow flows is determined by the propagation of disturbance waves which depends on the magnitude of the flow velocity  $u$  relative to the speed of the gravity wave  $c = \sqrt{gh}$ . The dimensionless parameter is the Froude number,  $Fr = u/c$ . The flow is supercritical if the flow velocity is greater than the wave speed, i.e.  $Fr = u/c > 1$ . The flow is subcritical if the Froude number, i.e.  $Fr = u/c < 1$ . Hydraulic jumps occur in supercritical flow in its transition to subcritical flow. The free-surface flow in open channel and density current in gravity-stratified flow are analogous as they are governed by the same equations. The wave speed in open-channel flow is defined by the constant gravity  $g$  and the depth of the flow  $h$ . In the density current on the other hand, wave speed is defined by density difference,  $\Delta\rho$ , relative to density,  $\rho$ . The reduced gravity  $g' = g\Delta\rho/\rho$  in density currents defines the internal wave speed  $\sqrt{g'h}$ . Small density difference leads to small internal-wave speed and supercritical density currents of large densimetric Froude numbers.

The occurrence of the hydraulic jump and internal hydraulic jump in shallow flows is a phenomenon analogous to the formation of shock waves in gas dynamics.

In compressible flow such as gas, the waves of small amplitude are the sound waves. The ratio of the flow speed  $u$  to the speed of sound  $c$  is the Mach number,  $Ma = u/c$ . Supersonic flows are often accompanied by abrupt pressure changes across the shock wave. The equivalent problem in shallow waters is sudden change in depth across the hydraulic jump. The similarities of the free-surface flow in shallow water and the counterpart of the flow in gas are known. Liggett (1994) has shown that the shallow-water equations for flow in open channel are identical to the two dimensional equations for the compressible flow in gas when the specific heat ratio is equal to 2. This realization is valid if the hydrostatic pressure variation over the water depth is assumed. Furthermore, the flow must be inviscid for the shallow-flow and gas-dynamic analogy to be fully valid.

The main challenge of numerical simulations using the shallow-water equation is the depth and velocity discontinuities across the hydraulic jumps. The numerical scheme must have high accuracy and in the same time maintain computational stability. The balance of accuracy and stability is crucial in the selection of a numerical scheme. The numerical simulations for the shallow flows share many of the computational requirements with the simulations of compressible flows in gas. The methods developed to capture flow discontinuities across the shock waves in the compressible flow are equally capable of capturing depth and velocity discontinuities across the hydraulic jumps. This thesis will review a number of classic Total Variation Diminishing (TVD) shock capturing schemes and compare those with a high-order scheme known as Weighted Essentially Non-Oscillatory (WENO). The WENO scheme developed by Shu (2009) can in principle achieve infinite order of accuracy. These TVD

schemes and WENO scheme are employed for spatial interpolation on a staggered grid. Time integration is conducted using a fourth-order Runge-Kutta method. The performance of the numerical method was verified by three simulation projects reported in this thesis. The three projects are (i) transverse dam-break waves, (ii) linear stability in shallow shear flow and (iii) wave and energy dissipation in sub-critical and supercritical mixing layers. The accuracy of the simulations for each problem is evaluated by comparing the simulation results with the analytical solutions and available experimental data. The results are presented in chapters 2, 3 and 4, respectively.

## 1.2 Computational schemes for high-speed shallow waters

We begin by reviewing the Method Of Characteristics (MOC), which has been popular since the early development of computational hydraulics (Abbott 1966, Henderson 1966, Stoker 1957). In the method of characteristics, the shallow-water equations are transformed onto systems of characteristics along which the governing equations are ordinary differential equations. Many shallow-water wave exact solutions are obtained using the MOC including 1D dam break wave solution by Ritter (1892) and Stoker (1957). However generalizing the MOC to include source terms such as complex topography and friction effect requires corrections that are problem specific. Numerical methods based on the MOC have been developed. One of the popular methods is the Riemann solvers. Local MOC solution obtained in a computational cell has been used to estimate the flux across the face of finite volumes (Roe 1981, Harten *et al.* 1983, LeVeque 2002, Toro 2009).

To overcome the limitation of the Riemann solver, the classical finite volume method is adapted for the solution of the shallow-water equation. High-order accurate interpolation scheme are developed on a staggered grid to capture the depth and velocity discontinuities. Recent developments in this direction for the finite-volume method to find solution of the shallow-water equations can be found in the works by Vázquez-Cendón (1999), Castro *et al.* (2012) and Yuan (2013). Unlike the Riemann solver, the finite-volume method is developed to compute the fluxes on the faces of the finite volume following the direction of the flow velocity rather than the direction of the characteristics. Therefore, the transformation of the governing equations to a hyperbolic system is not required. However, simulation of flow discontinuities relies on shock-capturing schemes to suppress the unphysical spurious numerical oscillation. The Minimal Intervention Strategy (MIS) as described by Pinilla *et al.* (2010), employs Total Variation Diminishing strategy (TVD) to define the fluxes on the faces of the control volume and to confine the numerical oscillation. This method has been successful in capturing the moving hydraulic jumps while maintaining the absolute computational stability. Variety of flux limiting strategies have been developed for shock capturing in compressible flows (e.g. Roe 1985; Gaskell & Lau 1988; Leonard & Mokhtari 1990; Leonard & Drummond 1995). Pinilla *et al.* (2010) tested the popular TVD schemes including MINMOD, MUSCL, SMART, Superbee, ULTRA-QUICK. Adjusting the fluxes in regions near the discontinuities does not affect the overall mass and momentum conservations but slightly impacts the accuracy of the base schemes.

TVD schemes are successful in regulating the numerical oscillations. They can however lead to excessive numerical errors. Therefore in the numerical simulation of a complex flow containing both smooth and sharp regions, employment of such schemes, may require excessive computational grid points to resolve the flow features properly. A high-order interpolation scheme could minimize the computational effort. The Weighted Essentially Non-Oscillatory (WENO) scheme is one high-order interpolation method that has gained popularity in the past decade as the scheme can capture the smooth part of the flow with high-order accuracy, and capture the discontinuity with acceptable accuracy and computational stability. The scheme was first introduced by Liu *et al.* (1994) and Jiand & Shu (1996). The WENO scheme was developed based on Essentially Non-Oscillatory (ENO) scheme introduced by Harten *et al.* (1987) and Shu & Osher (1988). Both the ENO and WENO schemes are constructed by dividing the overall stencil into sub-stencils according to the desirable order of accuracy (see Figure 1–1). In the encounter of discontinuity in one sub-stencil, the ENO scheme would skip entirely the sub-stencil with the discontinuity while manages the interpolation using the remainder of sub-stencils. The strategy of the WENO scheme on the other hand is to weigh the lower order stencil by a smoothness indicator. This strategy of the weighted function is superior in alleviating the problems associated with the abrupt removal of stencil in the ENO schemes (Shu 1990).

The WENO scheme can be extended to have infinite order of accuracy. In the present simulation, the 5<sup>th</sup>-order WENO reconstruction scheme is employed. The 5<sup>th</sup> order WENO, was chosen, as it provides a relatively high order of accuracy in the

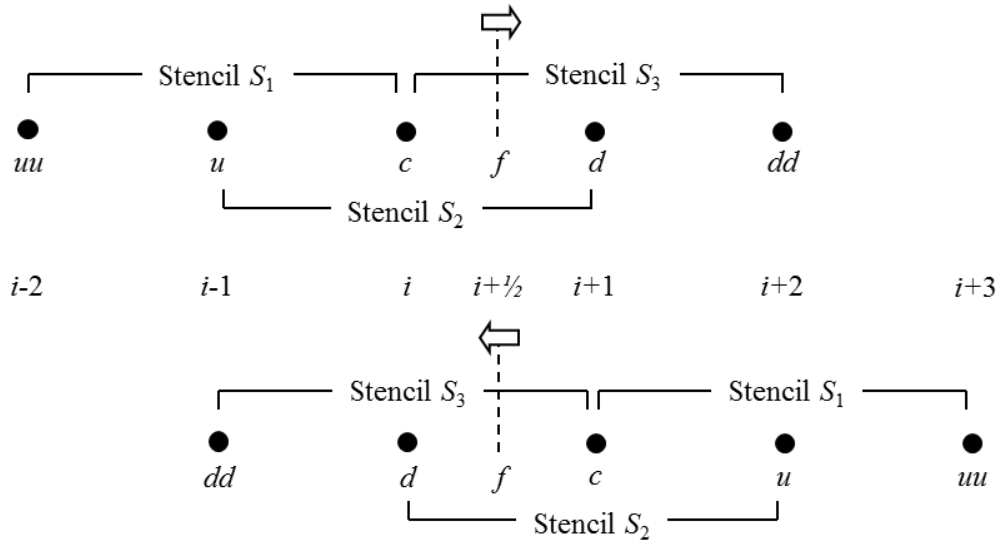


Figure 1–1: The main stencil and three substencils arrangement in  $5^{th}$  order WENO scheme by Shu (2009).

simulation of vortex-shock interaction, without compromising computational effort. The orientation of sub-stencils in a  $5^{th}$  order WENO scheme is demonstrated in Figure 1–1. This figure shows the stencil for a  $5^{th}$ -order scheme and its relation to the sub-stencils of three lower  $3^{rd}$ -order schemes.

### 1.3 Literature Review for Compressible Mixing Layers

Much of the previous studies on instabilities and transition of the instabilities to turbulence were conducted to study the development of the mixing layer between free streams. Mixing layer is turbulent flow formed between two parallel streams of different velocities without the presence of the solid boundary. Despite the common occurrence of such flow features in steep channels and density stratified flow, the literature available is mainly on the analogous dilation effect in gas dynamics. An understanding of the phenomenon in dilation effect on the flow in gas is necessary to

comprehend the shear flow in shallow waters. In gas dynamics the dilation effect due to the expansion and contraction, is widely measured by convective Mach number

$$\text{Ma} = \frac{U_1 - U_2}{c_1 + c_2} \quad (1.1)$$

In the definition of convective Mach number,  $U_1$  and  $U_2$  are the flow velocity and  $c_1$  and  $c_2$  are the speeds of the sounds in the free streams. Convective Mach number is defined based on relative to the free-stream speed rather than absolute speed of the flow. The first attempt to articulate the use of the convective Mach number was by Lin (1953). Later, this parameter was used to investigate high speed mixing layers with various velocities and density ratios by Bogdanoff (1983). The equivalent dimensionless parameter in shallow water is the convective Froude number used by Pinilla & Chu (2008).

$$\text{Fr} = \frac{U_1 - U_2}{c_1 + c_2} \quad (1.2)$$

where  $c_1$  and  $c_2$  are the speeds of the gravity waves. Shock waves are the discontinuities in pressure in gas. In shallow water, the hydraulic jumps are produced as flow changes from supercritical to subcritical state.

Without the dilation effect when the convective Mach number or the convective Froude number approaches zero, the instability of shear flow is describable by the classical Rayleigh inflection point theorem (Rayleigh 1880). Linear instability analysis by Sandham & Reynolds (1991) has found reduction of shear instability with the increase of convective Mach number. Despite the considerable reduction in growth rate, supersonic mixing layers are observed to be marginally unstable. This was explained through a discovery by Satomura (1981) suggesting that even a linear

shear flow can be unstable in shallow water to another mode of instability. The second mode of instability has been studied in Couette flow by Balmforth (1999) and Takehiro & Hayashi (1992). However, the study of second unstable mode and the inflection instability is only briefly considered by Balmforth (1999).

As mixing layer is sensitive to existence of white noise and perturbation in the environment, subsequent to linear stage, subcritical eddies are generally formed. The interaction of this shear flow generates substantial level of mixing across, in between the two flows which is due to a high level of turbulence velocity fluctuation at a zero pressure gradient flow where the Mach and Froude numbers are relatively small. Flow discontinuities in the form of shock wave in compressible fluid, and in the forms of hydraulic jump in free surface flow, have rather strong impact on the growth and development of the mixing layer. Early evidence of compressibility impact on turbulence was discussed by Bradshaw (1977).

Early experiments by Birch & Eggers (1973) first suggested the reduction in spreading rate with compressibility as Mach number increases. Experimental observation by Brown & Roshko (1974) and Papamoschou & Roshko (1988) confirmed that compressibility affects the development of the supersonic shear layer. The review of these works can be found in Lele (1994). Identification of the mechanisms responsible for the inhibited shear layer growth at high Mach number is of interest both to gain a fundamental understanding of the problem and to derive insights into possible mixing enhancement strategies.

The evidence from available studies indicates that the reduction of turbulent kinetic energy in the uniform shear layer as well as the reduced thickness of the

shear layer are related to decreased turbulent production. Vreman *et al.* (1996) among others have numerically studied a temporally evolving mixing layer to show that the reduction in turbulent production is due to dilation dissipation as the Mach number increases. Other experimental observations by Samimy & Elliot (1990), Rossman *et al.* (2002) among others, reported the reduction of growth rate with convective Mach number. Another parameter that was considered as energy sink, was the generation of noise by mixing layer. The production of noise from mixing layer also requires energy which consumes some of the turbulence kinetic energy. The energy flux radiated from mixing layer in the form of sound wave is also studied (see, e.g., Debiève *et al.* 2000).

The impact of compressibility however becomes evident not necessarily at supersonic flow. Even in moderate subsonic mixing layers, the structure of the eddy is modified by the existence of flow discontinuity, *shocklet* (Sandham & Reynolds 1990). The experiment by Papamoschou & Roshko (1988) also explained the intriguing structure of vortex in the presence of shock wave and hydraulic jumps as eddy-shocklets. There have been numerous efforts for the direct numerical simulation (DNS) of the compressible mixing layer. Vreman *et al.* (1996), Pantanto & Sarkar (2002), Fu & Li (2006) and Barone *et al.* (2006) are amongst the DNS of the mixing layer, correlating the reduction in growth rate in higher Mach numbers to compressibility. In supersonic convective Mach numbers, it has been reported that long shocklets are radiated from elongated vortices.

On the anisotropy of compressible flow, there have been discrepancies in literature. While several studies (e.g., Samimy & Elliot 1990; Pantanto & Sarkar 2002)

have suggested that the turbulent anisotropy expressed in terms of longitudinal versus transverse velocity fluctuations, is relatively constant over different Mach numbers, others studies (e.g. Goebel & Dutton 1991; Gruber *et al.* 1993) have actually shown a growth with Mach number. Despite numerous experimental and numerical investigations on shock-vortex interaction, due to inconsistency in results reported, further studies are required on this subject. The understanding of such flows is an important element in attempting to develop models for much more complex shock-turbulence interactions for highly inhomogeneous flows.

#### 1.4 Thesis Organization

This thesis is written in the manuscript-based format. It is a collection of papers accepted and submitted for publications supervised by Professor V. H. Chu. A summary of the collection is given in the Introduction chapter. This chapter also provides the motivation and objectives, a brief overview of the numerical methods and a literature review for supersonic and supercritical flows. Chapters 2 to 5 are drawn from the following journal papers, respectively:

1. S. Karimpour Ghannadi, and V. H. Chu. High-order Interpolation Schemes for Shear Instability Simulations. *International Journal of Numerical Methods for Heat and Fluid Flow*, In press, 2015.
2. S. Karimpour Ghannadi, and V. H. Chu. Transverse Dam-Break Waves. *Journal of Fluid Mechanics*, Volume 758, November 2014, R2 (12 pages).
3. S. Karimpour Ghannadi, and V. H. Chu. Linear Instabilities in Shallow Flows. *Journal of Fluid Mechanics*, draft for submission, 2014.

4. S. Karimpour Ghannadi, and V. H. Chu. Wave and Energy Dissipation in Subcritical and Supercritical Mixing Layers. *Journal of Fluid Mechanics*, draft for submission, 2014.

Chapter 2 explains the numerical method applied in this thesis to attain high-order of accuracy in a complex flow problem. The application of TVD schemes, as well as a high order WENO scheme is introduced in this paper. These are implemented on a staggered grid using the finite volume method. Different shock-capturing schemes are put to the test in the calculations for eddies and shocklets in the simulation of shear instabilities over a range of convective Froude numbers. The performance of the TVD and WENO schemes are evaluated using progressively refined grid. The computation error of each scheme is determined by extrapolation to the estimated exact solution. Some of TVD schemes showed promising results. The fifth-order WENO scheme generally performed better. Despite the higher accuracy of WENO scheme, it can be computationally expensive and should only be chosen for demanding applications. Otherwise TVD schemes are better fit to simulate the problems that are expected to contain only flow discontinuities.

Chapter 3 was inspired to prove that a TVD scheme is capable of simulating a fully 2D problem, without the requirement of high order interpolation scheme, with acceptable accuracy. Flow diversion from a main channel to the side through a weir is investigated numerically for subcritical and supercritical main flows (see Figure 1–2). In this chapter, results demonstrate that even in subcritical main flow, flow across the weir is significantly regulated by supercritical expansion fan. Results

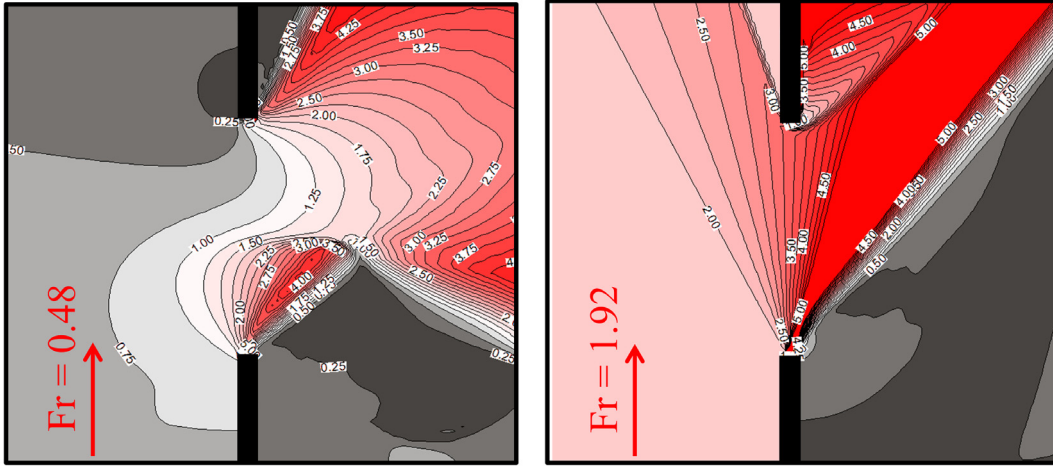


Figure 1–2: Supercritical expansion fan formation in  $Fr_o = 0.48$  and  $1.92$ , reported in chapter 3.

are presented in the framework of the classical dam break wave solution by Ritter (1892). In one limiting case of supercritical main flow, the results are consistent with Prandtl-Meyer expansion, developed originally for gas dynamics. On the other hand, results are in agreement with available experimental data in low speed subcritical main flows.

In the next two chapters, the preferred shock capturing method is WENO. In chapter 4 the instability beyond the classical Rayleigh instability is explored for the supercritical mixing layer. In this paper, the instability of mixing layer with various Froude numbers is studied. In the subcritical mixing layer, the classical results by Sandham & Reynold (1990) are reproduced. However the extension to supercritical mixing layer has shown existence of a second mode of instability, not seen in classical investigation of linear instability. This mode of instability is raised by supercritical waves that produce modulation in the growth of turbulence kinetic energy, turbulence

potential energy and other flow features. Amplitude of the small perturbations is observed to amplify thousands of time while maintaining a consistent structure. This consistent structure withstands until non-linear stage is reached. The modulation of the instability is explained in terms of energy entrapment between the returning surfaces, where the relative speed matches the speed of the wave.

In chapter 5 the development of the mixing layer to form eddies and shocklets are obtained from the direct numerical simulations. Radiation of wave energy and the local energy dissipation across the jumps were determined and correlated with the fractional spreading rate of the mixing layer. The fractional rates for a range of convective Froude numbers are compared with available data obtained for the analogous problem in gas dynamics. In addition, the total energy dissipation and radiation damping are studied. The anisotropy of the flow in the presence of shocklets is also analyzed.

The final conclusion chapter provides (i) a summary of computational results, (ii) the contribution of the thesis to knowledge and (iii) suggestions for further investigations.

## CHAPTER 2 HIGH-ORDER INTERPOLATION SCHEMES FOR SHEAR INSTABILITY SIMULATIONS

S. Karimpour Ghannadi and V. H. Chu. High-order Interpolation Schemes for Shear Instability Simulations. *International Journal of Numerical Methods for Heat and Fluid Flow*, In press, 2015.

### 2.1 Abstract

**Purpose:** The performance of a numerical method for the solution to shallow-water equations on a staggered grid is evaluated in simulations for shear instabilities at two convective Froude numbers.

**Design/methodology/approach:** The simulations start from a small perturbation to a base flow with a hyperbolic-tangent velocity profile. The subsequent development of the shear instabilities is studied from the simulations using a number of flux-limiting schemes, including the second-order MINMOD, the third-order ULTRA-QUICK and the fifth-order WENO schemes for the spatial interpolation of the nonlinear fluxes. The fourth-order Runge-Kutta method advances the simulation in time.

**Findings:** The simulations determine two parameters: (i) the fractional growth rate of the linear instabilities; and (ii) the vorticity thickness of the first nonlinear peak. Grid refinement using 32, 64, 128, 256 and 512 nodes over one wave length determines

the exact values by extrapolation and the computational error for the parameters. It also determines the overall order of convergence for each of the flux-limiting schemes used in the numerical simulations.

**Originality/value:** The four-digit accuracy of the numerical-simulations presented in this paper are comparable to analytical solutions. The development of this reliable numerical simulation method has paved the way for further study of the instabilities in shear flows that radiate waves.

**Keywords:** Shear Instabilities, Staggered Computational Grid, Flux-Limiting Strategy, MINMOD, ULTRA-QUICK, WENO.

## 2.2 Introduction

Shear instabilities are initiations of turbulence. The study of shear instabilities is therefore directly related to the modelling and simulation of turbulence. Instability analysis has been carried out traditionally using linear stability analysis and normal mode approach; see, e.g., Michalke (1964) and Sandham & Reynolds (1990). The initial growth of a small disturbance is determined as an eigenvalue problem of the governing ordinary differential equations. In this paper, the instabilities are determined from numerical simulations using the fully nonlinear equations. Wave radiation and the formation of shock waves are admissible to the solution of the shallow-water equations. The numerical simulation must have the capability to capture the shock waves and reproduce the classical results obtained from the linear stability analysis. The accuracy of the simulations for the instabilities depends on the numerical schemes and the grid sizes used for the simulations. The flow of two

different Froude numbers of the shallow shear flow are considered in order to examine the role of wave radiation and formation of shock waves in the linear and nonlinear stages of the instabilities' development. Radiation of wave is known to play a critical role on instability in compressible gas at high Mach numbers; see, e.g., Mack (1990) and Lee *et al.* (1991). The numerical simulation of the radiation requires a high order of numerical accuracy. The adapted boundary conditions allow the wave radiation from the instabilities to escape without reflection. The numerical method for the present simulation is developed for computation using a staggered grid. The nonlinear fluxes are calculated by a number of flux-limiting schemes, including the second-order MINMOD, the third-order ULTRA-QUICK and the fifth-order WENO schemes. The staggered grid is employed for its simplicity so that the simulations can be carried out to a high order of accuracy. A fourth order Runge-Kutta method is employed for the time integration. The order of accuracy of each of the limiting schemes is evaluated from a grid-refinement study that allows it to be compared with the intrinsic order of the scheme.

The paper has six sections including this introductory section. Section 2 presents the equations in a suitable form for the numerical simulations on a staggered grid. Section 3 provides the details of the numerical simulation method including the steps for interpolation of the nonlinear fluxes and the implementation details of the flux-limiting schemes of various orders of accuracy. The shear instability problem is considered in Section 4 and Section 5. Section 4 reports the calculations for the exponential growth in the initial linear stage of the instability development. Section

5 presents the calculations for the nonlinear development. Summary and conclusion are given in the final section, 6.

### 2.3 Shallow-water Equations

The governing shallow-water equations for the present investigation are:

$$\frac{\partial h}{\partial t} + \frac{\partial q_x}{\partial x} + \frac{\partial q_y}{\partial y} = 0 \quad (2.1)$$

$$\frac{\partial q_x}{\partial t} + \frac{\partial \mathcal{F}^{uq_x}}{\partial x} + \frac{\partial \mathcal{F}^{vq_x}}{\partial y} = -gh \frac{\partial h}{\partial x} \quad (2.2)$$

$$\frac{\partial q_y}{\partial t} + \frac{\partial \mathcal{F}^{uq_y}}{\partial x} + \frac{\partial \mathcal{F}^{vq_y}}{\partial y} = -gh \frac{\partial h}{\partial y} \quad (2.3)$$

where  $g$  = gravity,  $h$  = water depth, and  $(q_x, q_y)$  = flow rate in  $x$ - and  $y$ -directions respectively. The continuity equation (2.1) is linear. The nonlinear fluxes in the momentum equations (2.2) and (2.3) are

$$\mathcal{F}^{uq_x} = uq_x, \quad \mathcal{F}^{vq_x} = vq_x \quad (2.4)$$

$$\mathcal{F}^{uq_y} = uq_y, \quad \mathcal{F}^{vq_y} = vq_y \quad (2.5)$$

These fluxes are sources of unphysical spurious oscillations. An effective flux-limiting strategy is employed to manage the spurious oscillations for computational stability. Derivation of shallow-water equations can be found for example in Vreugdenhil (1994).

## 2.4 Formulation on Staggered Grid

The finite-volume approximation of the shallow-water equations is implemented on a staggered grid. The arrays  $h_{(i,j)}$ ,  $q_{x(i,j)}$  and  $q_{y(i,j)}$  are defined at the  $h$ -node,  $q_x$ -node, and  $q_y$ -node respectively. The arrays  $\bar{h}_{(i,j)}$ ,  $\bar{q}_x(i,j)$  and  $\bar{q}_y(i,j)$  are the cell averages. Figure 2–1 shows the nodes and the finite volumes on the staggered grid. The continuity equation (2.1) determines the temporal rate of change of the water depth  $d\bar{h}_{(i,j)}/dt = \mathcal{R}_{(i,j)}^h$ , which is the balance of the volume fluxes  $q_{x(i,j)}$  and  $q_{y(i,j)}$  in and out of the finite volume shown in Figure 2–1(a). The  $x$ -momentum equation (2.2) determines the rate  $d\bar{q}_x(i,j)/dt = \mathcal{R}_{(i,j)}^{q_x}$  by balancing the momentum fluxes  $\mathcal{F}_{(i,j)}^{uq_x}$  and  $\mathcal{F}_{(i,j)}^{vq_x}$  in the finite volume shown in Figure 2–1(b). The  $y$ -momentum equation (2.3) determines the rate  $d\bar{q}_y(i,j)/dt = \mathcal{R}_{(i,j)}^{q_y}$  by balancing the momentum fluxes  $\mathcal{F}_{(i,j)}^{uq_y}$  and  $\mathcal{F}_{(i,j)}^{vq_y}$  in the finite volume shown in Figure 2–1(c). The cell averages  $\bar{h}_{(i,j)}$ ,  $\bar{q}_x(i,j)$  and  $\bar{q}_y(i,j)$  are updated at each time step. The cell averages at time  $t + \Delta t$  are determined by their values at previous time  $t$  by a 4<sup>th</sup>-order Runge Kutta method.

### 2.4.1 Interpolation on the Staggered Grid

For accuracy and stability of the computation, the spatial interpolation for the fluxes are managed by *flux limiting* to prevent amplification of the unphysical numerical oscillations. The nonlinear fluxes  $\mathcal{F}_{(i,j)}^{uq_x}$  and  $\mathcal{F}_{(i,j)}^{vq_y}$  are defined at the  $h$ -node, while the fluxes  $\mathcal{F}_{(i,j)}^{uq_y}$  and  $\mathcal{F}_{(i,j)}^{vq_x}$  are defined at the  $\zeta$ -node. The values of  $u_{(i,j)}$ ,  $v_{(i,j)}$ ,  $q_{x(i,j)}$ ,  $q_{y(i,j)}$  needed for evaluation of these fluxes at the  $h$ -node and  $\zeta$ -node are determined by spatial interpolation in two dimensions on the staggered grid.

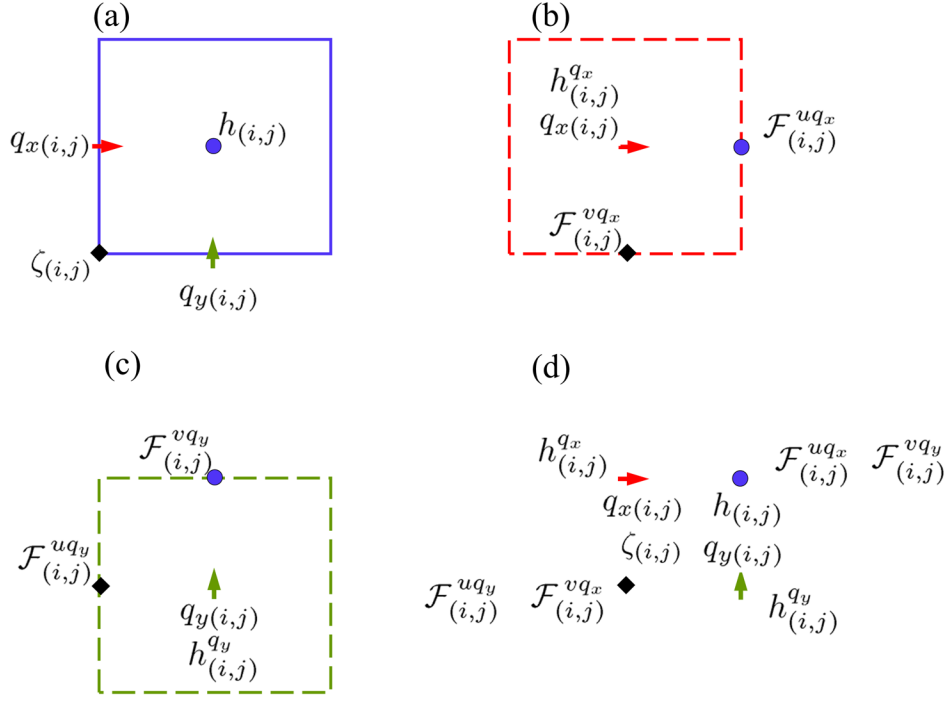


Figure 2-1: (a) finite volume for the calculation of  $h_{(i,j)}$  using the continuity equation, (b) finite volume for the calculation of  $q_{x(i,j)}$  using the  $x$ -momentum equation, (c) finite volume for the calculation of  $q_{y(i,j)}$  using the  $y$ -momentum equation, (d) locations where nonlinear fluxes ( $\mathcal{F}_{(i,j)}^{uq_x}$ ,  $\mathcal{F}_{(i,j)}^{vq_x}$ ,  $\mathcal{F}_{(i,j)}^{uq_y}$ ,  $\mathcal{F}_{(i,j)}^{vq_y}$ ) and depths ( $h_{(i,j)}^{q_x}$ ,  $h_{(i,j)}^{q_y}$ ) are determined by interpolation.

The interpolation begins by finding the values of the array  $h_{(i,j)}^{q_x}$  at the  $q_x$ -node and the array  $h_{(i,j)}^{q_y}$  at the  $q_y$ -node, so that the velocity components  $u_{(i,j)} = q_{x(i,j)}/h_{(i,j)}^{q_x}$  and  $v_{(i,j)} = q_{y(i,j)}/h_{(i,j)}^{q_y}$  are evaluated at these nodes. Figure 2-1(d) shows the relative positions between the  $h$ -node,  $q_x$ -node,  $q_y$ -node and  $\zeta$ -node for the interpolation. The interpolations to find the nonlinear fluxes  $\mathcal{F}^{uq_x}(i,j)$  and  $\mathcal{F}^{vq_y}(i,j)$  at the  $h$ -node, and the fluxes  $\mathcal{F}^{vq_x}(i,j)$  and  $\mathcal{F}^{uq_y}(i,j)$  at  $\zeta$ -node, has the following steps:

1. Interpolation to find  $h_{(i,j)}^{q_x}$  at the  $q_x$ -node and then find  $u_{(i,j)} = q_{x(i,j)}/h_{(i,j)}^{q_x}$ .
2. Interpolation to find  $h_{(i,j)}^{q_y}$  at the  $q_y$ -node and then find  $v_{(i,j)} = q_{y(i,j)}/h_{(i,j)}^{q_y}$ .
3. Interpolation to find  $u_{(i,j)}$  and  $q_{x(i,j)}$  at the  $h$ -nodes using the upwinding direction

- decided by  $\frac{1}{2}(q_{x(i,j)} + q_{x(i+1,j)})$ . Compute the nonlinear flux  $\mathcal{F}_{(i,j)}^{uq_x}$  at the  $h$ -nodes.
4. Interpolation to find  $v_{(i,j)}$  at the  $\zeta$ -node using the upwinding direction decided by  $\frac{1}{2}(q_{x(i,j)} + q_{x(i,j-1)})$ . Interpolation to find  $q_{x(i,j)}$  at the  $\zeta$ -node using the upwinding direction decided by the  $v_{(i,j)}$  at the  $\zeta$ -node. Compute the nonlinear flux  $\mathcal{F}_{(i,j)}^{vq_x}$  at the  $\zeta$ -node.
  5. Interpolation to find  $v_{(i,j)}$  at  $h$ -nodes using the upwinding direction decided by  $\frac{1}{2}(q_{y(i,j)} + q_{y(i,j+1)})$ . Compute the nonlinear flux  $\mathcal{F}_{(i,j)}^{vq_y}$  at the  $h$ -node.
  6. Interpolate to find  $u_{(i,j)}$  at the  $\zeta$ -node using the upwinding direction decided by  $\frac{1}{2}(q_{y(i,j)} + q_{y(i-,j)})$ . Interpolation to find  $q_{y(i,j)}$  at the  $\zeta$ -node using the upwinding direction decided by the  $u_{(i,j)}$  at the  $\zeta$ -node. Compute the nonlinear flux  $\mathcal{F}_{(i,j)}^{uq_y}$  at the  $\zeta$ -node.

Each step of these interpolations on the staggered grid is a one-dimensional (1D) problem of finding the *face* value  $\phi_f$  at a position between the center  $c$ -node and the downwind  $d$ -node, as delineated in figure 2-2. The distance between the nodes is  $\Delta$ , which is equal to either  $\Delta x$  or  $\Delta y$ . The location of the face is  $\frac{1}{2}\Delta$  downwind from the  $c$ -node. The number of nodes needed depends on the order of the accuracy of the interpolation scheme. The First-Order Upwind (FOU) scheme involves only the  $c$ -node:

$$\phi_f = \phi_c + O(\Delta) \tag{2.6}$$

The Central Difference (CD) and Quadratic Upwind Interpolation Convective Kinetics (QUICK) schemes are second-order and third-order accurate. The interpolation

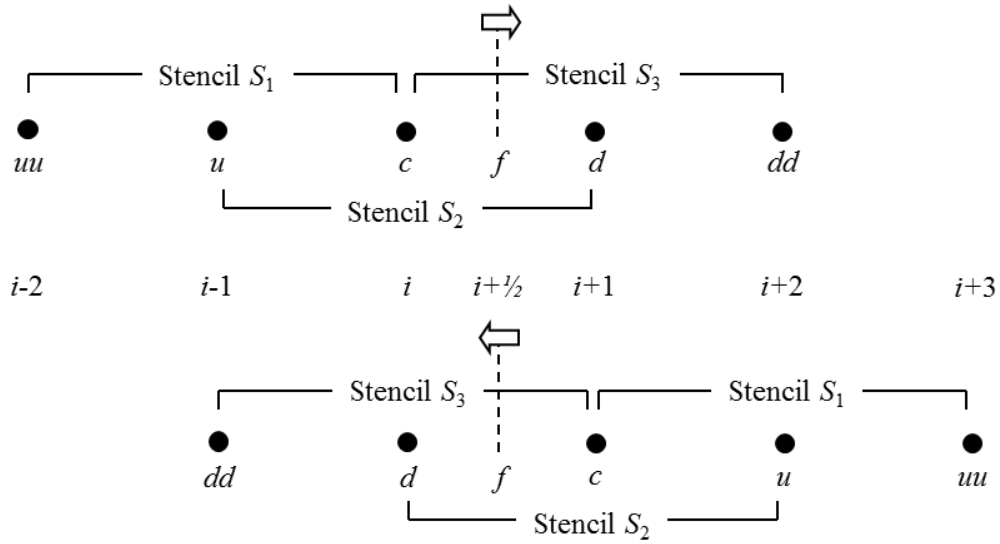


Figure 2–2: The  $uu$ -node,  $u$ -node,  $c$ -node,  $d$ -node and  $dd$ -node used in the upwinding interpolation for value  $\phi_f$  between the  $c$ -node and  $d$ -node.

formulae for these schemes respectively are

$$\phi_f = \frac{1}{2}(\phi_c + \phi_d) + O(\Delta^2) \quad (2.7)$$

$$\phi_f = \frac{1}{8}(-\phi_u + 6\phi_c + 3\phi_d) + O(\Delta^3) \quad (2.8)$$

The CD and QUICK schemes are known to produce spurious numerical oscillations (Versteeg & Malalasekera 2007; Vreugdenhil 1994). If these oscillations are allowed to amplify over time, they can lead to erroneous physics, numerical instability and the ultimate breakdown of the computation.

## 2.4.2 Flux-Limiting Schemes

Flux-limiting schemes have been developed for high-order schemes to suppress overshoot and undershoot across any sharp discontinuity. The fluxes are modified by lowering the order of the schemes, using for example the FOU to gain computational stability. The strategy is to first detect the unphysical oscillations and then to decide whether or not to lower the order of the interpolation.

### DWF-NV Diagram

Dimensionless parameters known as the Normalized Variable (NV) and the Downwind Weighting Factor (DWF) were introduced by Leonard (1988), Leonard (1991) and Leonard & Mokhtari (1990) to define the flux-limiting strategies in a DWF-NV diagram as shown in figure 2–3. Leonard & Mokhtari (1990) introduced the Universal Limiter for Tight Resolution and Accuracy (ULTRA). The strategy developed for the third-order QUICK was ULTRA-QUICK. Pinilla *et al.* (2010) formalized the flux-limiting strategy using the DWF and NV for two-dimensional (2D) simulations on a staggered grid. The detector of the unphysical oscillations is the normalized variable

$$\text{NV} = \frac{\phi_c - \phi_u}{\phi_d - \phi_u} \quad (2.9)$$

The variation will be monotonic if the nodal value  $\phi_c$  at the center lies between the upwind nodal value  $\phi_u$  and the downwind nodal value  $\phi_d$ , that is if the NV lies in the range  $0 < \text{NV} < 1$ . On the other hand, the variation will be non-monotonic if the value  $\phi_c$  lies outside the range  $0 < \text{NV} < 1$ , that is either in the range  $\text{NV} < 0$  or in the range  $\text{NV} > 1$ . The face value  $\phi_f$  is selected according to the downwind

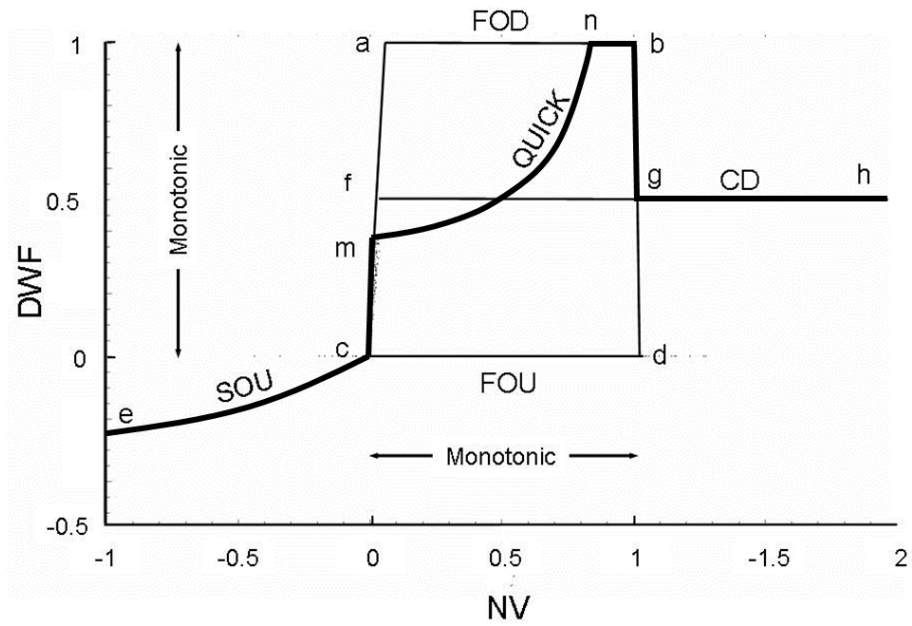


Figure 2-3: The DWF-NV diagram of Leonard & Mokhtari (1990) delineating the monotonic region and its relation in the diagram to various interpolation schemes including FOU, CD, SOU, FOD and QUICK. The thick solid line defines the flux limiter ULTRA-QUICK.

weighting factor

$$\text{DWF} = \frac{\phi_f - \phi_c}{\phi_d - \phi_c} \quad (2.10)$$

Once the value of the DWF is selected, the face value is determined as a function of the DWF as follows:

$$\phi_f = \phi_c + \text{DWF}(\phi_d - \phi_c) \quad (2.11)$$

The variation from  $\phi_c$  at the center node to the face value  $\phi_f$  and then to  $\phi_d$  at the downwind node will be monotonic if the DWF value is in the range  $0 < \text{DWF} < 1$ . On the other hand the variation will be non-monotonic if the DWF value is either in the range  $\text{DWF} < 0$  or in the range  $\text{DWF} > 1$ . The DWF-NV diagram in figure 2-3 delineates the monotonic region a-b-c-d and a number of well-known interpolation schemes. The DWF values for these schemes in the diagram are

DWF = 1	for FOD (first-order downwind) scheme
DWF = 0	for FOU (first-order upwind) scheme
DWF = 0.5	for CD (central differencing) scheme
DWF = 0.5 $\Theta$	for SOU (second-order upwind) scheme
DWF = 0.375 + 0.125 $\Theta$	for QUICK scheme

In these formulae,

$$\Theta = \frac{NV}{1 - NV} \quad (2.12)$$

Alternate to the normalized variable as detector of unphysical oscillations is the ratio of the consecutive gradients  $\Theta$ . The consecutive gradients are  $(\phi_c - \phi_u)/\Delta$  and

Flux Limiting Schemes	Non-Monotonic NV < 1	Monotonic 0 < NV < 1	Non-Monotonic NV > 1
MINMOD	0	$\min[0.5\Theta, 0.5]$	0
MUSCL	0	$\min[\Theta, 0.25+0.5\Theta, 1]$	0
SMART	0	$\min[2\Theta, 0.375+0.125\Theta, 1]$	0
SUPERBEE	0	$\max\min[\Theta, 0.5], \min[0.5\Theta, 1]$	0
ULTRA-QUICK	$0.5\Theta$	$\min[\text{abs}(1/\text{Co}-1)\Theta, 0.375+0.125\Theta, 1]$	0.5
ULTRA-CD	$0.5\Theta$	$\min[\text{abs}(1/\text{Co}-1)\Theta, 0.5]$	0.5

Table 2–1: DWF formulae in the non-monotonic ( $NV < 1$ ), monotonic ( $0 < NV < 1$ ) and non-monotonic ( $NV > 1$ ) regions for the six flux-limiting strategies;  $\text{Co} =$  Courant number

$(\phi_d - \phi_c)/\Delta$ , and the ratio is

$$\Theta = \frac{(\phi_c - \phi_u)}{(\phi_d - \phi_c)} \quad (2.13)$$

The ratio of the consecutive gradients  $\Theta$  is a unique function of the normalized variable  $NV$  as given by Equation (2.12). It is the detector that has been used by VanLeer (1977), Harten (1983), Roe (1985), Sweby (1984) and Gaskell & Lau (1988) in their searches for Total Variation Diminishing (TVD) flux-limiting schemes. The monotonic range of the normalized variable is  $0 < NV < 1$ . The corresponding range for the ratio of consecutive gradients is  $0 < \Theta < \infty$ . The DWFs as a function of  $\Theta$  are given in table 1 for six well known flux-limiting schemes: MINMOD, SUPERBEE, SMART, MUSCL, ULTRA-QUICK and ULTRA-CD. Most of these flux-limiting schemes are Total Variation Diminishing (TVD). In the monotonic part a-b-c-d of the DWF- $NV$  diagram, within the range of normalized variable  $0 < NV < 1$ , the DWF values of most flux limiters are selected to be within the TVD region of the DWF- $\Theta$  diagram of Sweby, as shown in figure 2–4. The lower boundary of the

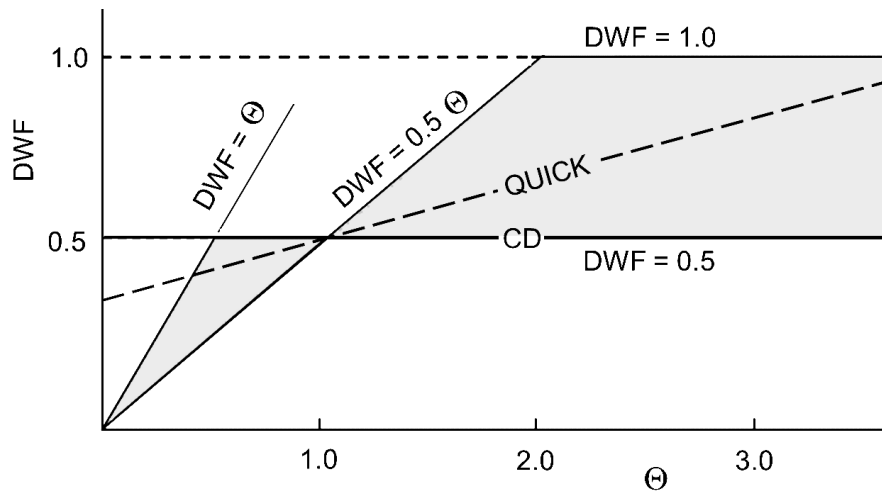


Figure 2–4: The TVD region (gray) in the DWF- $\Theta$  diagram of Sweby (1984). The upper boundary of TVD region is SUPERBEE and the lower boundary is MINMOD.

TVD region is the MINMOD and the upper boundary of the TVD region is the SUPERBEE. The ULTRA-QUICK and ULTRA-CD universal flux limiters of Leonard & Mokhtari (1990) are beyond TVD because parts of the ULTRA-QUICK and ULTRA-CD constraints are outside the TVD region. Although MINMOD and SUPERBEE are TVD, they are not as accurate as ULTRA-QUICK. The base scheme of ULTRA-QUICK is third-order accurate QUICK, as shown in Figure 2–3. The lowering to FOD, SOU and CD in ULTRA-QUICK occurs only rarely and only minimally alters the order of the order of QUICK. In their computation of heated wake, Bouhairie & Chu (2007) have shown how flux limiters are minimal interventions that do not change the order of accuracy of the base scheme significantly.

## WENO Reconstruction

Almost all flux-limiting schemes manage the unphysical numerical oscillations by lowering the order of interpolation. For those schemes listed in Table 2–1, the switching to the lower-order scheme is abrupt, occurring immediately after the variation is detected by the NV to be non-monotonic. The Weighted Essentially Non-Oscillatory (WENO) scheme by Jiang & Shu (1996) on the other hand is a less abrupt procedure. The strategy of the WENO is to weight the lower-order schemes by a smoothness indicator. In the present simulation, the 5<sup>th</sup>-order WENO reconstruction scheme is employed. Figure 2–2 shows the stencil for a 5<sup>th</sup>-order scheme and its relation to the sub-stencils of three lower 3<sup>rd</sup>-order schemes. The reconstruction scheme is employed because the updated values of  $h$ ,  $q_x$ , and  $q_y$  are cell averages, not nodal values. The interpolation for the face values therefore is based on the cell averages. The following are the reconstruction formulae derived by Jiang & Shu (1996), Shu (2009) and Shu (1998) for the face value  $\phi_f$  from the cell averages  $(\bar{\phi}_{uu}, \bar{\phi}_u, \bar{\phi}_c, \bar{\phi}_d, \bar{\phi}_{dd})$ :

$$\phi_f = \frac{1}{30}\bar{\phi}_{uu} - \frac{13}{60}\bar{\phi}_u + \frac{47}{60}\bar{\phi}_c + \frac{9}{20}\bar{\phi}_d - \frac{1}{20}\bar{\phi}_{dd} \quad (2.14)$$

which is a linear convex combination of three 3<sup>rd</sup>-order interpolations

$$\phi_f = \gamma_1\phi_{1f} + \gamma_2\phi_{2f} + \gamma_3\phi_{3f} \quad (2.15)$$

Figure 2–2 shows the stencils  $S_1 = \{\bar{\phi}_{uu}, \bar{\phi}_u, \bar{\phi}_c\}$ ,  $S_2 = \{\bar{\phi}_u, \bar{\phi}_c, \bar{\phi}_d\}$ , and  $S_3 = \{\bar{\phi}_c, \bar{\phi}_d, \bar{\phi}_{dd}\}$  for the three 3<sup>rd</sup>-order approximations. The interpolation formulae for these, respectively, are

$$\phi_{1f} = \frac{1}{3}\bar{\phi}_{uu} - \frac{7}{6}\bar{\phi}_u + \frac{11}{6}\bar{\phi}_c \quad (2.16)$$

$$\phi_{2f} = -\frac{1}{6}\bar{\phi}_u + \frac{5}{6}\bar{\phi}_c + \frac{1}{3}\bar{\phi}_d \quad (2.17)$$

$$\phi_{3f} = \frac{1}{3}\bar{\phi}_c + \frac{5}{6}\bar{\phi}_d - \frac{1}{6}\bar{\phi}_{dd} \quad (2.18)$$

The combination would be fifth-order accurate if the weighting factors were

$$\gamma_1 = \frac{1}{10}, \gamma_2 = \frac{3}{5}, \text{ and } \gamma_3 = \frac{3}{10} \quad (2.19)$$

The method of WENO by Jiang & Shu (1996) for an essentially non-oscillatory solution is to let

$$\phi_f = \omega_1\phi_{1f} + \omega_2\phi_{2f} + \omega_3\phi_{3f} \quad (2.20)$$

and then to choose the *nonlinear weight functions*  $\omega_j$  using the strategy that (i)  $\omega_j \simeq \gamma_j$  if the function  $\phi$  is smooth in the entire region over the big stencil  $S$  and (ii)  $\omega_j \simeq 0$  if  $\phi$  has a discontinuity somewhere within the stencil  $S_j$ . The choice relies on the smooth indicators  $\beta_j$  and then the calculations of the nonlinear weight functions  $\omega_k$  by the following formulae:

$$\beta_1 = \frac{13}{12}(\bar{\phi}_{uu} - 2\bar{\phi}_u + \bar{\phi}_c)^2 + \frac{1}{4}(\bar{\phi}_{uu} - 4\bar{\phi}_u + 3\bar{\phi}_c)^2 \quad (2.21)$$

$$\beta_2 = \frac{13}{12}(\bar{\phi}_u - 2\bar{\phi}_c + \bar{\phi}_d)^2 + \frac{1}{4}(\bar{\phi}_u - \bar{\phi}_d)^2 \quad (2.22)$$

$$\beta_3 = \frac{13}{12}(\bar{\phi}_c - 2\bar{\phi}_d + \bar{\phi}_{dd})^2 + \frac{1}{4}(3\bar{\phi}_c - 4\bar{\phi}_d + \bar{\phi}_{dd})^2 \quad (2.23)$$

$$\omega_k = \frac{\tilde{\omega}_k}{\tilde{\omega}_1 + \tilde{\omega}_2 + \tilde{\omega}_3} \quad \text{with} \quad \tilde{\omega}_k = \frac{\gamma_k}{(\epsilon + \beta_k)^2} \quad (2.24)$$

The positive small number is typically  $\epsilon = 10^{-6}$ , which is selected to avoid a zero denominator in the calculation for  $\tilde{\omega}_k$ .

### 2.4.3 Advance in Time by the Runge-Kutta Method

The time integration of the continuity and  $x$ - and  $y$ -momentum equations for cell-averaged values of  $\{h_{(i,j)}, q_{x(i,j)}, q_{y(i,j)}\}$  is explicit using the fourth-order Runge-Kutta method (RK4). Using  $\bar{\phi}$  to represent  $\{h_{(i,j)}, q_{x(i,j)}, q_{y(i,j)}\}$ , the time advancement from the value of  $\bar{\phi}^n$  at time  $t = n \Delta t$  to the value of  $\bar{\phi}^{n+1}$  at time  $t = (n+1)\Delta t$  is determined by the RK4 formula as follows (see, e.g., Vahl Davis 1986):

$$\bar{\phi}^{n+1} = \bar{\phi}^n + \frac{\Delta t}{6} (\mathcal{R}_1 + 2\mathcal{R}_2 + 2\mathcal{R}_3 + \mathcal{R}_4) \quad (2.25)$$

in which  $\mathcal{R}_1$ ,  $\mathcal{R}_2$ ,  $\mathcal{R}_3$  and  $\mathcal{R}_4$  are the estimated rate functions at time  $t_1 = n\Delta t$ ,  $t_2 = (n + \frac{1}{2})\Delta t$ ,  $t_3 = (n + \frac{1}{2})\Delta t$  and  $t_4 = (n + 1)\Delta t$ , respectively:

$$\mathcal{R}_1 = \mathcal{R}(t^n, \bar{\phi}^n) \quad (2.26)$$

$$\mathcal{R}_2 = \mathcal{R}(t^n + \frac{\Delta t}{2}, \bar{\phi}^n + \frac{\Delta t}{2} \mathcal{R}_1) \quad (2.27)$$

$$\mathcal{R}_3 = \mathcal{R}(t^n + \frac{\Delta t}{2}, \bar{\phi}^n + \frac{\Delta t}{2} \mathcal{R}_2) \quad (2.28)$$

$$\mathcal{R}_4 = \mathcal{R}(t^n + \Delta t, \bar{\phi}^n + \Delta t \mathcal{R}_3) \quad (2.29)$$

The rate of  $h_{(i,j)}$  for advancing  $h_{(i,j)}^n$  to  $h_{(i,j)}^{(n+1)}$  according to the continuity equation is

$$\mathcal{R}^h = -\frac{q_{x(i+1,j)} - q_{x(i,j)}}{\Delta x} - \frac{q_{y(i,j+1)} - q_{y(i,j)}}{\Delta y} \quad (2.30)$$

The rate of  $q_{x(i,j)}$  according to the  $x$ -momentum equation is

$$\mathcal{R}^{q_x} = -\frac{\mathcal{F}_{(i,j)}^{uq_x} - \mathcal{F}_{(i-1,j)}^{uq_x}}{\Delta x} - \frac{\mathcal{F}_{(i,j+1)}^{vq_x} - \mathcal{F}_{(i,j)}^{vq_x}}{\Delta y} - g \frac{h_{(i,j)}^2 - h_{(i-1,j)}^2}{\Delta x} \quad (2.31)$$

The rate of  $q_{y(i,j)}$  according to the  $y$ -momentum equation is

$$\mathcal{R}^{q_y} = - \frac{\mathcal{F}_{(i,j)}^{vq_y} - \mathcal{F}_{(i,j-1)}^{vq_y}}{\Delta y} - \frac{\mathcal{F}_{(i+1,j)}^{uq_y} - \mathcal{F}_{(i,j)}^{uq_y}}{\Delta x} - g \frac{h_{(i,j)}^2 - h_{(i,j-1)}^2}{\Delta y} \quad (2.32)$$

This numerical model is an improved version of the numerical scheme by Pinilla et al. (2010).

## 2.5 Simulation for the Shear Instabilities

The simulation for the shear instabilities starts from a small perturbation of wave length  $\lambda_x$  to the base flow with a hyperbolic tangent (TANH) velocity profile:

$$U = \frac{1}{2}(U_1 + U_2) + \frac{1}{2}(U_1 - U_2) \tanh \frac{2y}{\delta_{\omega o}} \quad (2.33)$$

The velocity is  $U_1$  on one side of the base flow as  $y/\delta_{\omega o} \rightarrow +\infty$ , and is  $U_2$  as  $y/\delta_{\omega o} \rightarrow -\infty$ . Figure 2-5 shows the computational domain. The length scale of the velocity profile is the vorticity thickness  $\delta_{\omega o}$  defined by the maximum velocity gradient at the inflection,  $\hat{U}_y$ , as follows:

$$\delta_{\omega o} = \frac{U_1 - U_2}{\hat{U}_y} \quad (2.34)$$

The water depth of the base flow is constant, that is  $h = H$ . The wave speeds on both sides of the free stream are  $c_1 = c_2 = \sqrt{gH}$ . The dimensionless parameters are the velocity ratio  $\Gamma$  and convective Froude number  $\text{Fr}_c$  respectively, defined as follows:

$$\Gamma = \frac{U_1 - U_2}{U_1 + U_2} \quad \text{and} \quad \text{Fr}_c = \frac{U_1 - U_2}{c_1 + c_2} \quad (2.35)$$

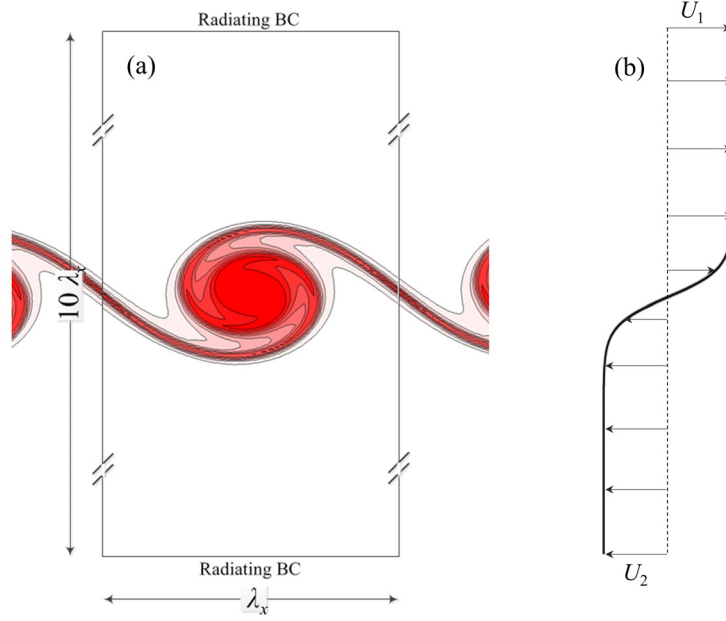


Figure 2-5: (a) Computational domain for simulation of the shear instabilities with periodic boundary condition in  $x$  direction and radiating boundary conditions at  $y = -5\lambda_x$  and  $y = +5\lambda_x$ . (b) TANH velocity profile.

The shear instabilities do not depend on the velocity ratio  $\Gamma$ . The convective Froude numbers considered in the present simulations are  $\text{Fr}_c = 0.1$  and  $0.8$ . The dimensions of the computational domain are  $\lambda_x$  in the  $x$ -direction and  $10\lambda_x$  in the  $y$ -direction. Periodic boundary conditions are applied over one wave length  $\lambda_x$ . The radiation boundary conditions are:

$$v(y^+) = c_1 \frac{h(y^+) - H}{H} \quad \text{as } y \rightarrow y^+ \quad \text{and} \quad v(y^-) = -c_2 \frac{h(y^-) - H}{H} \quad \text{as } y \rightarrow y^- \quad (2.36)$$

These boundary conditions allow the waves to escape without reflection at  $y = y^+ = 5\lambda_x$  and  $y = y^- = -5\lambda_x$ . The linearized shallow-water equations admit the normal-

mode solution for the disturbance

$$(h', u', v') = [h(y), u(y), v(y)] \exp[ik_x(x - ct) + \alpha t] \quad (2.37)$$

where  $k_x$  is the longitudinal wave number,  $c$  is the wave speed and  $\alpha$  is the exponential rate of the growth of the perturbation. In the linear stage of the instability's development, the amplitude of the disturbance is small. The rate of its growth is exponential. Most previous studies of linear stability were carried out using the Normal Mode Approach (NMA). In the NMA, the stability analysis is an eigenvalue problem of linearized shallow-water equations, see, e.g., Drazin & Howard (1966). In this paper, numerical simulations are conducted using fully nonlinear shallow-water equations. The fully nonlinear method is validated by comparing the simulations with the previous results obtained using the NMA.

The numerical simulations calculate the velocity  $u'$  and  $v'$  of the disturbance and its kinetic energy  $K' = \frac{1}{2}(u'^2 + v'^2)$ . Waves are allowed to escape from the computational domain without reflection through the radiating boundary condition, equation (2.36). The convenience of the radiation boundary condition in the numerical simulation is a significant advantage over the conventional NMA for linear instability analysis.

The average of the kinetic energy over the entire computation domain is

$$\overline{\overline{K'}} = \frac{1}{\lambda_x} \int_o^{\lambda_x} \frac{1}{\delta_{\omega o}} \int_{y^-}^{y^+} K' dy dx \quad (2.38)$$

The velocity  $u'$  and  $v'$  grow exponentially with time in the linear stage of its development. The kinetic energy  $\overline{\overline{K'}}$  also grows exponentially. Since  $u'$  and  $v'$  are

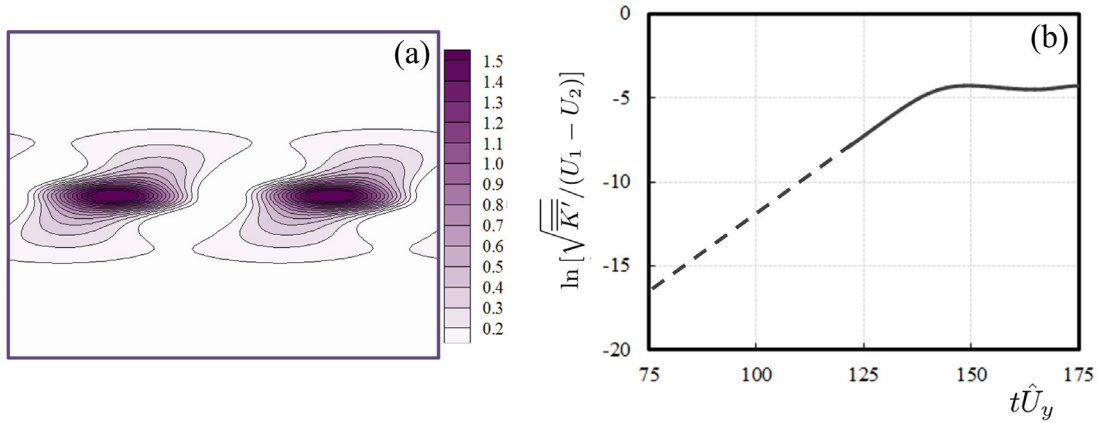


Figure 2–6: (a) Contours of the disturbances’ kinetic energy  $K'/\overline{K'}$  on the  $x$ - $y$  plane obtained for  $k_x = 0.893$  and  $\text{Fr}_c = 0.1$  at  $t\hat{U}_y = 75$  in the initial stage, when the development is governed by linear equations. (b) The growth of  $\sqrt{K'}/(U_1 - U_2)$  with time  $t\hat{U}_y$  on a semi-logarithmic scale. The red portion of the line delineates the fractional growth rate  $\alpha$ . Results are obtained for  $\lambda_x/\Delta x = 128$ , using 5<sup>th</sup>-order WENO reconstruction scheme.

proportional to  $\exp\{\alpha t\}$ , the kinetic energy  $\overline{K'}$  is proportional to  $\exp\{2\alpha t\}$ . The fractional increase of  $\sqrt{\overline{K'}}$  therefore determines  $\alpha$  as follows:

$$\alpha = \frac{1}{\sqrt{\overline{K'}}} \frac{d\sqrt{\overline{K'}}}{dt} \quad (2.39)$$

Figure 2–6(a) shows the disturbance’s kinetic energy obtained for one simulation of the disturbance, with wave number  $k_x = 0.893$  and convective Froude number  $\text{Fr}_c = 0.1$  at the dimensionless time of  $t\hat{U}_y = 75$ . The curve in Figure 2–6(b) shows the increase of  $\sqrt{\overline{K'}}$  with time  $t\hat{U}_y$ . The red-colored portion of the curve delineates the initial stage when the disturbance’s amplitude is small. The initial development is governed by the linearized equation. The fractional growth rate  $\alpha$  is determined

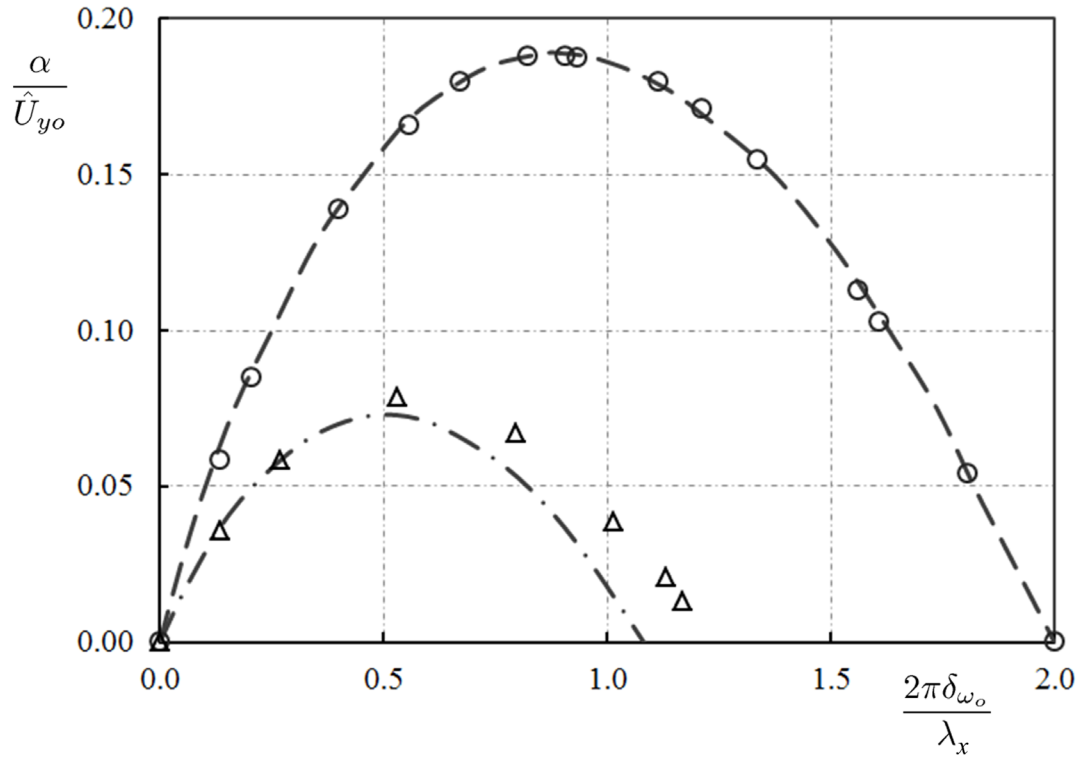


Figure 2-7: The growth rate  $\alpha/\hat{U}_y$  versus wave number  $k$  in the linear stage of the shear-layer development for  $Fr_c = 0.1$  ( $\circ$ ) and  $Fr_c = 0.8$  ( $\triangle$ ). Results for  $Fr_c = 0.1$  and  $0.8$  are obtained for  $\lambda_x/\Delta x = 128$  and  $256$  respectively, using  $5^{th}$ -order WENO reconstruction scheme. The open symbols represent current numerical simulation and dashed lines are the linear stability analysis obtained for compressible gas for convective Mach numbers  $Ma_c = 0.01$  and  $Ma_c = 0.8$  by Sandham & Reynolds (1990).

by Equation (2.39) using the data in this initial stage of development. The rate is a function of wave number  $k_x$  and the convective Froude number  $Fr_c$ .

Figure 2-7 shows the dependence of  $\alpha$  on  $k$  for the two Froude numbers  $Fr_c = 0.1$  and  $0.8$ . The simulation data for shear flow in shallow waters are compared with the growth rates obtained using the classical NMA by Sandham and Reynolds (1990) for the analogous shear flow of compressible gas. The dashed lines in the figure are the results obtained by Sandham & Reynolds (1990) for the convective Mach numbers

of  $\text{Ma}_c = 0.1$  and  $0.8$ . The convective Mach number is  $\text{Ma}_c = (U_1 - U_2)/(c_1 + c_2)$  defined by the speeds of sound at the free streams,  $c_1$  and  $c_2$ . The shallow-water equations are identical to 2D gas dynamic equations when the specific heat ratio of the gas  $\gamma = 2$ , see, e.g, Liggett (1994). The results provided in Figure 2–7 are obtained from simulations using a refined grid of 128 and 256 nodes over one wave length. The accuracy of these results is determined from a grid refinement study.

### 2.5.1 Grid Refinement and Convergence

For the grid refinement study, the parameter evaluated from the simulations of the linear instabilities is the maximum growth rate  $\hat{\alpha}$ . As shown in figure 2–7, this maximum rate  $\hat{\alpha}$  occurs at a wave number  $k_x = 0.89$  for the convective Froude number  $\text{Fr}_c = 0.1$ , and at a wave number  $k_x = 0.51$  for the convective Froude number  $\text{Fr}_c = 0.8$ . Simulations for this parameter  $\hat{\alpha}$  have been conducted using progressively smaller grid sizes. For  $\text{Fr}_c = 0.1$ , the number of grids per wave length are  $N = \lambda_x/\Delta = 32, 64, 128, 256$ . The corresponding number of grids over one vorticity thickness are  $\delta_{\omega_o}/\Delta = 4.545, 9.091, 18.182, \text{ and } 36.364$ . For  $\text{Fr}_c = 0.8$ , the number of grids per wave length are  $N = \lambda_x/\Delta = 64, 128, 256, 512$ . The corresponding number of grids over one vorticity thickness are  $\delta_{\omega_o}/\Delta = 5.154, 10.309, 20.619, \text{ and } 41.237$ . The approximate numbers of grids per vorticity thickness are the same for the two series of simulations with different convective Froude numbers. Table 2–2 summarizes the simulation results obtained from the progressively smaller grid sizes. The order of convergence as the grid is refined is determined from extrapolation formulae given in Stern *et al.* (2001). For each group of  $(\hat{\alpha}_{k-1}, \hat{\alpha}_k, \hat{\alpha}_{k+1})$  obtained

	Fr <sub>c</sub> = 0.1					Fr <sub>c</sub> = 0.8				
	<i>N</i>	$\delta_\omega/\Delta x$	$\hat{\alpha}/\hat{U}_y$	FE(%)	Order	<i>N</i>	$\delta_\omega/\Delta x$	$\hat{\alpha}/\hat{U}_y$	FE(%)	Order
WENO	32	4.545	0.17603	6.1636	—	64	5.154	0.07225	6.4172	—
	64	9.091	0.18545	1.1420	2.53	128	10.309	0.07639	1.0548	2.74
	128	18.182	0.18707	0.2785	2.04	256	20.619	0.07701	0.2531	2.06
	256	36.364	0.18747	0.0680	—	512	41.237	0.07716	0.0607	—
				<b>0.18759</b>	0	—			<b>0.07720</b>	
ULTRA-QUICK	32	4.545	0.17044	9.3103	—	64	5.154	0.06940	10.1065	—
	64	9.091	0.18545	1.3247	3.50	128	10.309	0.07576	1.8749	2.53
	128	18.182	0.18677	0.6213	1.09	256	20.619	0.07686	0.4475	2.07
	256	36.364	0.18739	0.2913	—	512	41.237	0.07712	0.1068	—
				<b>0.18794</b>	0			<b>0.07720</b>		
MINMOD	32	4.545	0.18312	2.3737	—	64	5.154	0.07757	0.4857	—
	64	9.091	0.18837	0.4230	N/A	128	10.309	0.07824	1.3536	N/A
	128	18.182	0.18775	0.0919	2.20	256	20.619	0.07743	0.3017	2.16
	256	36.364	0.18761	0.0199	—	512	41.237	0.07725	0.0673	—
				<b>0.18757</b>				<b>0.07720</b>		

Table 2-2: Grid size, fractional error and order of convergence obtained from the simulations of the linear shear instabilities using the 5<sup>th</sup>-order WENO, 3<sup>rd</sup>-order ULTRA-QUICK and 2<sup>nd</sup>-order MINMOD. The boldface numbers in the table are the values obtained from the extrapolation to  $\Delta x \rightarrow 0$ .

from three grid sizes, the formula for the order of convergence is

$$P_k = \frac{1}{\ln r} \ln \left[ \frac{\hat{\alpha}_k - \hat{\alpha}_{k-1}}{\hat{\alpha}_{k+1} - \hat{\alpha}_k} \right] \quad (2.40)$$

where  $r = \Delta_k/\Delta_{k+1}$ . In the present refinement of the grid  $r = 2$ , the extrapolated value is

$$\hat{\alpha}_{\Delta x \rightarrow 0} = \frac{r^{P_k} \hat{\alpha}_{k+1} - \hat{\alpha}_k}{r^{P_k} - 1}. \quad (2.41)$$

The results for infinitely small grid sizes,  $\hat{\alpha}_{\Delta x \rightarrow 0}$ , are extrapolated from the group of the finest three grids. The boldface numbers in the table are the values obtained from the extrapolation to  $\Delta x \rightarrow 0$ . The Fractional computational Error in percentage is

$$\text{FE}(\%) = \frac{|\hat{\alpha} - \hat{\alpha}_{\Delta x \rightarrow 0}|}{\hat{\alpha}_{\Delta x \rightarrow 0}} \times 100 \quad (2.42)$$

The results in Table 2-2 are somewhat unexpected. The fractional computation error of  $2^{nd}$ -order MINMOD is consistently lower than the two higher-order computational schemes WENO and ULTRA-QUICK. The accuracy of MINMOD is particularly impressive in the simulations obtained using the coarse grid when the number of nodes is only 4.5 to 5.1 ( $N = 64$  for  $\text{Fr}_c = 0.8$ ) across the vorticity thickness. The fractional computational error of MINMOD is only  $\text{FE}(\%) = 2.4$  percent using the coarse grid  $N = 32$  when  $\text{Fr}_c = 0.1$ , and only  $\text{FE}(\%) = 0.48$  percent for the coarse grid  $N = 64$  when  $\text{Fr}_c = 0.8$ .

The numerical computational error therefore is not dependent on the order of the interpolation for the nonlinear fluxes. In the present formulation using the staggered grid, the approximation to the pressure gradient force is only second order in accuracy. The false diffusion known to be associated with MINMOD seems to have

helped with the numerical simulations. In the linear stages of the shear instabilities' development, the nonlinear fluxes in the momentum equations are small compared with the dominant pressure gradient force. On the staggered grid, the approximation for the pressure gradient is accurate to the second order.

Figure 2–8 plots the fractional computation errors in percentage on a logarithmic scale. The order of convergence as delineated by the slope of the dash line on the logarithmic plots are approximately second order for all simulations using different flux-limiting schemes. These results are consistent with the explanation that in the initial linear stage of development, when the velocity fluctuations associated with the perturbation are small compared with the velocity in the base flow, the dominant force is the pressure gradient force, not the nonlinear fluxes.

## 2.6 Nonlinear Development

The nonlinear development of shear instabilities begins when the mean flow is modified by the growth of the perturbation, as the velocity of the disturbance becomes comparable to the velocity of the base flow. Figure 2–9 shows the formation of an eddy associated with the maximum growth of the instabilities at the wave number  $k_x = 0.89$  for convective Froude number  $Fr_c = 0.1$ . Figure 2–10 shows the formation of a “shocklet” associated with the maximum growth at the wave number  $k_x = 0.51$  for convective Froude number  $Fr_c = 0.8$ . Shock waves are characteristics of the processes in a shocklet that are to be distinguished from the roll-up of the vorticity in an eddy. The presence of shock waves has been observed in numerical simulation of shear instabilities and compressible turbulence in the analogous problems in gas

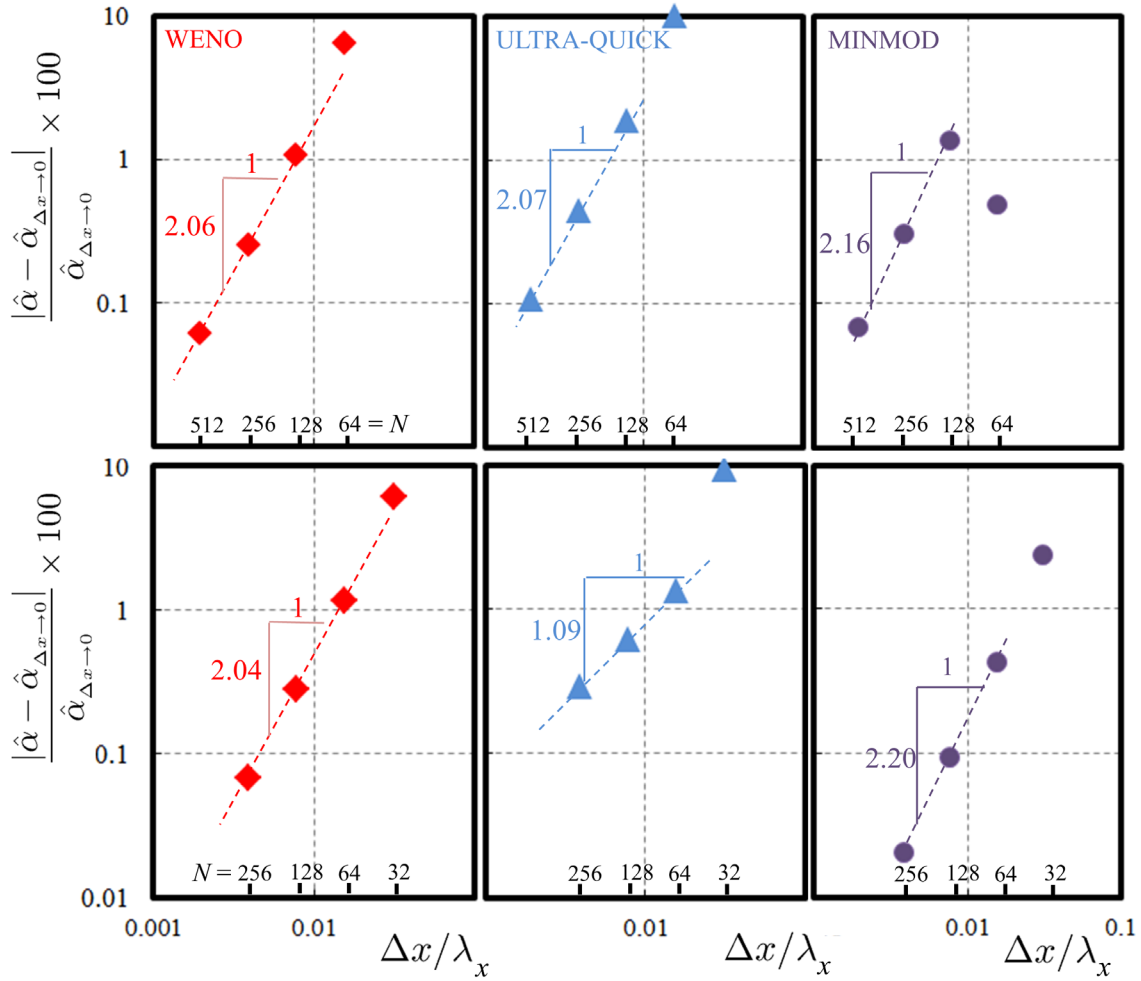


Figure 2-8: The convergence of the maximum growth rate  $\hat{\alpha}$  at the wave number  $k_x = 2\pi\delta_{\omega 0}/\lambda_x = 0.51$  for  $Fr_c = 0.8$  (top row), and the maximum rate  $\hat{\alpha}$  at  $k_x = 0.89$  for  $Fr_c = 0.1$  (bottom row). The fractional errors are plotted versus the grid size for the fifth-order WENO (left), third-order ULTRA-QUICK (centre) and second-order MINMOD (right) schemes.

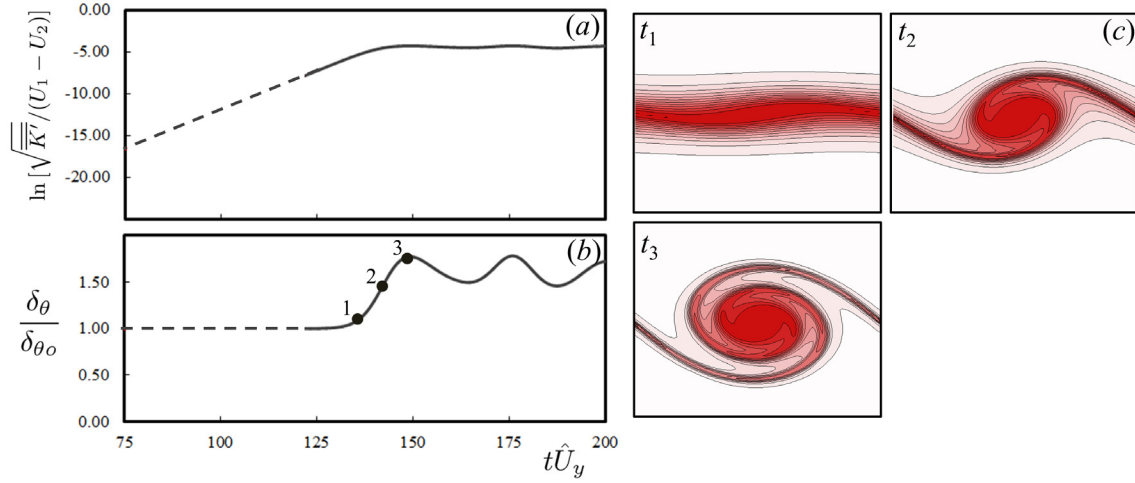


Figure 2-9: The maximum growth of the instability to form an eddy at  $k_x = 0.89$  for  $Fr_c = 0.1$ . (a) Disturbance kinetic energy ( $\sqrt{K'}/(U_1 - U_2)$ ) versus time  $t\hat{U}$  in semi-logarithmic scale. (b) Momentum Thickness,  $\delta_\theta/\delta_{\theta_o}$ . (c) Vorticity contour on the  $x$ - $y$  plane at the times  $t_1$ ,  $t_2$  and  $t_3$  as marked in (b) of the figure. The first pinnacle of the momentum thickness  $\hat{\delta}_\theta$  in the nonlinear stage occurs at time  $t_3$ .

dynamics by Sandham & Reynolds (1989) and Lee *et al.* (1991). The vorticity thickness and the momentum thickness are the parameters that characterize the modification, and are the parameters to be examined for dependency on the grid size. The vorticity thickness is defined by the mean velocity gradient at the inflection

$$\delta_\omega = \frac{U_1 - U_2}{(d\bar{U}/dy)_{\max}} \quad (2.43)$$

The mean velocity  $\bar{U}$  is obtained by averaging the  $x$ -component of the velocity over its wave length:

$$\bar{U}(y) = \frac{1}{\lambda_x} \int_0^{\lambda_x} u(x, y) dx \quad (2.44)$$

The vorticity thickness is sensitive to minor irregularity at the inflection. We shall use the momentum thickness  $\delta_\theta$  to evaluate the performance of the numerical scheme.

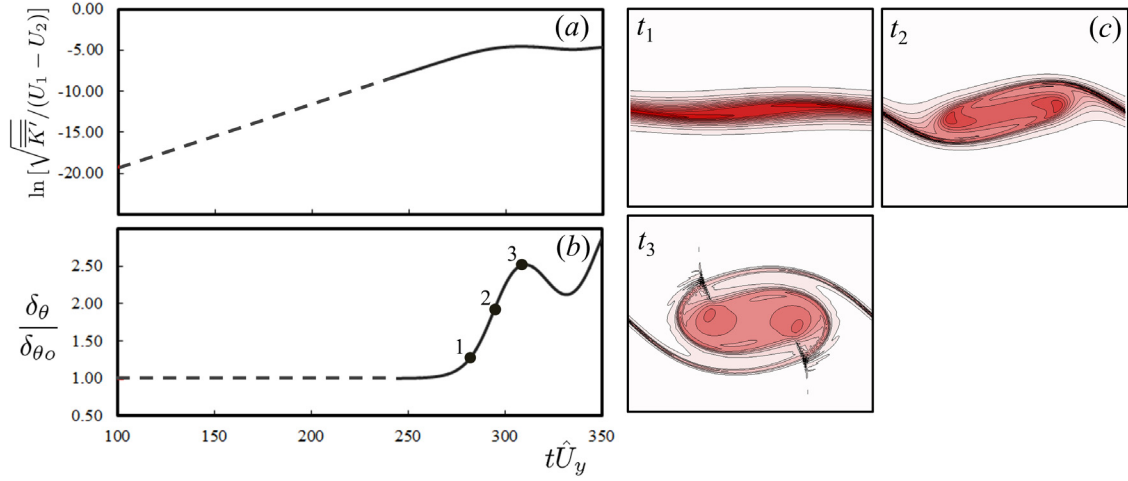


Figure 2–10: The maximum growth of the instability to produce a shocklet at  $k_x = 0.51$  for  $\text{Fr}_c = 0.8$ . (a) Disturbance kinetic energy ( $\sqrt{\overline{K'}}/(U_1 - U_2)$ ) versus time  $t\hat{U}$  in semi-logarithmic scale. (b) Momentum Thickness  $\delta_\theta/\delta_{\theta_0}$ . (c) Vorticity contour on the  $x$ - $y$  plane at the times  $t_1$ ,  $t_2$  and  $t_3$  as marked in (b) of the figure. Shock waves with a sudden jump in depth and velocity are observed in the shocklet as the momentum thickness reaches its first pinnacle at time  $t_3$ .

By definition the momentum thickness is:

$$\delta_\theta = \int_{-\infty}^{\infty} \frac{\bar{U} - U_2}{U_1 - U_2} \left( 1 - \frac{\bar{U} - U_2}{U_1 - U_2} \right) dy \quad (2.45)$$

The ratio of the vorticity thickness and momentum thickness is  $\delta_\omega/\delta_\theta \simeq 4$  and exactly equal to 4 for the unperturbed TANH velocity profile.

The nonlinear development of the momentum thickness  $\delta_\theta$ , normalized by its initial value  $\delta_{\theta_0}$ , for three different times,  $t_1$ ,  $t_2$  and  $t_3$ , are marked in part (b) of Figures 2–9 and 2–10. The corresponding vorticity contours are shown on the right-hand side of these figures. The momentum thickness increases with time. It reaches the first pinnacle with a peak value  $\hat{\delta}_\theta$  at time  $t_3$ . For the convective Froude

number  $\text{Fr}_c = 0.1$ , peak values  $\hat{\delta}_\theta$  at the pinnacle are calculated using progressively refined grid sizes of  $N = \lambda_x/\Delta = 32, 64, 128$  and  $256$ . For convective Froude number  $\text{Fr}_c = 0.8$ , the calculations are conducted using  $N = \lambda_x/\Delta = 64, 128, 256$  and  $512$ . The results of the calculations for  $\hat{\delta}_\theta$  are given to six decimal places in Table 2–3. The values of  $\hat{\delta}_{\Delta x \rightarrow 0}$ , obtained from extrapolation for infinitely small grid sizes are also included as the boldface numbers in the table. For each group of  $(\hat{\delta}_{\theta \ k-1}, \hat{\delta}_{\theta \ k}, \hat{\delta}_{\theta \ k+1})$  obtained from three grid sizes, the order of convergence  $P_k$  and the extrapolated solution of  $\hat{\delta}_{\theta \Delta x \rightarrow 0}$  are determined by the formulae of Stern *et al.* (2001) as follows:

$$P_k = \frac{1}{\ln r} \ln \left[ \frac{\hat{\delta}_{\theta \ k} - \hat{\delta}_{\theta \ k-1}}{\hat{\delta}_{\theta \ k+1} - \hat{\delta}_{\theta \ k}} \right] \quad (2.46)$$

$$\hat{\delta}_{\theta \Delta x \rightarrow 0} = \frac{r^{P_k} \hat{\delta}_{\theta \ k+1} - \hat{\delta}_{\theta \ k}}{r^{P_k} - 1} \quad (2.47)$$

where  $r = \Delta_k/\Delta_{k+1}$ . The Fractional computational Error in percentage is

$$\text{FE}(\%)_k = \frac{|\hat{\delta}_{\theta \ k} - \hat{\delta}_{\theta \Delta x \rightarrow 0}|}{\hat{\delta}_{\theta \Delta x \rightarrow 0}} \times 100 \quad (2.48)$$

Inspecting the results for the nonlinear instabilities in this table has produced a different impression from the previous table for linear instabilities. The 5<sup>th</sup>-order WENO is now the most accurate of all schemes. The 2<sup>nd</sup>-order MINMOD, on the other hand, is the least accurate scheme, producing the highest fractional error. Furthermore, the computational error is now dependent on the convective Froude number. The fractional error in the simulation for the nonlinear processes at the higher convective Froude number of  $\text{Fr}_c = 0.8$  is an order of magnitude greater. The radiation of waves from the instabilities and the dissipation of energy across the shock waves

	Fr <sub>c</sub> = 0.1					Fr <sub>c</sub> = 0.8				
	<i>N</i>	$\delta_{\omega_o}/\Delta x$	$\delta_{\theta}/\delta_{\theta_o}$	FE(%)	Order	<i>N</i>	$\delta_{\omega_o}/\Delta x$	$\delta_{\theta}/\delta_{\theta_o}$	FE(%)	Order
WENO	32	4.545	1.7098	3.5707	—	64	5.154	2.1437	15.1016	—
	64	9.091	1.7684	0.2665	3.68	128	10.309	2.4628	2.4638	2.44
	128	18.182	1.7730	0.0084	4.97	256	20.619	2.5214	0.1434	4.10
	256	36.364	1.7731	0.0003	—	512	41.237	2.5248	0.0083	—
				<b>1.7731</b>					<b>2.5250</b>	
ULTRA-QUICK	32	4.545	1.6889	4.7647	—	64	5.154	2.1893	13.3139	—
	64	9.091	1.7606	0.7177	2.70	128	10.309	2.4701	2.1919	2.54
	128	18.182	1.7717	0.0952	2.91	256	20.619	2.5184	0.2829	2.95
	256	36.364	1.7731	0.0126	—	512	41.237	2.5246	0.0365	—
				<b>1.7734</b>					<b>2.5255</b>	
MINMOD	32	4.545	1.6449	7.2332	—	64	5.154	2.1893	13.2834	—
	64	9.091	1.7513	1.2184	2.66	128	10.309	2.3107	8.4734	-0.40
	128	18.182	1.7681	0.2704	2.17	256	20.619	2.4720	2.0850	2.02
	256	36.364	1.7719	0.0600	—	512	41.237	2.5117	0.5131	—
				<b>1.7729</b>					<b>2.5246</b>	

Table 2–3: Grid size, fractional error and order of convergence obtained for the momentum thickness from simulations of nonlinear shear instabilities using 5<sup>th</sup>-order WENO, 3<sup>rd</sup>-order ULTRA-QUICK and 2<sup>nd</sup>-order MINMOD. The boldface numbers in the table are the values obtained from the extrapolation to  $\Delta x \rightarrow 0$ .

are processes of smaller-length scale that are associated with the nonlinear development of the instabilities at the higher convective Froude number. It is clear from the grid refinement study that relatively finer grid sizes are required for correct simulation of these smaller-scale processes. The nonlinear fluxes  $\mathcal{F}^{uq_x}$ ,  $\mathcal{F}^{vq_x}$ ,  $\mathcal{F}^{uq_y}$ ,  $\mathcal{F}^{vq_y}$  are the dominant terms in the shallow-water equations in numerical simulations for nonlinear instabilities. It is not surprising therefore that the numerical computational error is decided by the order of accuracy of the interpolation schemes for these nonlinear fluxes. Figure 2–11 shows the fractional computation errors for five interpolation schemes of different orders of accuracy. From left to right in the figure are the results obtained by progressively less accurate schemes. The approximate order of accuracy of these schemes is as follows: 5<sup>th</sup>-order WENO, 3<sup>rd</sup>-order QUICK, 3<sup>rd</sup>-order ULTRA-QUICK, 2<sup>nd</sup>-order SUPERBEE, 2<sup>nd</sup>-order MINMOD.

## 2.7 Summary and Conclusion

The simulations for the shear instabilities in this paper have demonstrated how flux-limiting strategies are implemented on a staggered grid. Through the use of the grid-refinement study, the accuracy for each of the flux-limiting strategies is evaluated for (i) the linear stage of the shear instabilities, and then (ii) the nonlinear aspect of the instabilities' development. The overall accuracy of the simulations is dependent on the one hand on interpolation of the pressure gradient on the staggered grid, and on the other hand on the approximation of the nonlinear fluxes. In the linear stage of the shear instabilities' development, the overall order of accuracy is decided by the interpolation of the pressure gradient on the staggered grid. In the nonlinear stage

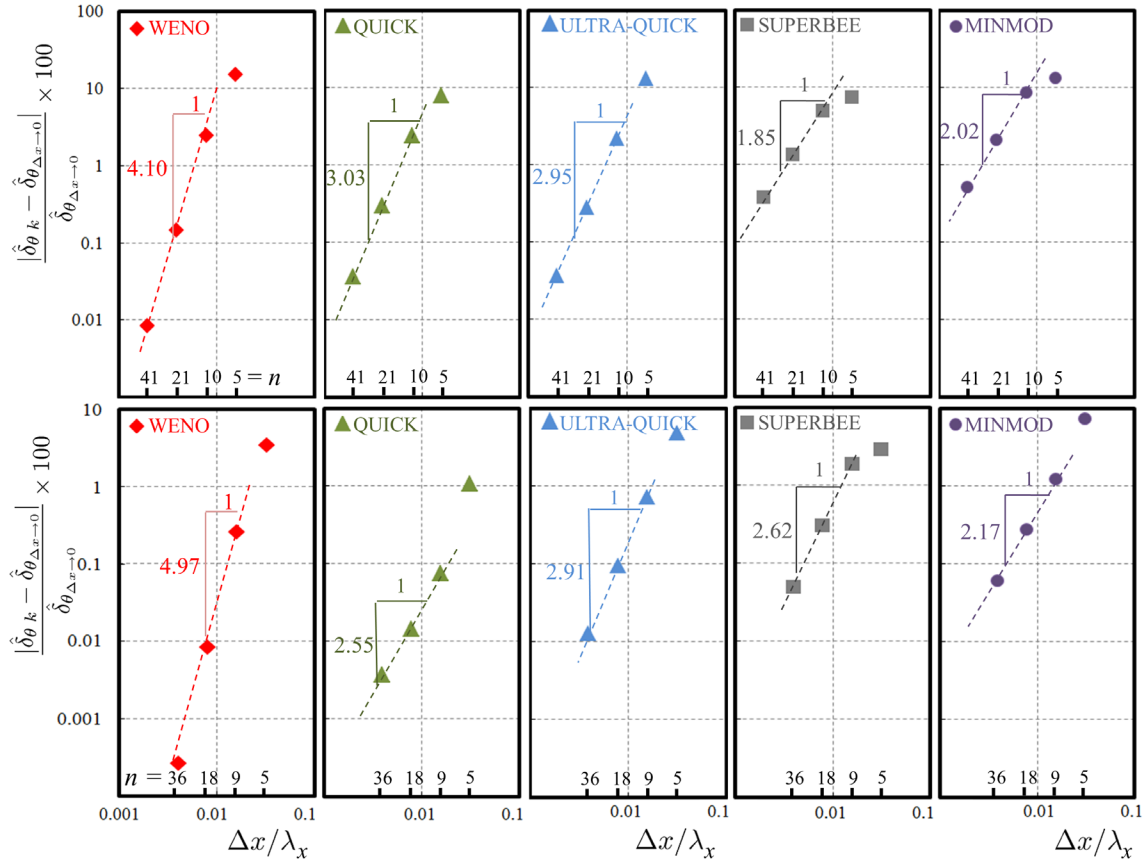


Figure 2-11: The convergence of the nonlinear simulation for the momentum thickness by five progressively less accurate interpolation schemes. From the left to right in the figure are the results obtained by WENO, QUICK, ULTRA-QUICK, SUPERBEE, MINMOD. The top row shows results for  $Fr_c = 0.8$  and the bottom row for  $Fr_c = 0.1$ .

of development, the overall order of accuracy is determined by the approximation of the nonlinear fluxes. Accuracy of the nonlinear simulation is higher in the case of small convective Froude number  $Fr_c = 0.1$ . The fractional error for simulations of nonlinear instabilities at the higher convective Froude number of  $Fr_c = 0.8$  is an order of magnitude greater than is the case for the smaller convective Froude number of  $Fr_c = 0.1$ . The radiation of waves and the dissipation of energy are small-scale processes. Finer grid is required for capturing these small scales in the shear flow of higher convective Froude numbers.

The four-digit accuracy of the numerical simulations presented in this paper is comparable to analytical solutions. The development of this reliable numerical-simulation method paves the way for further study of the instabilities in shear flows that radiate waves. Calculations for the nonlinear interaction between multiple eddies and shocklets are to be reported in a future publication.

## CHAPTER 3 TRANSVERSE DAM-BREAK WAVES

S. Karimpour Ghannadi and V. H. Chu. Transverse Dam Break Wave. *Journal of Fluid Mechanics*, Volume 758, November 2014, R2 (12 pages).

### 3.1 Abstract

Numerical simulations of the transverse dam-break waves produced by the sudden removal of a gate on the side of a waterway are conducted based on the shallow-water equations to find solutions to a family of water-diversion problems. The Froude numbers in the main flow identify the members of the family. The depth and discharge profiles are analysed in terms of Ritter's similarity variable. For subcritical main flow, the waves are comprised of a supercritical flow expansion followed by a subcritical outflow. For supercritical main flow on the other hand, the waves are analogous to the Prandtl-Meyer expansion in gas dynamics. The diversion flow rate of the two-dimensional transverse dam-break waves on a flat bed is 55% greater than the one-dimensional flow rate of Ritter in the limiting case of zero main flow, and approaches the rate of Ritter in the other limit when the value of the Froude number in the main flow approaches infinity. The diversion flow rate over weir is generally higher than the rate over the flat bed depending on the Froude number of the main flow. These numerical simulation results are consistent with the laboratory observations.

**Keywords:** Flow Diversion, Open-Channel Flow, Dam-break Waves, Prandtl-Meyer Expansion, Numerical Simulation

### 3.2 Introduction

The diversion of water from the main flow to the side is a ubiquitous occurrence in natural and man-made waterways. It has found applications in irrigation, in flood control, and in the municipal and industrial conveyance of water. The engineering design for diversion structures has been dependent on empirical formulae and more recently on numerical simulations. For the diversion flow over a side weir, Subramanya & Awasthy (1972) proposed semi-empirical discharge formulae based on laboratory experimental data. Mizumura *et al.* (2003), on the other hand, acquired experimental data and formulated the supercritical flow diversion on a flat bed using the analogy between open-channel hydraulics and gas dynamics. Ritter (1892) introduced a similarity variable in his solution to the one-dimensional (1D) dam-break wave problem.

This paper describes numerical simulations conducted to study the diversion of water from the main flow. The results are analysed as a family of Transverse Dam-break Waves (TDWs) defined by the Froude number of the main flow. When correctly implemented, numerical simulation can be accurate and can provide in-depth understanding that is equal to analytical methods. The present simulation complements a number of recent works on related dam-break waves, by Hogg & Pritchard (2004), Vazquez *et al.* (2008), Ghostine *et al.* (2013) and Mahmodinia *et al.* (2014).

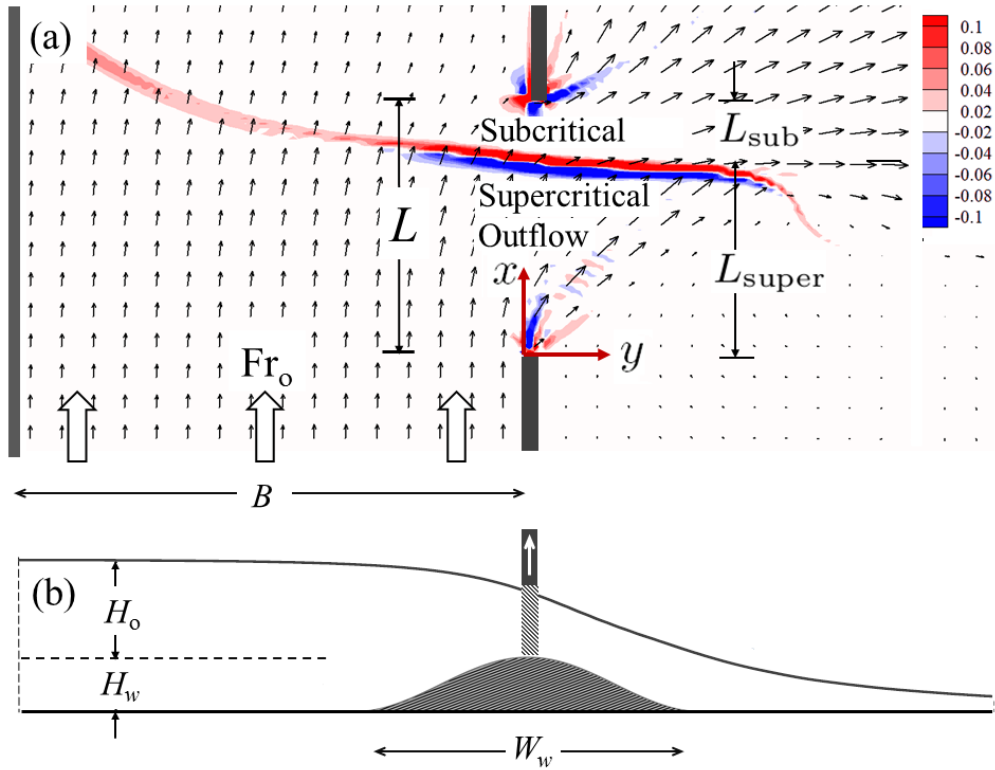


Figure 3–1: Transverse dam-break waves over a length of  $L$  on the side of the open-channel main flow. (a) The arrows show the velocity vector  $(u, v)$ . The sharp change in dilation  $(\partial u/\partial x + \partial v/\partial y)$  from blue to red marks the hydraulics jump as the outflow changes from supercritical to subcritical. The flow pattern shown is obtained from a simulation for the main-flow Froude number  $Fr_o = 0.63$ . The length along the opening of the supercritical outflow upstream of the jump is  $L_{\text{super}}$ . The length of the subcritical outflow is  $L_{\text{sub}}$ . (b) Cross-sectional profile of water depth and bottom elevation over a weir of height  $H_w$  and width  $W_w$ .

Figure 3–1 delineates the two-dimensional (2D) problem of the TDWs produced by the sudden removal of a gate on the side of a waterway. The height of the weir on the side is  $H_w$ . The undisturbed water level above the crest of the weir is  $H_o$ . The velocity and depth of the undisturbed main flow,  $U$  and  $H$ , define the Froude number of the main flow,  $Fr_o = U/\sqrt{gH}$ . The lateral outflow through the gate opening can be subcritical, supercritical or a combination of both.

The paper has six sections including this introductory section. Section 2 explains the numerical simulations and the implementation of the shock-capturing scheme for the simulations. The results for the family of TDWs are related on the one hand with the analogous problem of the Prandtl-Meyer expansion in gas dynamics and on the other hand with the classical 1D dam-break waves of Ritter (1892). Prandtl-Meyer expansion is a supersonic expansion wave of compressible gas along an outwardly bent wall, see, e.g., Liepmann & Roshko (2013). Sections 3 and 4 present the simulation results for the transient and steady-state development of the waves on a flat bed. In Section 5, the simulations are repeated for the TDWs over a weir. The simulations are compared with laboratory measurements. Summary and conclusion are given in the final section, 6.

### 3.3 Numerical Simulation

The simulations for the TDWs are based on numerical solutions of shallow-water equations:

$$\frac{\partial h}{\partial t} + \frac{\partial q_x}{\partial x} + \frac{\partial q_y}{\partial y} = 0 \quad (3.1)$$

$$\frac{\partial q_x}{\partial t} + \frac{\partial (uq_x)}{\partial x} + \frac{\partial (vq_x)}{\partial y} = -gh \frac{\partial (h + z_o)}{\partial x} \quad (3.2)$$

$$\frac{\partial q_y}{\partial t} + \frac{\partial (uq_y)}{\partial x} + \frac{\partial (vq_y)}{\partial y} = -gh \frac{\partial (h + z_o)}{\partial y} \quad (3.3)$$

where  $h$  = flow depth,  $z_o$  = channel-bottom elevation,  $g$  = gravity,  $(u, v)$  = velocity components,  $(q_x, q_y) = (uh, vh)$  = discharge components in the  $x$  and  $y$  directions, respectively. For flow on a flat bed ( $z_o = 0$ ), these shallow-water equations are

identical to 2D gas-dynamic equations when the specific heat ratio is 2; see e.g., Liggett (1994).

An improved version of the numerical scheme by Pinilla *et al.* (2010) is used for the numerical simulations. A staggered grid defines the nodal values for  $h$ ,  $q_x$  and  $q_y$  in the computational domain. The MINMOD flux limiter determines the momentum fluxes on the faces of the finite volume. This maintains the stability of the computation by controlling the spurious numerical oscillations initiated across the hydraulic jump. A fourth-order Runge-Kutta scheme is employed for integration in time. The MINMOD flux limiter is known to be somewhat diffusive; see, e.g., Chu & Gao (2013). It is however acceptable for simulations for depth and velocity profiles that are not sensitive to false diffusion. Other flux limiters mentioned in Sweby (1984) have been used in this study but have produced no significant difference in results.

The numerical simulation starts with a given velocity  $U$  and depth  $H$  in the main channel. Removal of the gate on the side of length  $L$  produces the TDWs. For the flow profiles presented in this paper, the length of the opening on the side is  $L = 25$  m and the water depth is  $H_o = 1$  m. The width selected for the main channel is  $B = 8L$  for subcritical main flow ( $Fr_o < 1$ ). For supercritical main flow ( $Fr_o > 1$ ), the width is  $B = 8L/Fr_o$ . These widths are selected to avoid the effect of the wave reflection. There are 100 nodes over the length of the opening. The grid sizes therefore are  $\Delta x = \Delta y = L/100$ . Grid-refinement study has shown that this grid-size selection has a better than one percent accuracy on the discharge coefficient.

### 3.4 Transient Development toward the Steady State

Figures 3–2 and 3–3 show the transient development of the TDWs toward the steady state for main-flow Froude numbers of  $Fr_o = 0.03$  and  $0.63$ , respectively. There are three subsets of figures for each  $Fr_o$ . The top in each figure contains the depth  $h$ -profiles obtained on the center plane, where  $x = 0.5L$  for time  $t/t_s = 0.25, 0.75, 1.5$  and  $3.0$ . Figures 3–2(b) and 3–3(b) are the lateral outflow  $q_y$ -profiles on the center plane for the same period of time. The four images in 3–2(c) and 3–3(c) show the contours of the local Froude number  $Fr = \sqrt{u^2 + v^2}/\sqrt{gh}$  on the  $x$ - $y$  plane. The local Froude number  $Fr$  delineates the evolution of the flow due to the waves over a period of  $t/t_s = 0.25, 0.5, 1.0$  to  $1.5$ . The area of supercritical flow with  $Fr > 1$  is marked in red. The subcritical flow with  $Fr < 1$  is marked in grey. The critical flow section where  $Fr = 1$  is defined by the contour line between the red and the grey. The flow pattern changes rapidly with time. The time scale for the transient development is the communication time  $t_s = L/\sqrt{gH_o}$ , which is approximately the time needed for the wave of speed  $c = \sqrt{gH_o}$  to travel from one end of the gate opening to the other end. Immediately after the removal of the gate, the critical-flow contour is located at the gate where  $y = 0$ . The contour moves forward with time in the direction of the flow. In the case of a small main-flow Froude number of  $Fr_o = 0.03$  as shown in Figure 3–2, the outflow at the gate opening is subcritical as the flow approaches the steady state. At a higher main-flow Froude number of  $Fr_o = 0.63$  as shown in Figure 3–3, the outflow at the leading edge is a supercritical flow expansion followed by a subcritical outflow. The depth and velocity change rapidly across the jump from supercritical to subcritical outflow.

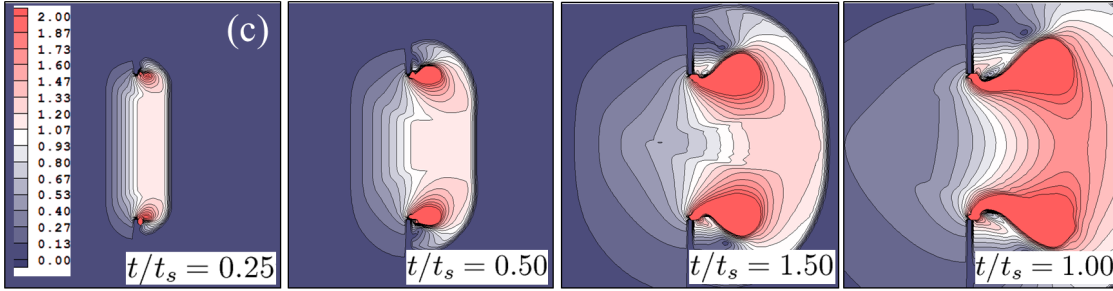
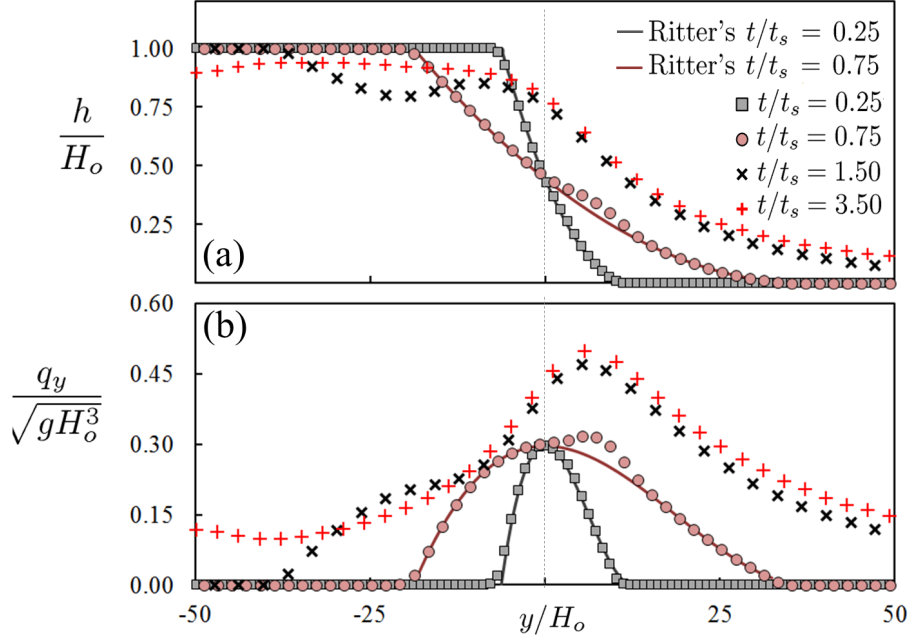


Figure 3-2: Transient development of TDWs on a flat bed for  $Fr_o = 0.03$  over the period from time  $t/t_s = 0.25$  to 3.00. (a) The depth and (b) lateral discharge (bottom left) profiles are obtained at the center of the opening where  $x = L/2$ . The contour lines in the images (c) define the local Froude number  $Fr = \sqrt{u^2 + v^2} / \sqrt{gh}$ . The red color marks the region of the supercritical flow ( $Fr > 1$ ).

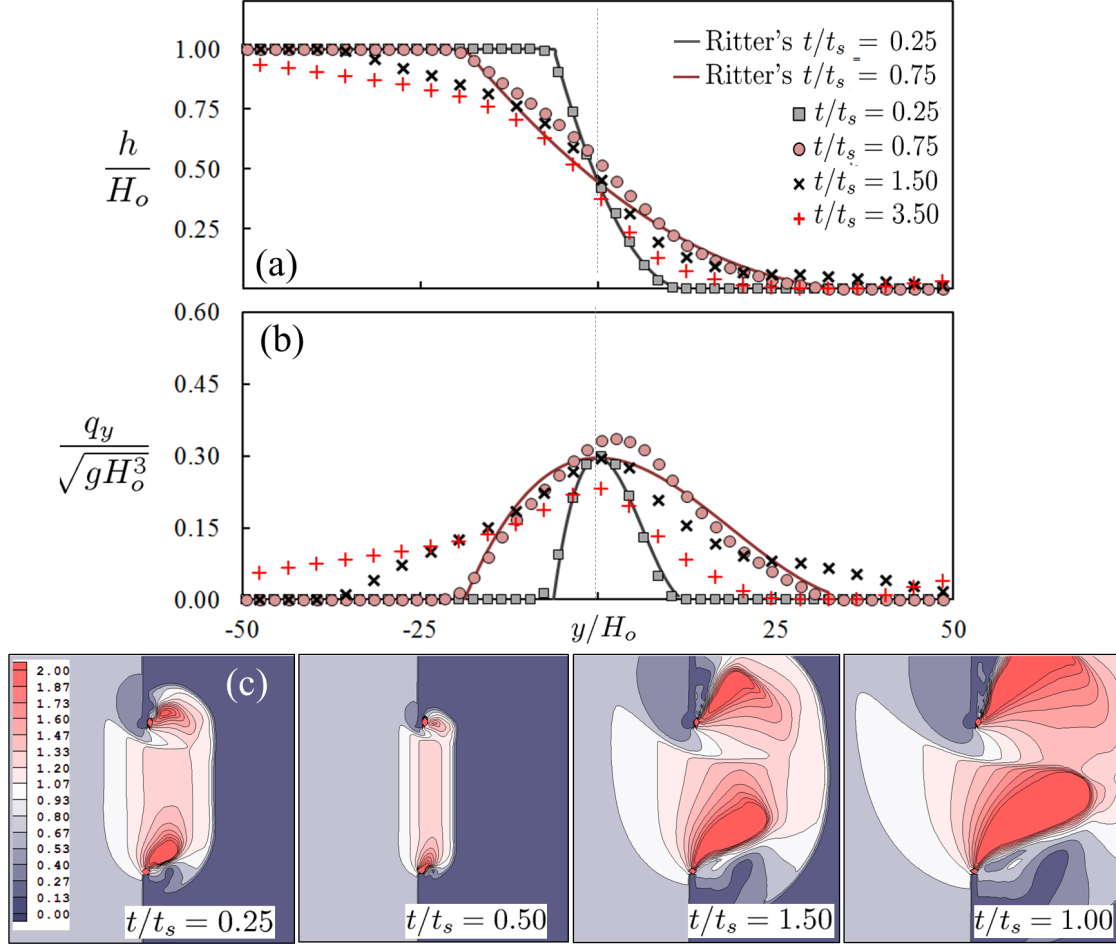


Figure 3-3: Transient development of TDWs on a flat bed for  $Fr_o = 0.63$  over the period from time  $t/t_s = 0.25$  to 3.00. (a) The depth and (b) lateral discharge (bottom left) profiles are obtained at the center of the opening where  $x = L/2$ . The contour lines in the images (c) define the local Froude number  $Fr = \sqrt{u^2 + v^2}/\sqrt{gh}$ . The red color marks the region of the supercritical flow ( $Fr > 1$ ).

### 3.4.1 1D Dam-break Waves of Ritter

The initial TDW profiles follow closely the one-dimensional (1D) dam-break wave profiles of Ritter (1892), which are the solid lines in Figures 3–2 and 3–3. These profiles remain close to the 1D solution of Ritter as long as the waves from the opposite edges of the opening have not reached the cross section. The later development of the 2D TDWs can also be described by Ritter’s similarity variable. A brief summary of the 1D solution of Ritter therefore is given in this sub-section for comparison with the 2D simulation results in later sections. The 1D wave does not have a steady state. The flow through the critical-flow section nevertheless stays constant throughout the development of the waves. The removal of the dam in the 1D channel produces a positive wave and a negative wave. The front of the positive wave advances with a velocity equal to  $v = 2\sqrt{gH_o}$ . The recessing edge has a negative velocity equal to  $v = -\sqrt{gH_o}$ . The similarity variable of Ritter is

$$R = \frac{y}{t\sqrt{gH_o}} \quad (3.4)$$

which unifies the space  $y$  and time  $t$  through the wave speed  $\sqrt{gH_o}$ . The profiles for the depth and discharge of the 1D wave expressed in terms of Ritter’s similarity variable are

$$\frac{h}{H_o} = \frac{1}{9}(2 - R)^2, \quad \frac{q_y}{\sqrt{gH_o^3}} = \frac{2}{27}(1 + R)(2 - R)^2 \quad \text{for } -1 < R < 2 \quad (3.5)$$

The depth and discharge profiles change rapidly with time. The profiles of Ritter are the solid lines, while numerical simulation results for the TDWs are the points in Figures 3–2 and 3–3. The local Froude number of the 1D solution according to

equation (3.5) is

$$\text{Fr}_y = \frac{q_y}{\sqrt{gh^3}} = \frac{2(1+R)}{2-R} \quad \text{for } -1 < R < 2 \quad (3.6)$$

At the gate where  $y = 0$  and  $R = 0$ , the flow is critical with  $\text{Fr}_y = 1$ . The depth and discharge of this critical flow are:

$$h = h_{\text{critical}} = \frac{4}{9}H_o, \quad (q_y)_{\text{critical}} = \frac{8}{27}\sqrt{gH_o^3}. \quad (3.7)$$

The discharge  $q_y$  is zero at the advancing front and the receding edge. The maximum discharge occurs at the critical-flow section:  $(q_y)_{\text{max}} = (q_y)_{\text{critical}}$ . The dimensionless discharge coefficient corresponding to this flow rate through the critical section is

$$q_{\text{Ritter}}^* = \frac{(q_y)_{\text{max}}}{\sqrt{gH_o^3}} = \frac{8}{27} \simeq 0.296. \quad (3.8)$$

Water moves through the critical section as it depletes on one side, filling the volume on the other side of the wave.

### 3.4.2 Discharge Coefficient of the 2D TDWs

The discharge coefficients of the 2D TDWs as shown in Figure 3–4 are comparable in magnitude to the 1D coefficient of Ritter. The flow through the gate opening is the integral of  $q_y$  over the the length of the opening,  $Q(t, \text{Fr}_o) = \int_o^L q_y(x, 0, t) dx$ . The corresponding discharge coefficient is  $Q^*(t, \text{Fr}_o) = Q/(L\sqrt{gH_o^3})$ . Immediately after the opening of the gate, all discharge coefficients are equal to the 1D value  $q_{\text{Ritter}}^* \simeq 0.296$ . The discharge coefficient increases with time for  $\text{Fr}_o < 0.63$  and decreases with time for  $\text{Fr}_o > 0.63$ . Steady state is reached within a very short period

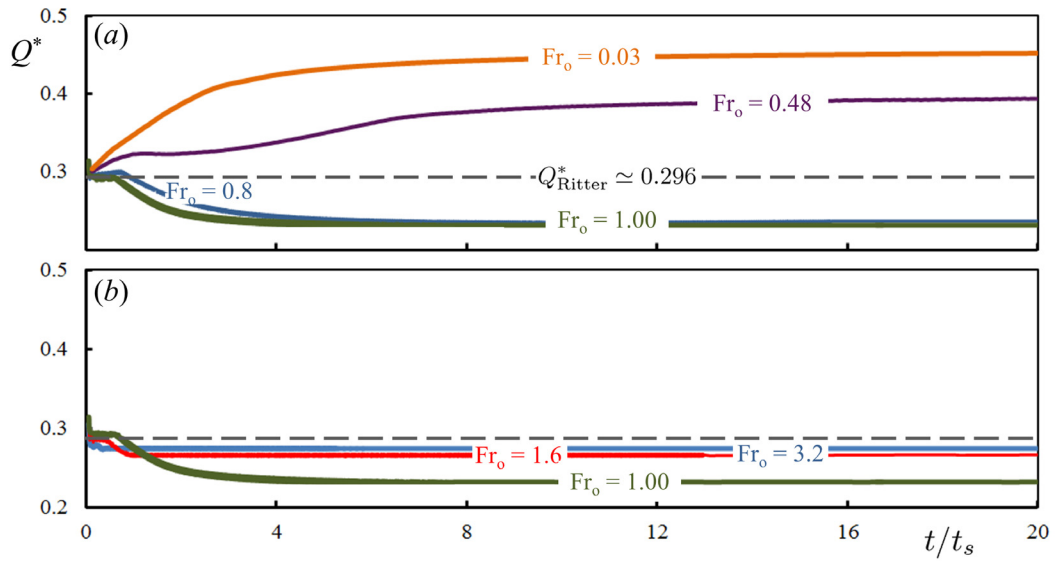


Figure 3–4: The discharge coefficient,  $Q^*(t, Fr_o)$ , and its dependence on the time  $t/t_s$  and on the main-flow Froude number  $Fr_o$ : (a) subcritical main flow with  $Fr_o < 1$ , (b) supercritical main flow with  $Fr_o > 1$ . The flow is considered to have reached steady state at time  $t = 10 t_s$  as the total flow rate  $Q^*$  has closely approached its asymptote at this time.

of time, particularly for supercritical main flow. For subcritical main flow ( $Fr_o < 1$ ), the discharge coefficient decreases as the main-flow Froude number,  $Fr_o$ , increases from 0 to about 0.9. For supercritical main flow ( $Fr_o \geq 1$ ) on the other hand, the discharge coefficient increases with the  $Fr_o$ .

### 3.5 Transverse Dam-break Waves on a Flat Bed in Steady State

Figure 3-5 shows the flow patterns of the TDWs on a flat bed in the steady state. The patterns delineated by the local Froude number  $Fr = \sqrt{u^2 + v^2} / \sqrt{gh}$  on the  $x$ - $y$  plane, are obtained at a time  $t = 10 t_s$ . The flow is considered to have reached the steady state as the total outflow rate  $Q$  has nearly reached its asymptote at this time, as shown in figure 3-4. There are two distinctively different steady-state flow patterns. Figures 3-5(a), (b) and (c) are the patterns for subcritical main flow with  $Fr_o = 0.03, 0.48,$  and  $0.80$ , and Figures 3-5(d), (e) and (f) for supercritical main flow with  $Fr_o = 1.00, 1.28$  and  $1.92$  respectively. For subcritical main flow with  $Fr_o < 1$ , a supercritical expansion on the upstream side is followed by subcritical outflow. Rapid change in depth and velocity occurs across the hydraulic jump as the flow changes from supercritical to subcritical flow. The length  $L_{\text{super}}$  defines the location of the hydraulic jump at the gate, as shown in figure 3-1. Figure 3-6 shows the fraction of supercritical outflow,  $L_{\text{super}}/L$ . The supercritical fraction of the flow increases in length linearly with the main-flow Froude number  $Fr_o$  in the range varying from  $Fr_o = 0$  to 1. The entire outflow becomes supercritical when  $Fr_o \geq 1$ .

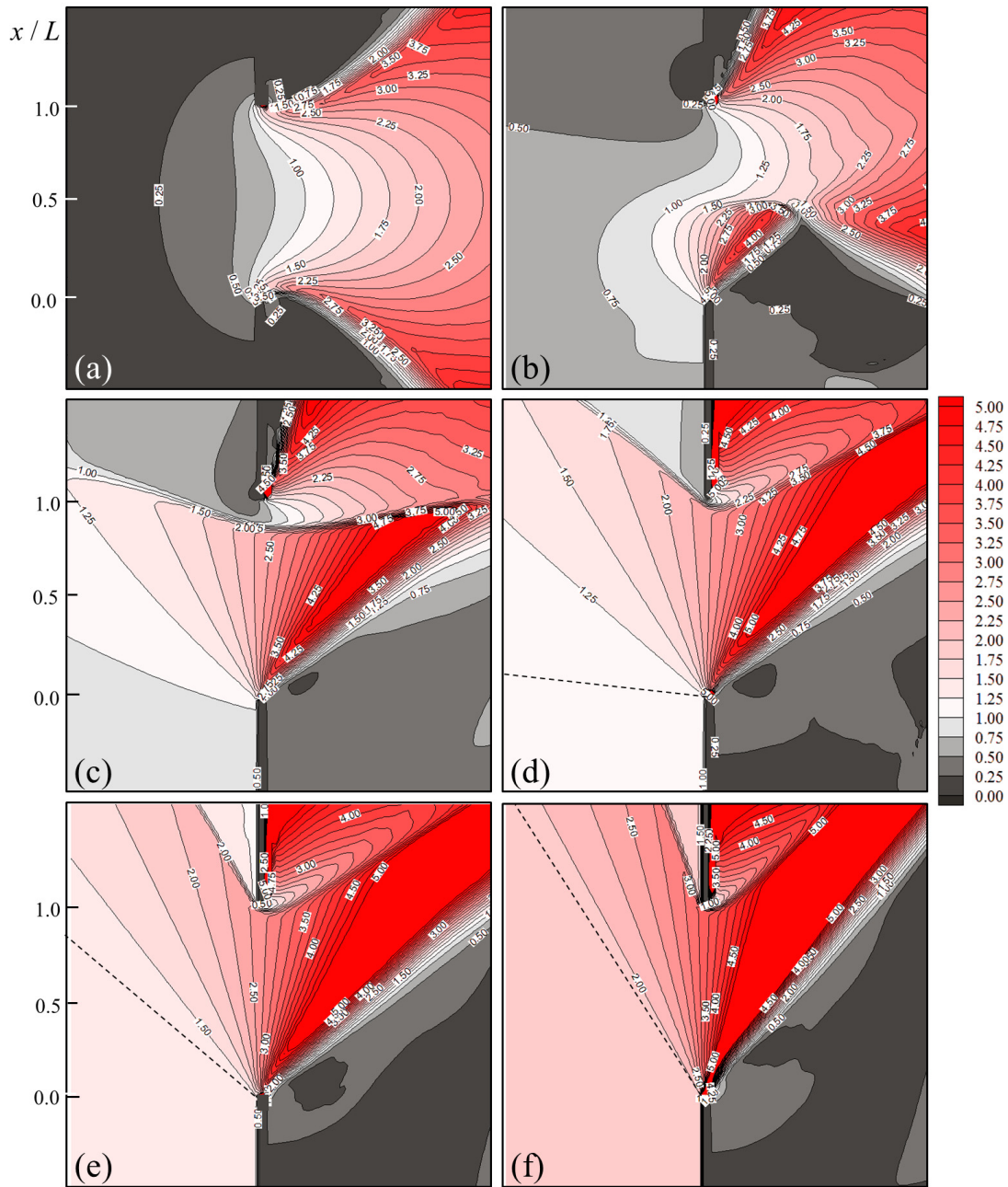


Figure 3-5: The TDWs on a flat bed at the steady state when time  $t = 10t_s$ . The main-flow Froude numbers are (a)  $Fr_o = 0.03$ , (b)  $Fr_o = 0.48$ , (c)  $Fr_o = 0.80$ , (d)  $Fr_o = 1.00$ , (e)  $Fr_o = 1.28$  and (f)  $Fr_o = 1.92$ . The contour values are the local Froude numbers. Dashed lines in (d), (e) and (f) indicate the “Froude line” between the undisturbed main flow and the diversion expansion fan.

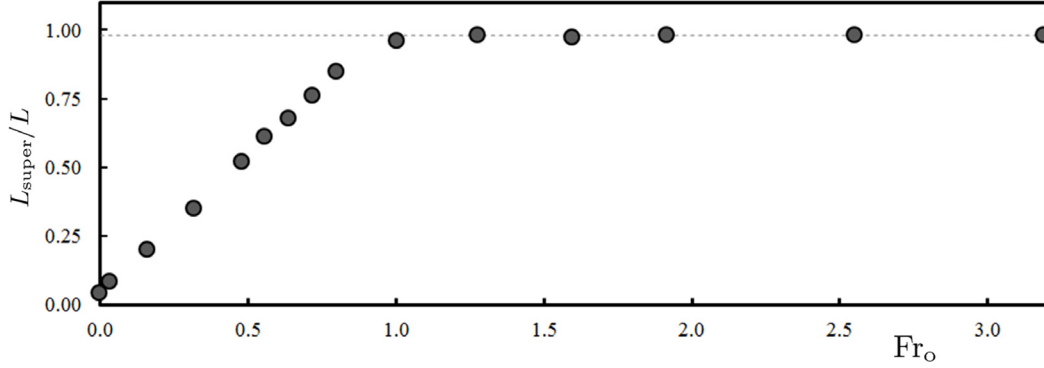


Figure 3-6: The length fraction  $L_{\text{super}}/L$  of the supercritical flow expansion.

### 3.5.1 Prandtl-Meyer Expansion for TDWs with $\text{Fr}_o > 1$

In the steady state, the diversion of the supercritical outflow on a flat bed is the Prandtl-Meyer expansion. Mizumura *et al.* (2003) provided the following explicit expressions for the velocity components ( $v_r, v_\theta$ ) and the depth  $h$  of the Prandtl-Meyer expansion in plane polar coordinates ( $r, \theta$ ):

$$v_r = \sqrt{2gE} \sin\left(\frac{\theta + \theta_1}{\sqrt{3}}\right), v_\theta = \sqrt{\frac{2gE}{3}} \cos\left(\frac{\theta + \theta_1}{\sqrt{3}}\right), h = \frac{2E}{3} \cos^2\left(\frac{\theta + \theta_1}{\sqrt{3}}\right) \quad (3.9)$$

The angle  $\theta$  is clockwise from the opening where  $y = 0$ . These solutions give  $\text{Fr}_\theta = v_\theta/\sqrt{gh} = 1$  throughout the expansion fan and a critical outflow of  $\text{Fr}_y = v/\sqrt{gh} = 1$  at the opening where  $y = 0$ . The corresponding flow rate in the  $y$ -direction is

$$q_y = [v_r \sin \theta + v_\theta \cos \theta] h. \quad (3.10)$$

The specific energy  $E$  and the angle  $\theta_1$  in Equations (3.9) are

$$E = H_o \left[ \frac{1}{2} \text{Fr}_o^2 + 1 \right], \quad \theta_1 = \sqrt{3} \cos^{-1} \sqrt{\frac{3}{2 + \text{Fr}_o^2}} + \sin^{-1} \frac{1}{\text{Fr}_o} \quad (3.11)$$

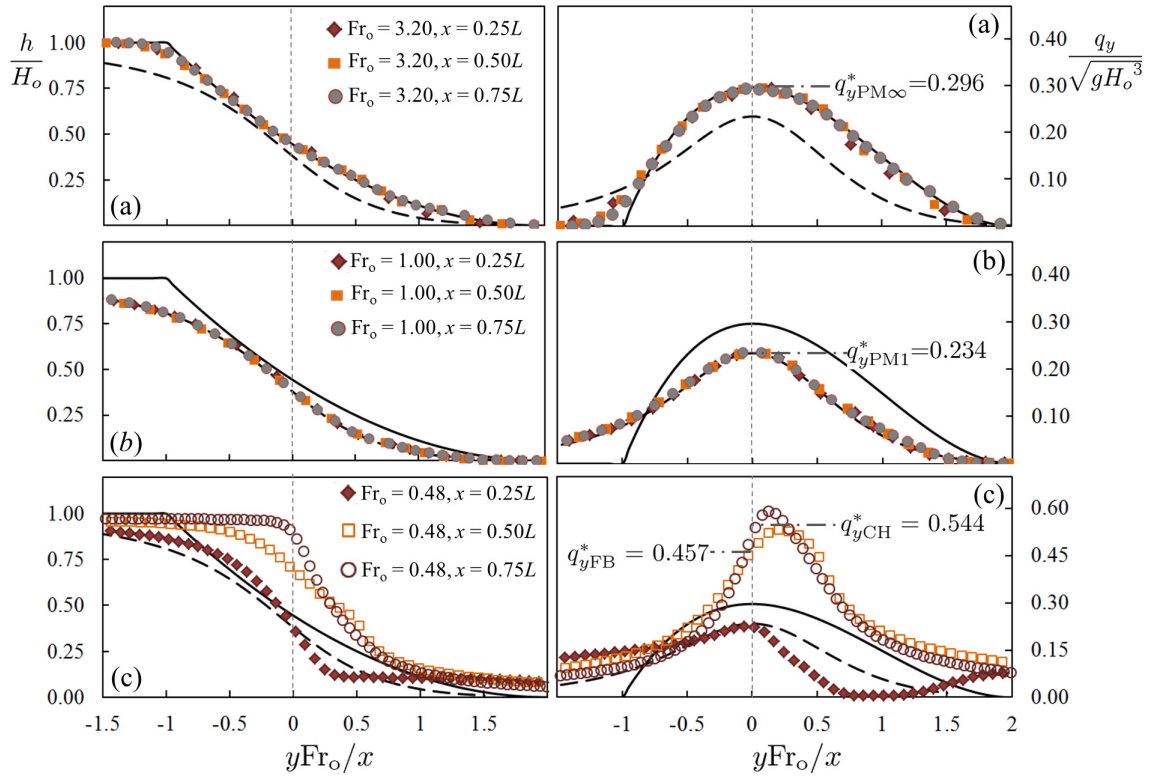


Figure 3-7: Depth  $h$ -profile (left) and lateral discharge  $q_y$ -profile (right) of the TDWs in the steady state for (a)  $Fr_o = 3.2$ , (b)  $Fr_o = 1.0$  and (c)  $Fr_o = 0.48$ . The dashed lines and the solid lines are the Prandtl-Meyer profiles for the limiting cases of  $Fr_o = 1$  and  $Fr_o \rightarrow \infty$ , respectively.

which are evaluated at the “Froude line” between the expansion fan and the undisturbed main flow where  $\theta = -\sin^{-1}[1/\text{Fr}_o]$ . At the Froude line,  $h = H_o$  and  $\sqrt{v_r^2 + v_\theta^2} = U_o$ .

### 3.5.2 Prandtl-Meyer Expansion in Terms of Ritter’s Similarity Variable

For observation in a reference frame moving with the undisturbed main flow, the space and time are related through the Galilian transformation  $x = U_o t$ . With this transformation,  $t\sqrt{gH_o} = x/\text{Fr}_o$ , the Ritter’s similarity variable becomes  $R = y\text{Fr}_o/x$ . The  $h$ -profile and the  $q_y$ -profile of the Prandtl-Meyer expansion given by Equations (3.9) and (3.10) are unique functions of Ritter’s similarity variable. The dashed lines and the solid lines in Figure 3–7 are respectively the limiting profiles when  $\text{Fr}_o = 1$  and  $\text{Fr}_o \rightarrow \infty$ . The points in the figure denote the numerical simulation results at three outflow sections  $x = 0.25L, 0.5L$  and  $0.75L$ . For the main-flow Froude number  $\text{Fr}_o = 3.2$  and  $1.0$ , the points in Figure 3–7(a) and (b) respectively fall between the solid line and dashed line, supporting the use of Ritter’s similarity variable to describe the Prandtl-Meyer expansion. Exactly like the 1D solution of Ritter’s, the outflow rate peaks at a critical-flow section where the local Froude number  $Fr_y = (q_y)_{\max}/\sqrt{gh^3} = 1$ . The lateral flow through the gate opening is the exact value of Ritter’s  $q_{y\text{PM}\infty}^* = q_{\text{Ritter}}^* = (q_y)_{\max}/\sqrt{gH_o^3} = 0.296$  as the main-flow Froude number  $\text{Fr}_o \rightarrow \infty$ . The rate drops to a value of  $q_{y\text{PM}1}^* = 0.234$  as the main-flow Froude number approaches its lowest value of  $\text{Fr}_o = 1$ . The drop in the flow rate from  $q_{y\text{PM}\infty}^*$  to  $q_{y\text{PM}1}^*$  is most likely due to the retreating wave-front velocity at the Froude line. Greater retreating velocity leads to lower critical flow rate. In the

reference frame moving with the main flow, the retreating velocity is  $v \rightarrow -\infty$  at the Froude line if the main-flow Froude number is  $Fr_o = 1$ . The retreating velocity is reduced to the value of Ritter's  $v = -\sqrt{gH_o}$  as the main-flow Froude number  $Fr_o \rightarrow \infty$ .

### 3.5.3 Transverse Dam-break Waves for Subcritical Main Flow

Figure 3–7(c) shows the simulation profiles for the subcritical main flow of  $Fr_o = 0.48$ . The solid symbols in the figures delineate the depth and discharge profiles in the expansion fan upstream of the jump. They are comparable to the profiles of the Prandtl-Meyer for  $Fr_o = 1$  defined by the dashed lines, with a peak discharge of  $q_y^* \simeq q_{yPM1}^* = 0.234$ . However, the profiles defined by the open symbols for the pool of water downstream of the hydraulic jump are very different. The peak discharge in the pool is significantly higher. The flow downstream of the hydraulic jump (where  $q_x \ll q_y$ ) is nearly unaffected by the main flow. Therefore the outflow from the pool can be roughly characterized by the head  $H_o$ , leading to a peak discharge of  $q_y = \sqrt{g(2H_o/3)^3}$  and a peak discharge coefficient of  $q_{yCH}^* = \sqrt{(2/3)^3} = 0.544$ . The peak occurs at the critical depth  $h_c = 2H_o/3$  where the Froude number  $v/\sqrt{gH_o} = 1$ . The depth at the opening downstream of the hydraulic jump is slightly greater than the critical depth therefore the discharge coefficient  $q_{yFB}^* \simeq 0.457$  at the opening is lower than the peak values.

## 3.6 Discharge Coefficient over Weir and Flat Bed

The simulation results thus far have been presented for the TDWs on a flat bed. A number of additional simulations have been carried out for the outflow

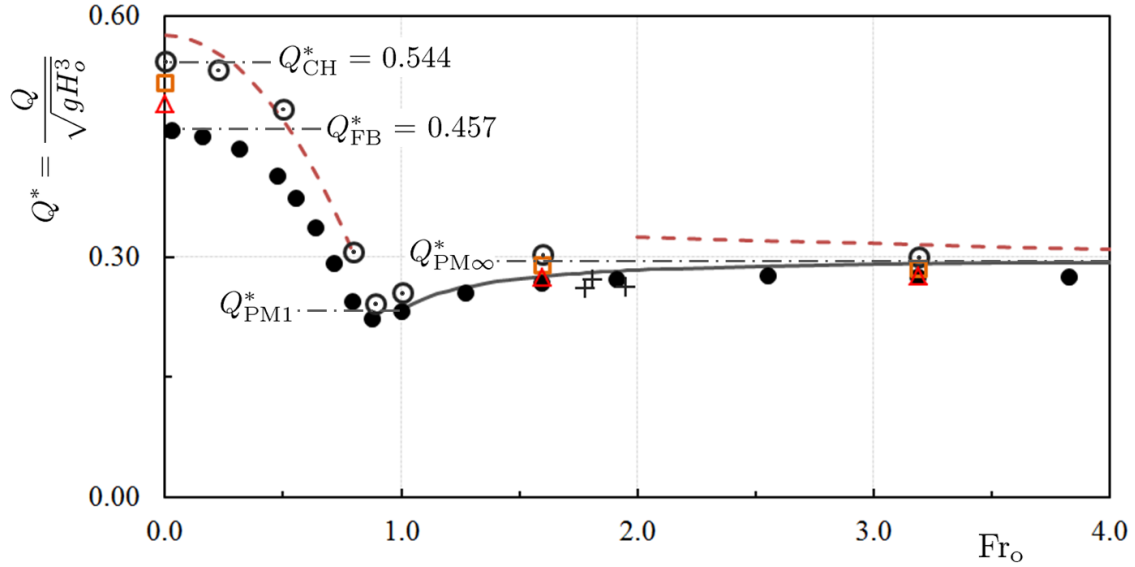


Figure 3–8: Dependence of steady-state discharge coefficient on the main-flow Froude number. The solid symbols denote the discharge coefficient obtained from the simulations over a flat bed. The open symbols denote the simulated outflow over weirs of  $W_w/H_w = 16, 8$  and  $4$ , respectively. The solid line is the Prandtl-Meyer solution for the expansion. The + symbol represents the laboratory data obtained by Mizumura *et al.* (2003). The red dashed lines are the empirical Equations (3.12) and (3.13) derived from laboratory experiments over a sharp-crested weir by Subramanya & Awasthy (1972).

over weirs. The results are compared with laboratory experimental observations. Some of laboratory experiments were conducted for outflow on flat bed. Most of the experiments were over sharp-crested weirs. Figure 3–8 shows all simulation results on flat bed and over the weir, and available experimental data for the total discharge coefficient  $Q^* = [\int_0^L q_y dx] / L \sqrt{gH_o^3}$ .

### 3.6.1 Discharge Coefficient for Diversion over Weir

For the simulation over the weir, the bottom elevation is  $z_o = \frac{1}{2}H_w[\cos(\pi y/W_w) + 1]$  gradually varying over the width of the weir from  $y = -\frac{1}{2}W_w$  to  $y = \frac{1}{2}W_w$ . With the weir, the depth  $H$  in the main flow is not uniform. However, the main-flow Froude number  $Fr_o = U/\sqrt{gH}$  is unchanged by varying the velocity  $U$  across the main flow. The width-to-height ratio of the weir,  $W_w/H_w$ , is a parameter of the weir that affects the diversion flow rate, which increases with the steepness of the weir. For the main flow Froude Number of  $Fr_o = 0$ , the increases from the flat bed value are 7%, 13%, and 19% for the ratio of  $W_w/H_w = 16, 8, \text{ and } 4$ , respectively. For  $Fr_o = 1.6$  the increases are 3%, 8%, 14% and for  $Fr_o = 3.2$  the increases are 0.3%, 4%, 8.9%, respectively. The gradual rise in bottom elevation has only a small effect on the discharge coefficient. However, a more rapid rise in bottom elevation for the sharper crested weir of  $W_w/H_w = 4$  increases the discharge coefficient to  $Q_{\text{weir}}^* = 0.545, 0.307, 0.255, 0.304, 0.301$  for  $Fr_o = 0, 0.8, 1.00, 1.6, 3.2$ , respectively. These coefficients are marked by the  $\odot$  symbol in Figure 3–8.

For subcritical main flow ( $Fr_o < 1$ ), the presence of the weir has the effect of bringing the critical-flow section closer to the crest of the weir. The result is increase in the discharge coefficient. For zero main flow the increase is from  $Q_{\text{FB}}^* = q_{y\text{FB}}^* = 0.457$  to a value of  $Q_{\text{CH}}^* = q_{y\text{CH}}^* = 0.544$  as shown in figure 3–8. The derivation for the value of  $q_{y\text{CH}}^*$  has been previously given in section 3.5.3. Increasing the main flow Froude number  $Fr_o$  from 0 to 1 progressively increases the presence of the supercritical flow expansion and reduces the contribution of the subcritical outflow downstream

of the hydraulic jump. The consequence is the reduction of the discharge coefficient in the subcritical range of main-flow Froude number as shown in Figure 3–8.

The effect of the weir on the outflow in the supercritical range of main-flow Froude number ( $Fr_o > 1$ ) is different. All outflows from the Prandtl-Meyer expansion are critical with  $Fr_y = v/\sqrt{gh} = 1$  at the gate opening (see section 3.5.1). The presence of the weir does not change the location of the critical section. It does however produce a narrower expansion fan, and hence the tendency for supercritical main-flow to increase the discharge coefficient toward the rate of Ritter's  $Q_{PM\infty}^* = q_{yPM\infty}^* = 0.296$ .

### 3.6.2 Laboratory Experimental Investigation

Mizumura *et al.* (2003) have measured the diversion flow rate in laboratory experiments over a flat bed. Their data are affected by the bed friction but are only slightly below the discharge coefficient obtained from the simulations. Subramanya & Awasthy (1972) have conducted laboratory experiments to measure the diversion flow rate over a sharp-crested weir and on a flat bed. They introduced the discharge coefficient  $C_d$  via  $Q = \frac{2}{3}C_d\sqrt{2gH_o^3}$ , and proposed the following semi-empirical formulae to fit their data:

$$C_d = 0.611\sqrt{1 - \left(\frac{3Fr_o^2}{Fr_o^2 + 2}\right)} \quad \text{for } Fr_o < 0.8 \quad (3.12)$$

$$C_d = 0.36 - 0.008 Fr_o \quad \text{for } Fr_o > 2 \quad (3.13)$$

The dashed lines in Figure 3–8 are these formulae evaluated for  $Q^* = \frac{2}{3}\sqrt{2}C_d$ . The ratios of the main-flow width to side-weir length varying from  $B/L = 5$  to 1 in the

laboratory experiments of Subramanya & Awasthy (1972) are not the same as the width-to-length ratios in the simulations. The trend of the numerical simulation results nevertheless is consistent with the experimental data.

### 3.7 Conclusion

The diversion of water to the side of main flow produces a family of TDWs that is dependent on the Froude number of the main flow. For subcritical main flow ( $Fr_o < 1$ ), the TDWs are supercritical flow expansions followed by a hydraulic jump to subcritical outflows. For supercritical main flow ( $Fr_o > 1$ ), the TDWs are expansions that approach rapidly to the steady-state solution of Prandtl-Meyer. The simulations of flow over weirs have produced discharge coefficients that follow the trend of dependence on the main-flow Froude number in a manner that is consistent with the data obtained from laboratory observation. The agreement of the simulations with analytical solutions is validation of the present numerical method, showing that it can be relied on to find solutions to other related flow-diversion problems, including the problems studied by Vazquez *et al.* (2008), Ghostine *et al.* (2013) and others. The method can also be utilized to study the erosion of channels and deposition of sediments in situations where the bottom of the channel varies in space, and in time.

## CHAPTER 4 LINEAR INSTABILITIES IN SHALLOW FLOW

S. Karimpour Ghannadi and V. H. Chu. Linear Instabilities in Shallow Flow. *Journal of Fluid Mechanics*, Draft for submission, 2014.

### 4.1 Abstract

Numerical simulations of the shallow-flow instabilities are conducted using an accurate numerical scheme to find solution directly from the shallow-water equations. The radiation intensity from the subcritical instabilities increases with the convective Froude number and reaches its maximum at a convective Froude number of about 0.7. In the supercritical flow, the waves produced by the instabilities are trapped between the returning surfaces where the relative current speed matches the gravity-wave speed. The excitation, reflection and transmission of the supercritical instabilities between the returning surfaces produce modulating waves that maintain a consistent linear structure as the amplitude of the structure increases greatly over many orders of its magnitude before reaching the finite amplitude in the nonlinear stage.

**Keywords:** Shear Instabilities, Shallow Flow, Waves in Currents, Numerical Simulations

## 4.2 Introduction

The instabilities of shear flow in shallow waters involve both the vorticity and gravity waves. The classical instability analysis is based on the assumption of the normal mode. The solutions for the depth and velocity fluctuations of the disturbances  $[h', u', v']$  take the form of  $[\hat{h}(y), \hat{u}(y), \hat{v}(y)] \exp ik_x(x - c_t t)$ . In this normal-mode approach,  $c_t$  is determined as an eigenvalue problem. The fractional growth rate (or exponential growth rate) of the disturbance is the imaginary part of  $c_t$ :

$$\Im(c_t) = \frac{1}{h'} \frac{dh'}{dt} = \frac{1}{u'} \frac{du'}{dt} = \frac{1}{v'} \frac{dv'}{dt}. \quad (4.1)$$

The phase velocity is the real part  $\Re(c_t)$ . Implicit in the normal-mode approach is the requirement of a time independent relation between the real and imaginary parts of  $c_t$  and the wave number  $k_x$ . A less restrictive method of the stability analysis is direct numerical simulation (DNS). The fractional growth rate of the instabilities as defined by Equation (4.1) is determined directly from the numerical solutions of the full equations. Using the fifth-order WENO for spatial interpolation, and the fourth-order Runge-Kutta for time integration, Karimpour & Chu (2014) have been able to find the fractional growth rate of the subcritical instabilities from DNS using the shallow-water equations without assuming the existence of the normal mode. The same numerical codes are employed in this paper to provide further details of the instabilities. This includes the extension of the calculations to supercritical instabilities when entrainment and radiation of the gravity waves are significant factors in the process. We consider the base flow with the hyperbolic tangent velocity problem in a domain of infinite lateral extend as shown in Figure 4–1. Gravity waves produced as

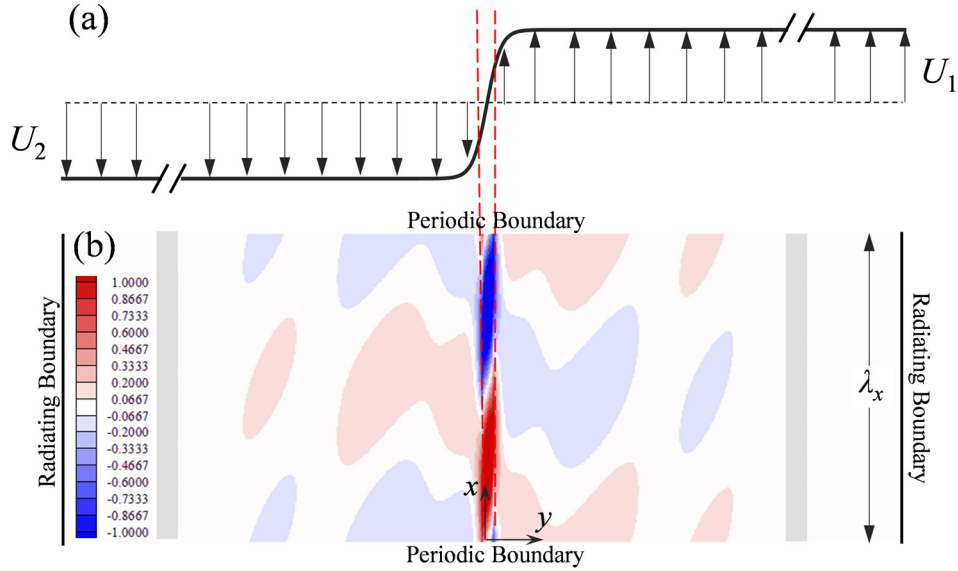


Figure 4-1: (a) TANH base-flow velocity profile. (b) Computational domain defined in the  $x$ -direction from  $x = 0$  to  $\lambda_x$  and in the lateral  $y$ -direction from  $y = y^-$  to  $y = y^+$ . The dashed lines mark the returning surfaces where the current speed matches the gravity-wave speed.

part of shear instabilities are allowed to escape from the computational domain. The general problem of the instabilities in shallow waters has been examined using the normal mode approach by Balmforth (1999). The analogous problem in gas dynamics was examined by Blumen *et al.* (1975), Sandham & Reynolds (1990) and Mack (1990). Wave entrapment and radiation are significant in the instabilities in shallow waters. The DNS is to provide the details of the entrapment and radiation processes in the instabilities that are the extension beyond the existing results obtained from the classical method of the normal mode.

### 4.3 Direct Numerical Simulation

The shallow-water equations for the direct numerical solutions for depth  $h$  and velocities  $u$  and  $v$  are:

$$\frac{\partial h}{\partial t} + \frac{\partial uh}{\partial x} + \frac{\partial hv}{\partial y} = 0 \quad (4.2)$$

$$\frac{\partial u}{\partial t} + u \frac{\partial u}{\partial x} + v \frac{\partial u}{\partial y} = -g \frac{\partial h}{\partial x} \quad (4.3)$$

$$\frac{\partial v}{\partial t} + u \frac{\partial v}{\partial x} + v \frac{\partial v}{\partial y} = -g \frac{\partial h}{\partial y} \quad (4.4)$$

where  $g$  is the gravity. The base flow is the hyperbolic-tangent (TANH) velocity profile

$$U = \frac{1}{2}(U_1 + U_2) + \frac{1}{2}(U_1 - U_2) \tanh \frac{2y}{\delta_{\omega o}} \quad (4.5)$$

The velocities in the free streams are  $U_1$  on one side and  $U_2$  on the other side of the shear flow. Simulation for the instabilities starts with the superposition of a small disturbance  $(h', u', v')$  to the base flow  $(H, U, 0)$ . The subsequent development of the disturbance is determined directly from the numerical solution of the shallow-water equations to find  $h = H + h'$ ,  $u = U + u'$ ,  $v = v'$ . To study the linear instabilities, the calculation is started with a disturbance of very small amplitude so that the nonlinear terms remain negligible after the amplitude of the disturbance has increased significantly by many orders of magnitude. In the present simulations, the initial disturbance is the depth fluctuations  $h'/\delta_{\omega o} = 10^{-10} \sin(2\pi/\lambda_x)$  specified in the central area from  $y = -\lambda_x/64$  to  $y = +\lambda_x/64$ ; the depth elsewhere is  $h' = 0$ . Figure 4-1 (a) shows the TANH base velocity profile and Figure 4-1 (b) the computational domain defined by the periodic boundary condition over one wave length in the longitudinal direction from  $x = 0$  to  $x = \lambda_x$  and the radiation boundary condition

at  $y = y^-$  and  $y = y^+$ . The velocity difference  $(U_1 - U_2)$  is the velocity scale of the instability problem. The length scale is the vorticity thickness  $\delta_{\omega o}$  defined by the shear rate at the inflection point  $\hat{U}_y = (U_1 - U_2)/\delta_{\omega o}$ . The characteristics of instabilities depend on the wave number of the disturbance  $k_x = 2\pi/\lambda_x$ , and the convective Froude number  $Fr_c$  which is the ratio of the velocity difference  $(U_1 - U_2)$  and wave speed of the gravity wave  $\sqrt{gH}$  as follows:

$$Fr_c = \frac{U_1 - U_2}{2\sqrt{gH}} \quad (4.6)$$

The lateral dimensions of the computational domain  $(y^+ - y^-)$  is selected to vary from  $4 \lambda_x$  and  $10 \lambda_x$  depending on the convective Froude number. The calculations for the subcritical instability were made in a computational domain with a lateral dimension from  $y = y^- = -5\lambda_x$  and  $y = y^+ = 5\lambda_x$ . The calculations for the supercritical instability one the other hand were made in a domain with lateral dimensions from  $y = y^- = -2\lambda_x$  and  $y = y^+ = 2\lambda_x$ .

In an unstable shear flow, all components of the disturbance  $h'$ ,  $u'$  and  $v'$  grow exponentially. These include the disturbance vorticity  $\zeta' = (\partial v'/\partial x - \partial u'/\partial y)$ , the disturbance kinetic energy  $K' = \frac{1}{2}(u'^2 + v'^2)$  and disturbance potential energy  $P' = \frac{1}{2}gh'^2$ . The averages of  $K'$  and  $P'$  are obtained by the integration over the computational domain as follows:

$$\overline{K'} = \frac{1}{\lambda_x} \int_o^{\lambda_x} \left[ \frac{1}{\delta_{\omega o}} \int_{y^-}^{y^+} K' dy \right] dx, \quad \overline{P'} = \frac{1}{\lambda_x} \int_o^{\lambda_x} \left[ \frac{1}{\delta_{\omega o}} \int_{y^-}^{y^+} P' dy \right] dx \quad (4.7)$$

Figure 4-2 shows the variation of the characteristic velocity  $\sqrt{\overline{K'}}/(U_1 - U_2)$  with time  $t\hat{U}_y$  in a semi-logarithmic scale. Figure 4-3 shows the ratio of the potential to

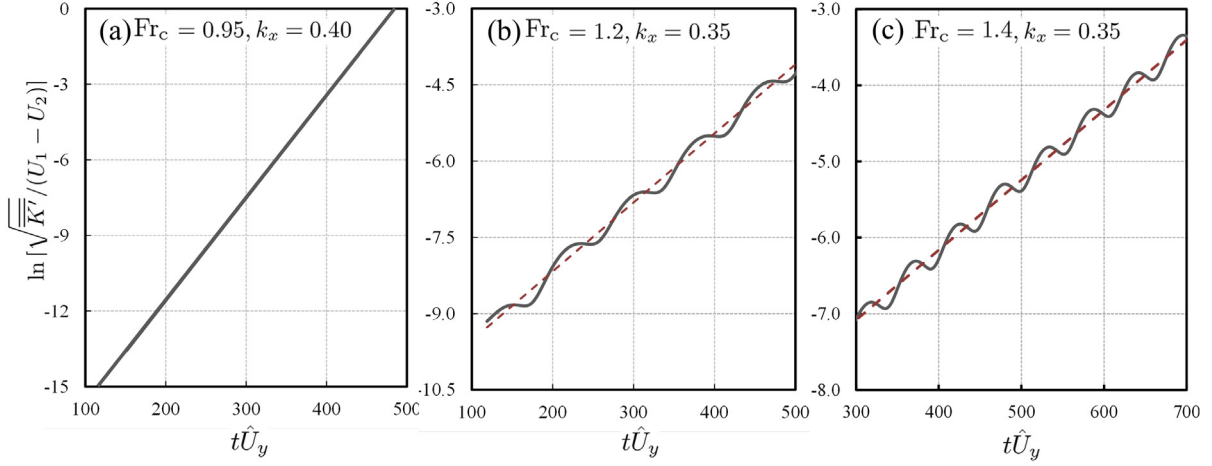


Figure 4-2: The growth of the perturbations' kinetic energy,  $\overline{\overline{K^i}}/(U_1 - U_2)$ , with time  $t\hat{U}_y$  on the semi-logarithmic scale for (a) subcritical instabilities with  $\text{Fr}_c = 0.95$ ,  $k_x = 2\pi/\lambda_x = 0.40$  (b) supercritical instabilities with  $\text{Fr}_c = 1.2$ ,  $k_x = 0.35$  and (c) supercritical instabilities with  $\text{Fr}_c = 1.4$ ,  $k_x = 0.35$ . The fractional growth rates are respectively  $\alpha/\hat{U}_y = 0.0407$  and  $\bar{\alpha}/\hat{U}_y = 0.01365, 0.0094$ .

kinetic energy  $\overline{\overline{P^i}}/H\overline{\overline{K^i}}$ . The ratio defines the overall structure of instabilities and is maintained as the amplitude of disturbance has increased by many orders of magnitude. There are however significant differences in the structure of the instabilities between the subcritical base flow with  $\text{Fr}_c \leq 1$  and supercritical flow with  $\text{Fr}_c > 1$ . The subcritical instabilities have an absolutely constant structure. The supercritical instabilities on the other hand are modulating with a modulating period  $T$  that has a corresponding frequency  $\omega_M = 2\pi/T$ . Despite the modulation, a *consistent structure* is nevertheless observed to maintain during the entire development of the supercritical instabilities.

Table 4-1 provides the overall characteristics for the three typical instabilities shown in Figure 4-2 (a), (b) and (c) and Figure 4-3 (a), (b) and (c), with the

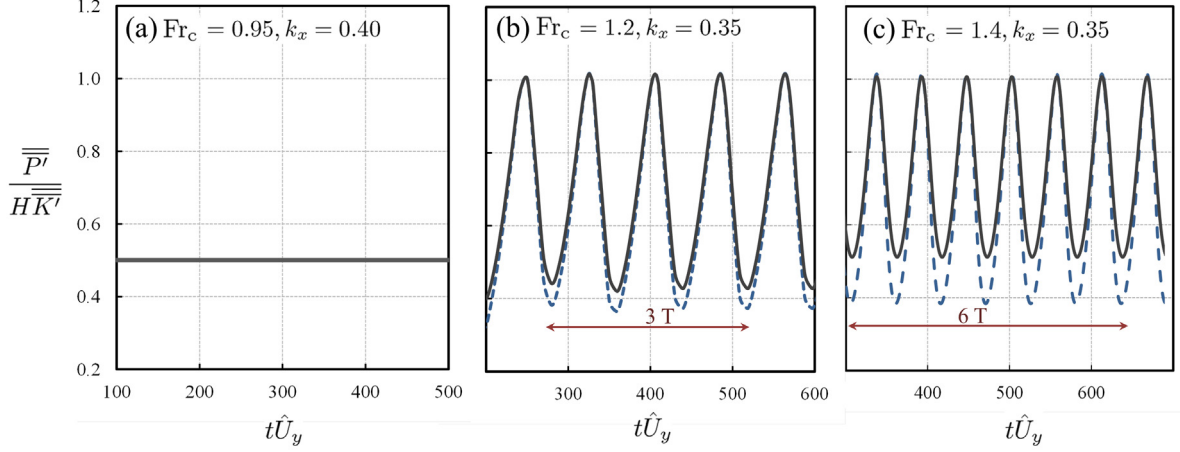


Figure 4-3: Disturbance potential energy to kinetic energy ratio ( $\overline{\overline{P'}}/H\overline{\overline{K'}}$ ) for (a)  $Fr_c = 0.95, k_x = 2\pi/\lambda_x = 0.40$ , (b)  $Fr_c = 1.2, k_x = 0.35$  and (c)  $Fr_c = 1.4, k_x = 0.35$ . The dashed and solid lines in (b) and (c) represent the results obtained from two computational domain sizes of  $y^+ = -y^- = \lambda_x$  and  $y^+ = -y^- = 2\lambda_x$ , respectively.

Table 4-1: The level of normal disturbance kinetic energy growth. The initial disturbance perturbs depth at a magnitude of  $h'/\delta_{\omega_0} = 1E-10$ . For the supercritical  $Fr_c = 1.4$ , it takes about  $t\hat{U}_y = 250$  to reach the linear consistent structure.

$Fr_c$	$k_x$	$\sqrt{\overline{\overline{K'}}_b}/(U_1 - U_2)$	$t_b\hat{U}_y$	$\sqrt{\overline{\overline{K'}}_e}/(U_1 - U_2)$	$t_e\hat{U}_y$	$\overline{\alpha}/\hat{U}_y$	$T\hat{U}_y$
(a) $Fr_c = 0.95$	0.40	2E-9	20	0.36	500	0.0407	–
(b) $Fr_c = 1.20$	0.35	2E-9	90	0.23	1450	0.013	79
(c) $Fr_c = 1.40$	0.35	2E-9	250	0.313	2250	0.0094	55

convective Froude numbers of  $\text{Fr}_c = 0.95, 1.2$  and  $1.4$ , respectively. The consistent structure of the instabilities begins at time  $t_b$  and ends at time  $t_e$ . For the cases (a), (b) and (c) shown in the table, the formation of the consistent structure begins from the time  $t_b \hat{U}_y \simeq 20, 90$  and  $250$  and is maintained until the end time of  $t_e \hat{U}_y \simeq 500, 1450$  and  $2250$ , respectively. Over this linear stage of the disturbance's development from  $t_b \hat{U}_y$  to  $t_e \hat{U}_y$ , the amplitudes of the disturbance are magnified by many millions of times. However, the magnitude of the disturbance remains small and the nonlinear terms remain negligible over the same period of time.

#### 4.4 Fractional Growth Rate

During the linear stage of the instabilities' development, the fractional growth rates for all components  $h', u'$  and  $v'$  are the same, including the rate for the kinetic energy,  $K' = \frac{1}{2}(u'^2 + v'^2)$ . In the present simulations, the characteristic velocity equal to the square root of the average kinetic energy determines the rate

$$\bar{\alpha} = \frac{1}{\sqrt{\overline{K'}}} \frac{d\sqrt{\overline{K'}}}{dt} = \frac{d \left[ \ln \sqrt{\overline{K'}} \right]}{dt} \quad (4.8)$$

This fractional growth rate is the slope of the lines  $\left[ \ln \sqrt{\overline{K'}} \right]$  versus time  $t$  in Figure 4-2 (a), (b) and (c), and is comparable to the eigenvalue  $\Im(c_t)$  as defined in Equation (4.1) for the normal mode. For the subcritical instabilities, the fractional growth rate  $\alpha$  is simply the slope of the straight line in the semi-logarithmic scale as show in Figure 4-2 (a) for  $\text{Fr}_c = 0.95$  and  $k_x = 0.4$ . For supercritical instabilities as show in Figure 4-3 (b) and (c), the fractional increase is not constant as the increase is modulating about the averaged value  $\bar{\alpha}$ . Despite the modulation, consistent linear

structure of the instabilities is maintained from  $t_b\hat{U}_y$  to  $t_e\hat{U}_y$  over a long period of time as the amplitude of the instabilities is magnified by million of times. The averaged fractional growth rate is relevant parameter of the instabilities as the same averaged rate  $\bar{\alpha}$  is maintained during the entire linear stage of the instabilities' development.

#### 4.5 Constant Structure of Subcritical Instabilities

The *constant structures* obtained by the DNS during the linear stage of its development are shown in Figure 4-4 for the convective Froude number of  $\text{Fr}_c = 0.7$  and the wave number of  $k_x = 0.6$ . The vorticity fluctuation profiles  $\zeta'\delta_{\omega o}/\sqrt{\overline{K'}}$  are plotted in the left-hand side of the figure for four longitudinal positions  $x = \frac{1}{4}\lambda_x$ ,  $x = \frac{1}{2}\lambda_x$ ,  $x = \frac{3}{4}\lambda_x$  and  $x = \lambda_x$ . On the right-hand side of these figures are the disturbance kinetic energy profiles  $\overline{K'}/\overline{K'}$  averaged over the wave length  $\lambda_x$  between the periodic boundary conditions:

$$\overline{K'} = \frac{1}{\lambda_x} \int_0^{\lambda_x} K' dx. \quad (4.9)$$

The profiles in Figure 4-4 and the profiles of all other variables for the subcritical instabilities with a convective Froude number  $\text{Fr}_c < 1$  are absolutely independent of time. The same profiles are maintained in the entire period as the disturbance is amplified by millions of times from the beginning of time  $t_b\hat{U}_y$  to the end time  $t_e\hat{U}_y$ . These time independent constant structures obtained from the DNS are identical to the normal-mode solution of the eigenvalue problem obtained by the classical method. Figure 4-5 shows the fractional growth rate obtained from DNS over a range of wave number for two convective Froude numbers  $\text{Fr}_c = 0.1$  and  $0.8$ . These are comparable with the analogous results obtained for ideal gas by Sandham & Reynolds (1990).

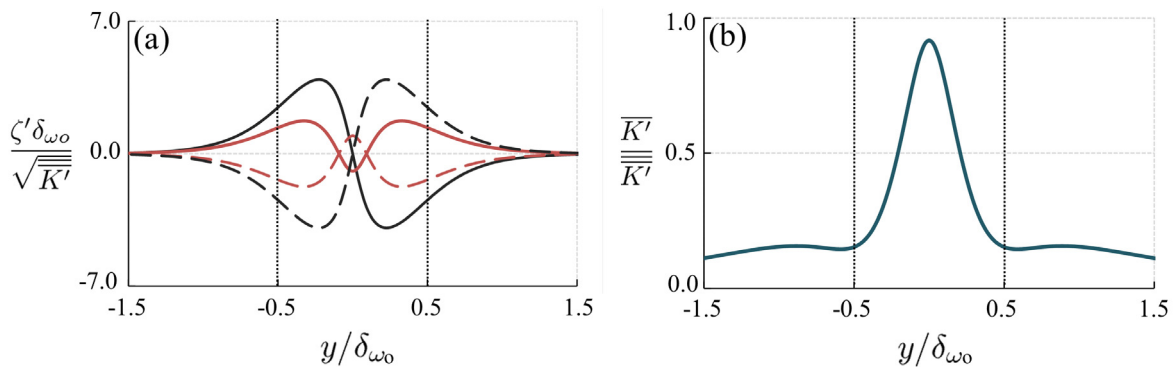


Figure 4-4: (a) vorticity fluctuation  $\zeta'\delta_{\omega_0}/\sqrt{\overline{K}'}$  and (b) disturbance kinetic energy  $\overline{K}'/\overline{K}'$  for the subcritical instability with  $\text{Fr}_c = 0.7$ ,  $k_x = 0.60$ .

The shallow-water equations are identical to the gas-dynamic equations when value of the specific heat ratio of the gas is 2 (Liggett 1994). The results obtained for  $\text{Fr}_c = 0.1$  also closely replicate the results obtained by Michalke (1964) for non-divergent flow in the limiting case of  $\text{Ma}_c = 0$ . Michalke (1964) and Sandham & Reynolds (1990) found the fractional growth using the classical method of the normal mode. The comparison therefore validates the DNS method as equivalent to the classical method. The DNS method however is more general as the method can find the instabilities in greater range of parameter space beyond the subcritical. The general application of the method will be further demonstrated in the subsequent sections.

#### 4.6 Consistent Structure for Supercritical Instabilities

The averaged fractional growth rate of the supercritical instabilities ( $\text{Fr}_c > 1$ ) is given in Figure 4-6. One example of the structure of the supercritical instabilities ( $\text{Fr}_c = 1.4$  and  $k_x = 0.35$ ) is shown in Figure 4-7. As shown in Figure 4-6, the

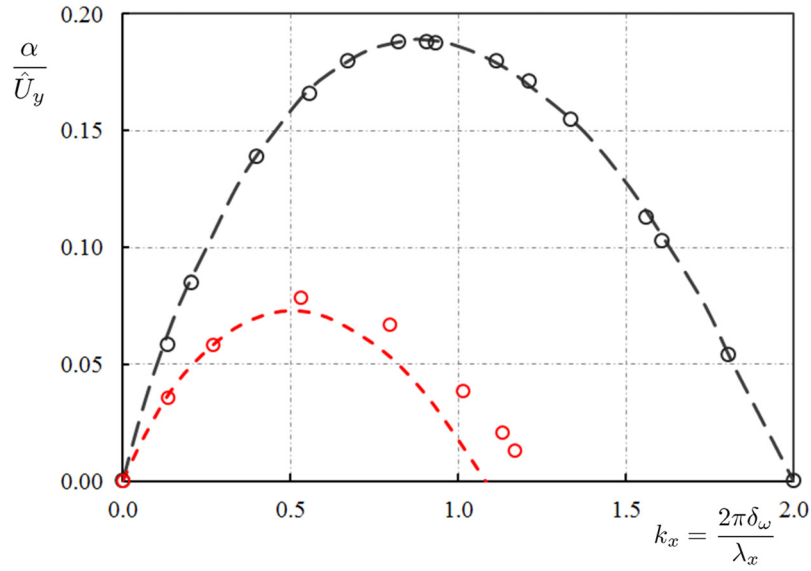


Figure 4-5: Fractional growth rate of the subcritical instability obtained from DNS for two convective Froude numbers  $Fr_c = 0.1$  and  $0.8$ . The dashed lines are the results obtained from for convective Mach number  $Ma_c = 0.01$  and  $0.8$  by Sandham and Reynolds (1990) for ideal gas.

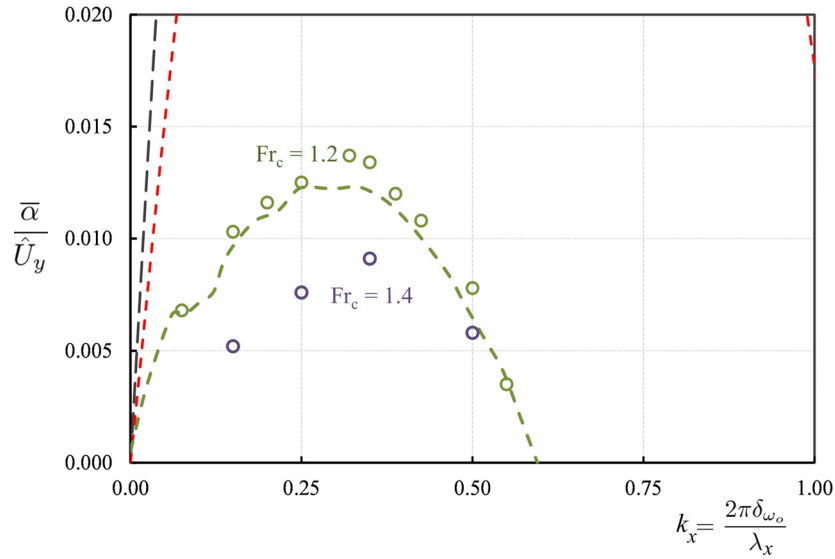


Figure 4-6: Averaged fractional growth rate  $\bar{\alpha}/\hat{U}_y$  of the supercritical instability for convective Froude numbers  $Fr_c = 1.2, 1.4$ . The dashed line is the relation for the ideal gas with the Mach number of  $Ma_c = 1.2$  obtained by Sandham and Reynolds (1990).

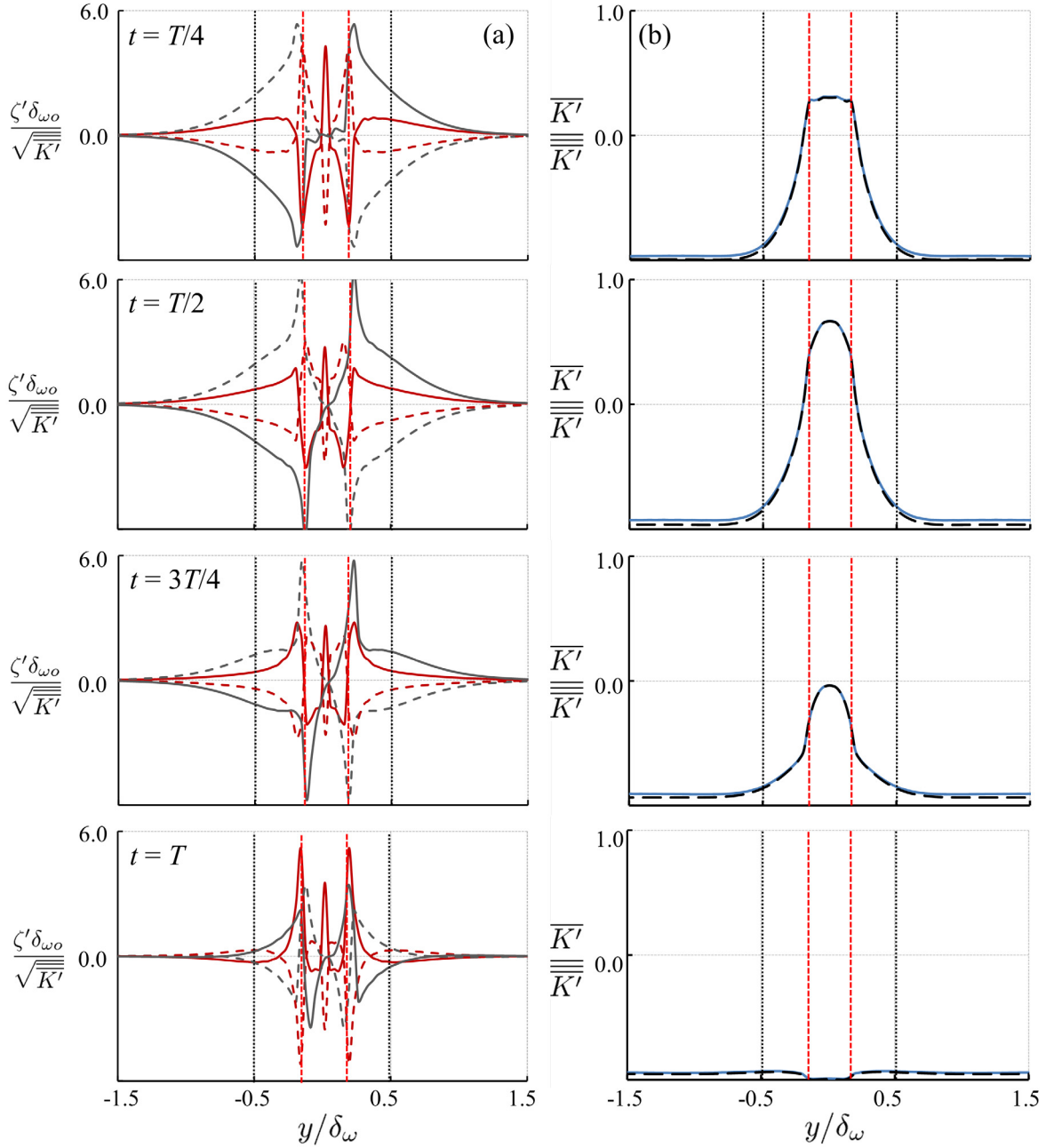


Figure 4-7: (a) Lateral vorticity fluctuation profiles,  $\zeta' \delta_{\omega o} / \sqrt{\overline{\overline{K'}}}$ , at  $x = \lambda_x/4$ ,  $\lambda_x/2$ ,  $3\lambda_x/4$  and  $\lambda_x$ ; and (b) lateral profile for the disturbance kinetic energy,  $\overline{K'}/\overline{\overline{K'}}$  (blue solid line) and normal reynold's stress  $\overline{u'u'}/2\overline{\overline{K'}}$  (dashed line), of the supercritical instability at  $Fr_c = 1.40$  and  $k_x = 0.35$  at  $\frac{1}{4}T$  (top),  $\frac{1}{2}T$  (top-centre) and  $\frac{3}{4}T$  (top-bottom) and  $T$  (bottom). The lateral extent of the shear instability over a distance of one vorticity thickness is marked by the black vertical dashed lines. The locations of the returning surfaces at  $y/\delta_{\omega o} = \pm 0.117$  is marked by the red vertical dashed lines.

averaged fractional growth rate  $\bar{\alpha}/\hat{U}_y$  for the supercritical instabilities is an order of magnitude smaller than the rate  $\alpha/\hat{U}_y$  for the subcritical instability in the same range of wave number. The peak rate of  $\bar{\alpha}/\hat{U}_y = 0.01365$  for  $\text{Fr}_c = 1.2$  at  $k_x = 0.35$  is comparable to the rate of 0.013 obtained by Sandham & Reynolds (1990). Sandham & Reynolds (1990) have conducted stability calculations for the ideal gas up to a Mach number of  $\text{Ma}_c = 1.2$ . Their results for  $\text{Ma}_c = 1.2$  are the dashed line in Figure 4-6. The DNS however has captured instabilities over a wider range of wave number beyond the range of reach by the classical method of the normal mode. The supercritical flow is susceptible to disturbance of smaller wave length beyond  $k_x = 1.0$ . The growth rate of the supercritical instabilities may be small. The instabilities however are real. For the case of  $\text{Fr}_c = 1.4$  and  $k_x = 0.35$  given in Table 4-1, the amplitude of the disturbance has increased from  $\sqrt{\overline{K'_b}}/(U_1 - U_2) = 2.0 \times 10^{-9}$  to  $\sqrt{\overline{K'_e}}/(U_1 - U_2) = 0.313$  before the reaching the nonlinear stage of its development. Such amplification in the linear stage is  $1.5 \times 10^8$  folds.

Over this enormous amplification of the disturbance, despite the modulation in growth rate, the instabilities maintain a *consistent structure*. An example of this consistent structure for the case of  $\text{Fr}_c = 1.4$  and  $k_x = 0.35$  is shown in Figure 4-7 over a period of  $T\hat{U}_y = 55$ . The profiles of the vorticity fluctuations  $\zeta'/\hat{U}_y$  and the averaged profiles of the kinetic energy  $\overline{K'}/\overline{K'}$  for time  $\frac{1}{4}T$ ,  $\frac{1}{2}T$ ,  $\frac{3}{4}T$  and  $T$  are similar but not identical as shown in Figures 4-7 (a) and (b), respectively. The most remarkable feature of these profiles is observed at the returning surface where the vorticity fluctuations peak. The kinetic energy of the waves that is trapped between the returning surfaces, modulates with time with a period  $T$  that depends on  $\text{Fr}_c$

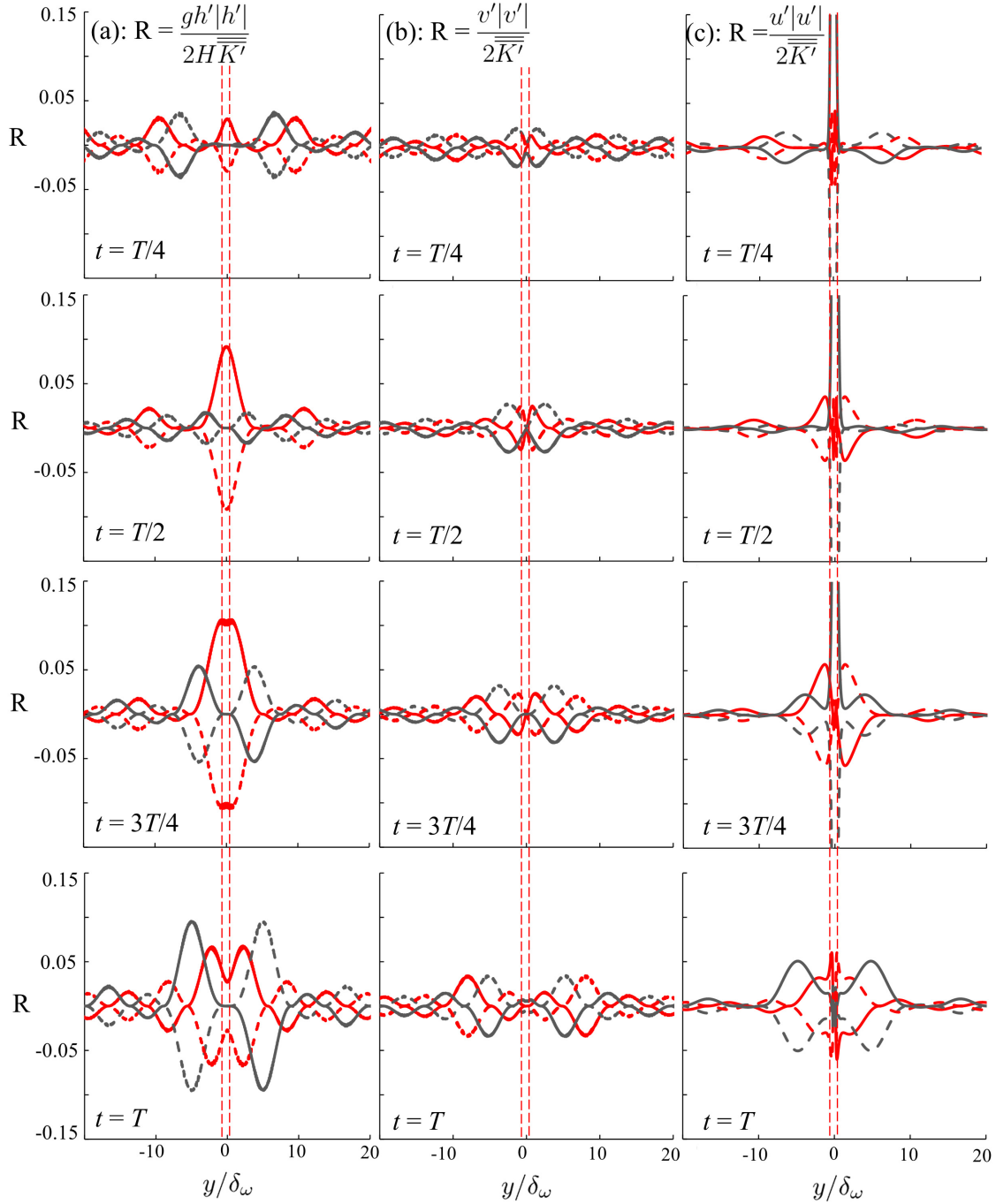


Figure 4–8: Lateral distribution of (a) disturbance potential energy  $gh'|h'|/(2H\overline{K'})$ ; (b) disturbance streamwise velocity  $u'|u'|/(2\overline{K'})$  and (c) disturbance lateral velocity  $v'|v'|/(2\overline{K'})$  for  $Fr_c = 1.4$  and  $k_x = 0.35$  over at  $\frac{1}{4}T$  (top),  $\frac{1}{2}T$  (top-centre) and  $\frac{3}{4}T$  (top-bottom) and  $T$  (bottom). Vertical dashed lines define the returning surfaces. The streamwise velocity fluctuation  $u'|u'|/(2\overline{K'})$  inbetween the returning surfaces reaches 1.30, 1.66, 0.96 and 0.06 at  $\frac{1}{4}T$ ,  $\frac{1}{2}T$ ,  $\frac{3}{4}T$  and  $\frac{3}{4}T$ , respectively.

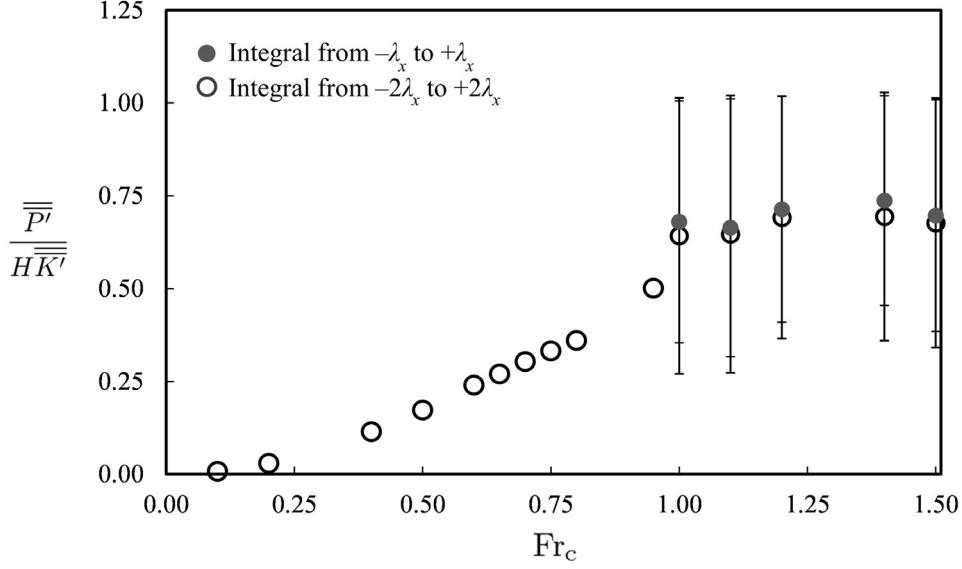


Figure 4-9: Ratio of averaged disturbance potential energy to averaged total disturbance kinetic energy ( $\overline{\overline{P'}}/H\overline{\overline{K'}}$ ) and its dependence on the convective Froude number.

and  $k_x$  (see also Table 4-1). The disturbance kinetic energy inbetween the returning surfaces however is mostly compromised of kinetic energy due to streamwise velocity fluctuation  $u'$ . The dashed line in Figure 4-7, shows the level of  $\overline{u'u'}/\overline{\overline{K'}}$ , which has nearly the same magnitude of disturbance kinetic energy  $\overline{K'}/\overline{\overline{K'}}$ , therefore the lateral velocity fluctuation component  $v'$  is negligible inbetween the returning surfaces. The location of the returning surfaces  $y_t$  according to general formulation by Balmforth (1999) and Takehiro & Hayashi (1992), is where the local velocity  $U$  matches the phase (real) velocity of the consistent structure  $c_p$  plus and minus the speed of the gravity waves  $\sqrt{gH}$ . In a temporal mixing layer, at the returning surfaces the current speed relative to the free streams, is equal to the gravity-wave speed.

$$U_1 - U_+(y_t) = \sqrt{gH} \quad \text{and} \quad U_2 - U_-(y_t) = -\sqrt{gH} \quad (4.10)$$

Much of the kinetic energy is trapped between the returning surfaces. There are however a great deal of wave activities outside of the returning surfaces. Figure 4–8(a) shows the surface wave profiles as defined by the disturbance potential energy  $gh'|h'|/(2H\overline{K'})$  for the case of  $Fr_c = 1.4$  and  $k_x = 0.35$ . The structure of these modulating profiles at times  $T/4$ ,  $T/2$ ,  $3T/4$  and  $T$  are similar but not constant over the modulating period. The magnitude of surface wave profiles are significant both inbetween returning surfaces and in the outer region. The streamwise velocity fluctuation  $u'$  (Figure 4–8(c)), in the outer region is comparable to lateral velocity fluctuation  $v'$  (Figure 4–8(b)). Inbetween the returning surfaces on the other hand  $v'$  is negligible.

#### 4.7 Entrapment and Radiation of Waves

Entrapment and radiation of waves are characteristics of the supercritical instabilities. Figure 4–9 shows the ratio of averaged disturbances' potential to kinetic energy over the computational domain. As an indicator of the depth fluctuations, this averaged potential energy increase with the convective Froude number reaching a saturation value of  $\overline{gh'^2}/(2H\overline{K'}) \simeq 0.75$  for the supercritical flow when  $Fr_c > 1$ . It is clear that the wave activities increase with the convective Froude number.

The waves may or may not transmit the waves' energy to its surrounding. The transmission capability of the waves is the wave power which is a vector with two components  $P_x = (\frac{1}{2}(u^2 + v^2) + gh) uh$  and  $P_y = (\frac{1}{2}(u^2 + v^2) + gh) vh$ . The average of the wave power in the  $y$ -direction over the wave length  $\lambda_x$  is

$$\overline{P}_y = \frac{1}{\lambda_x} \int_0^{\lambda_x} \left( \frac{1}{2}(u^2 + v^2) + gh \right) vh dx, \quad (4.11)$$

This wave power increases exponentially with the growing waves. Figure 4–10 shows the lateral distribution of the averaged wave power  $\overline{P}_y(y, t)$  at time  $t$  normalized by the averaged kinetic energy  $\overline{K'}(t - y/\sqrt{gH})$  at an earlier time  $(t - y/\sqrt{gH})$  when the wave power was initiated. The lateral distribution of  $P_y$  as shown in Figure 4–10 (a) for the subcritical instabilities ( $Fr_c = 0.7$ ,  $k_x = 0.6$ ) is quite different from the distribution in Figure 4–10 (b) for the case of supercritical instabilities ( $Fr_c = 1.4$ ,  $k_x = 0.35$ ). The distribution for the subcritical instabilities in (a) is time independent. The distribution for the supercritical instabilities in (b) on the other hand is modulating and has a consistent modulation period over the time during the linear development. The amplitude of modulation is shown with gray error bars in Figure 4–10 (b). For subcritical instabilities, the peak normalized wave power occurs at the edges of the computational domain. For supercritical instabilities, the magnitude of modulation is significant, however the average wave power is lower compared to subcritical instability.

The wave power escapes the computational domain at the two edges. This wave power evaluated at  $y = \pm 6 \delta_{\omega o}$  is the wave radiation. Figure 4–11 shows the dependence of this radiation power on time. The subcritical instabilities have a constant time independent radiation. The radiation of the supercritical instabilities, on the other hand, is modulating around a rather small flux. Figure 4–12 shows the dependence of the radiation power on convective Froude number. The returning surfaces are effective wave guides that keep the waves confined. The radiation power for the supercritical instabilities is quite small by comparison despite the production of the huge wave power in-between the returning surfaces (see Figure 4–10 (b)). The

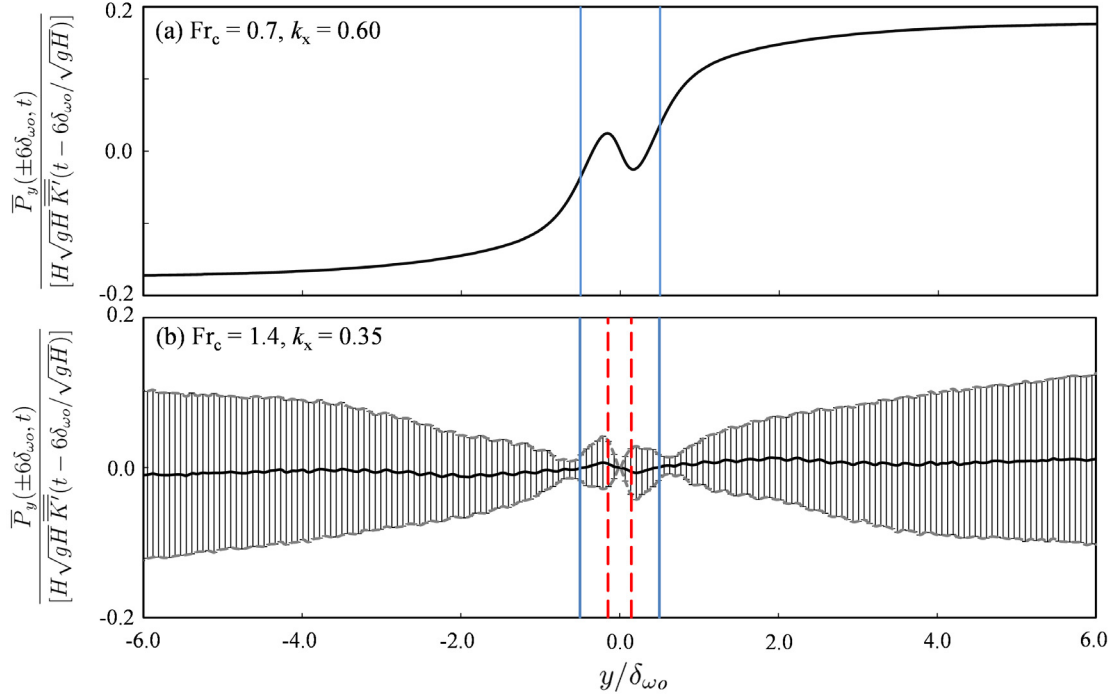


Figure 4-10: The lateral distribution of the wave power  $P_y(y, t)/[H\sqrt{gH}\overline{K'}(t - y/\sqrt{gH})]$  for (a)  $Fr_c = 0.7$ ,  $k_x = 0.6$  and (b)  $Fr_c = 1.4$ ,  $k_x = 0.35$ . The blue lines mark the vorticity thickness and the red dashed lines the returning surfaces.

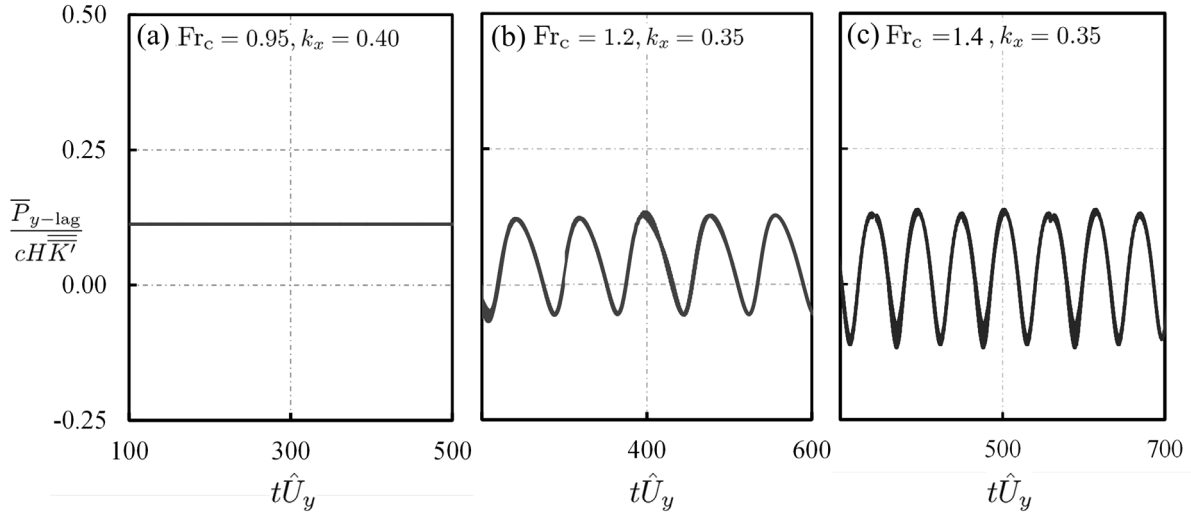


Figure 4-11: Radiation at  $y = \pm 6\delta_{\omega_0}$ , for  $\overline{P}_y(\pm 6\delta_{\omega_0}, t)/[H\sqrt{gH}\overline{K'}(t - 6\delta_{\omega_0}/\sqrt{gH})]$  for (a)  $Fr_c = 0.95$ ; (b)  $Fr_c = 1.20$  and (c)  $Fr_c = 1.4$ .

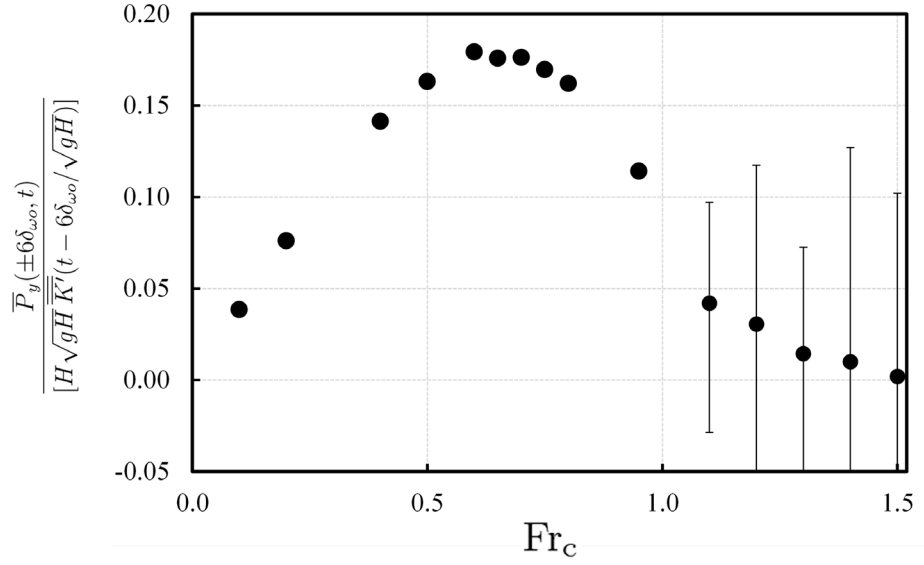


Figure 4–12: Wave radiation power and its dependence on the convective Froude Number. The symbol  $\bullet$  defines the averaged value of the normalized power.

subcritical instabilities are unbounded. Wave intensity increases with the convective Froude. The maximum of the normalized radiation has a value

$$\frac{\overline{P}_y(\pm 6\delta_{\omega o}, t)}{[H\sqrt{gH}\overline{K'}(t - 6\delta_{\omega o}/\sqrt{gH})]} \simeq 0.18, \quad (4.12)$$

which occurs at the subcritical convective Froude number of  $Fr_c \simeq 0.7$ . The value of this normalized radiation reduces to a value of 0.1 at  $Fr_c = 1.0$ . The radiation is modulating about zero for the supercritical instability with the convective Froude number  $Fr_c \simeq 1.5$ . The error bars at  $Fr_c > 1.0$  represent the modulation of radiation power in Figure 4–12. At high convective Froude numbers waves are mostly trapped between the returning surfaces. The period of the modulation of the waves inside and outside of the trapped region has been determined. The normalized modulation

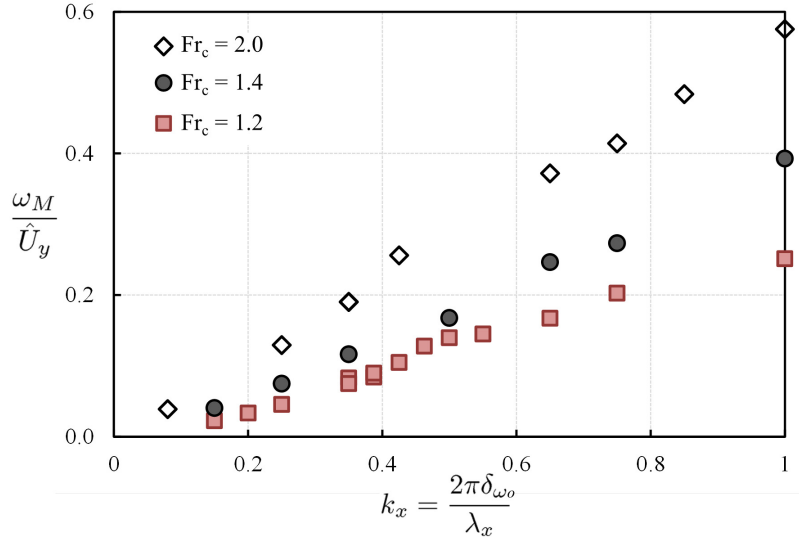


Figure 4–13: Frequency of the modulation  $\omega_M/\hat{U}_y$  and its dependence on the wave number  $k_x$  in the waves trapped between the returning surfaces for  $Fr_c = 1.2, 1.4$  and  $2.0$ .

period is a function of convective Froude number and wave number as shown in Figure 4–13.

#### 4.8 Summary and Conclusion

The direct numerical simulations of the shallow-water equations have been carried out for the base flow with a hyperbolic tangent velocity profile. The method has been validated as the simulation results are comparable with the classical results obtained by the method of the normal mode. The structural descriptions in the linear development of the supercritical instabilities are provided beyond the range of convective Froude numbers examined by the classical method. The highest level of wave radiation from the instabilities occurs in the subcritical range. The simulations

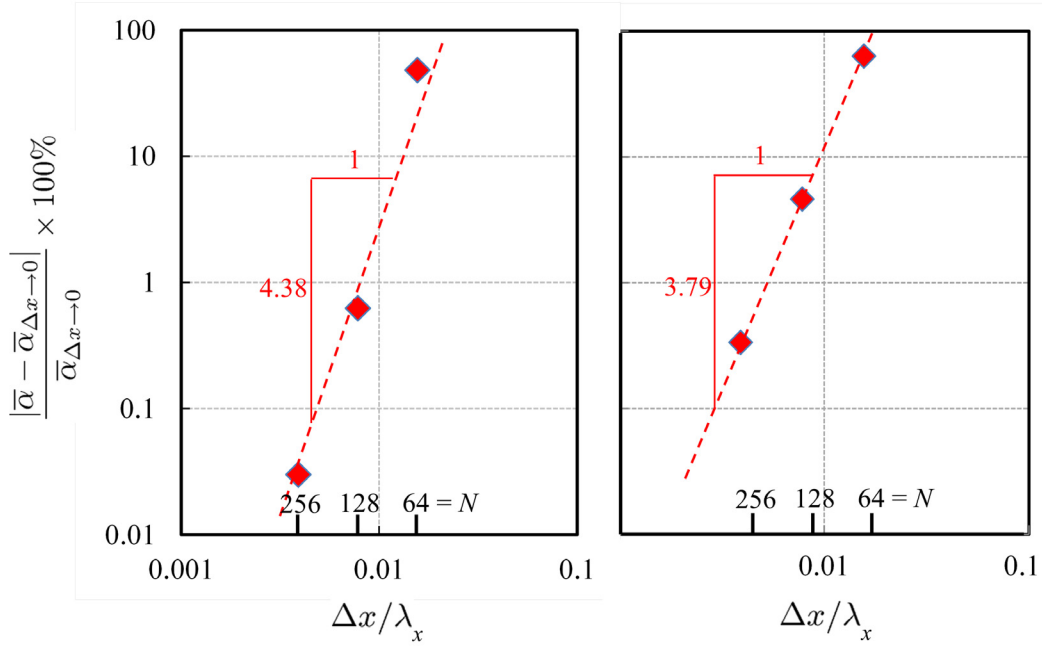


Figure 4–14: Estimated fractional error for the averaged growth rate,  $\bar{\alpha}/\hat{U}_y$ , obtained from the calculations of the fractional growth rate for the supercritical instability with convective Froude number equal to  $Fr_c = 1.2$  (left) and  $Fr_c = 1.4$  (right) at  $k_x = 0.35$ . The levels of error at  $N = 256$  are 0.03% and 0.33% for  $Fr_c = 1.2$  and 1.4, respectively.

have provided details of the wave entrapment inbetween the returning surfaces in the supercritical instabilities.

## Appendix: Numerical Computation

The numerical simulations for the instabilities were conducted using the Weighted Essentially Non-oscillatory (WENO) scheme developed by Shu (1998) using a five-point interpolation stencil. Time integration was carried out by a fourth order Runge-Kutta procedure. The detailed implementation for subcritical instability is given in Karimpour & Chu (2014). Table 4–2 shows how the simulation results obtained for one supercritical instabilities converge to true solution as the grid is refined from  $N = \lambda_x/\Delta x = 64, 128$  to 256. The convergence towards the true solution is shown

Table 4–2: The convergence of averaged growth rate  $\bar{\alpha}/\hat{U}_y$ .

Fr <sub>c</sub>	$k_x$	$N$	$\delta_{\omega_0}/\Delta x$	$\bar{\alpha}/\hat{U}_y$	Error (%)	Order
1.20	0.35	64	3.57	0.0202	48.04	–
1.20	0.35	128	7.14	0.01373	0.62	4.38
1.20	0.35	256	14.28	0.01365	0.03	–
1.20				<b>0.01364</b>		
1.40	0.35	64	3.57	0.0153	63.31	–
1.40	0.35	128	7.14	0.0098	4.60	3.78
1.40	0.35	256	14.28	0.0094	0.33	–
1.40				<b>0.00937</b>		

in Figure 4–14. Orders of convergence are 4.38 and 3.78 for Fr<sub>c</sub>=1.2 and 1.4, respectively.

## CHAPTER 5

### WAVE AND ENERGY DISSIPATION IN SUBCRITICAL AND SUPERCRITICAL MIXING LAYERS

S. Karimpour Ghannadi and V. H. Chu. Wave and Energy Dissipation in Subcritical and Supercritical Mixing Layers. *Journal of Fluid Mechanics*, Draft for submission, 2014.

#### 5.1 Abstract

Direct Numerical Simulations (DNS) have been carried out to study the transition from linear to non-linear instability using a one-layer shallow water equations. The development of non-linear instability is highly influenced by the dilation and total energy dissipation. The transition from linear to non-linear instability occurs very rapidly. During this transition the energy level, flow pattern and the disturbance kinetic energy change drastically. Mixing layer growth rate reduces with convective Froude number which is in agreement with the available experimental and numerical investigations in gas dynamics. Total energy dissipation emerges at intermediate Froude number of 0.75 and impacts the configuration of non-linear eddy. The study of anisotropy tensor has revealed substantial change in the distribution of turbulence kinetic energy with convective Froude number.

**Keywords:** Mixing Layer; Convective Froude Number; Discontinuity; Radiation; Anisotropy

## 5.2 Introduction

The mixing of mass and momentum across shear flows at high Froude number are governed by processes not solely describable by the conventional theory of turbulence. Waves have dominant influence on the exchange process across the turbulent shear layer. Despite the common occurrence of such flow features in steep channels and density stratified flows, only literature available are in compressible flow. Understanding of the phenomenon in compressible flows is necessary to comprehend the flow in gravity-driven mixing layers. Studies in compressible gas dynamics on the effect of compressibility have revealed that the growth rate of shear layer substantially changes with Mach number. Early evidence of compressibility impact on turbulence was discussed by Bradshaw (1977). Later direct numerical simulations also verified the effect of compressibility. The review of these works can be found in Lele (1994).

Experimental observations by Samimy & Elliot (1990), Rossman *et al.* (2002) reported the reduction of thickness growth rate with convective Mach number. Vreman *et al.* (1996) among others have numerically shown that the reduction in shear production is due to radiation dissipation as the Mach number increases. There is also evidence that the turbulence structure changes as Mach number increases. The experiment by Papamoschou & Roshko (1988) further explained the intriguing structure of vortex in the presence of shock waves and hydraulic jumps as “eddy shocklets”.

Although there has been significant progress in the understanding of compressible mixing layer, little to no data are available in the free-surface flow on the interaction of eddy and shocklet. In this paper, the transition from linear to non-linear

instability of a temporal mixing layer is studied numerically using shallow water equations. Data from simulation are analyzed to investigate the effect of dilation and shocklets on (i) total energy dissipation; (ii) radiation and (iii) anisotropy.

### 5.3 Formulation and Numerical Methods

The temporal evolution of mixing layer is numerically solved using single-layer shallow water equations. Free stream velocities are equal and opposite on two sides of the mixing layer. Flow is inviscid and the mixing layer is simulated for  $0 < x < \lambda_x$  and  $y^- < y < y^+$ , where  $|y^+| = |y^-| = 5\lambda_x$  and  $2\lambda_x$  in subcritical and supercritical shear layers, respectively. Wave length of  $\lambda_x$  is chosen to provide the maximum linear growth rate at given convective Froude number.  $x$ - and  $y$ -coordinates correspond to streamwise, and lateral directions. The boundary condition in  $x$ -direction is periodic. In  $y$ -direction, a Sommerfeld radiating boundary condition is applied. This boundary was extensively verified by Nycander & Döös (2003). The mixing layer consists of a tangent hyperbolic profile for the streamwise velocity and a uniform depth of  $H$ . The streamwise velocity profile is:

$$U = \frac{1}{2}(U_1 + U_2) + \frac{1}{2}(U_1 - U_2) \tanh \frac{2y}{\delta_{\omega o}} \quad (5.1)$$

where  $|U_1| = |U_2| = 0.5$  and  $\delta_{\omega o} = 1$  is the initial vorticity thickness. The streamwise velocity profile given by Equation (5.1) is an approximation to fully developed mixing-layer profile (Metcalf *et al.* 1987). Based on the definition of convective Mach number by Brown & Roshko (1974), convective Froude number is defined as:

$$\text{Fr}_c = \frac{U_1 - U_2}{c_1 + c_2} \quad (5.2)$$

Table 5–1: Specification of direct numerical simulation databases: convective Froude number, domain and grid size.

Fr <sub>c</sub>	$L_x \times L_y$	$\Delta x$	Fr <sub>c</sub>	$L_x \times L_y$	$\Delta x$
0.1	7.0400 × 70.400	0.0275	0.75	11.4176 × 114.176	0.0446
0.2	7.2960 × 72.960	0.0285	0.80	12.416 × 124.16	0.0485
0.4	7.8336 × 78.336	0.0306	0.95	16.000 × 160.00	0.0625
0.5	8.4992 × 84.992	0.0332	1.10	17.920 × 71.68	0.070
0.6	9.2416 × 92.416	0.0361	1.20	17.920 × 71.68	0.070
0.65	9.9328 × 99.328	0.0388	1.40	17.920 × 71.68	0.070
0.70	10.5472 × 105.472	0.0412			

where  $c_1$  and  $c_2$  are the speed of gravity waves in the free streams across the mixing layer. Numerical experiments are conducted with fixed initial velocity distribution of free-surface mixing layer but with various initial depths. Mixing layer for this study is considered to be symmetric in  $y$ -direction and therefore local free stream Froude numbers as well as convective Froude numbers are equal and all subcritical or supercritical simultaneously. Numerical experiments are conducted for Fr<sub>c</sub> from 0.1 to 1.4. Simulations for higher convective Froude numbers are being conducted that will be reported separately. Summary of numerical conditions including domain size and grid size are given in Table 5–1. The simulations in all cases are conducted using Minimal Intervention Strategy proposed by Pinilla *et al.* (2010) and further developed by Karimpour & Chu (2014). The time integration was carried out using 4<sup>th</sup> order Runge-Kutta scheme. An upwind biased 5<sup>th</sup> WENO scheme (see, e.g., Shu 2009) was employed for spatial discretization. The 5<sup>th</sup> order WENO was used, as it efficiently captures the discontinuity with minimum accuracy of 3<sup>rd</sup> order, while

maintaining 5<sup>th</sup> accuracy over vortices. The performance of this scheme in compressible mixing layer was conducted by Karimpour & Chu (2014), and the grid size selected for this study has shown 0.1% to less than 0.01% errors in  $Fr_c = 0.8$  and 0.1, respectively.

## 5.4 General Results

Figure 5–1 shows the streamwise vorticity distribution for three cases of  $Fr_c = 0.1, 0.8$  and 1.1. In all three the main stream flow velocities are unchanged and pressure change imposes the local and convective Froude numbers. These cases represent three distinct behaviors in the mixing layer.  $Fr_c = 0.1$  illustrates the roll-up of the vortex, with negligible dilation effect. The transition from fast-growing linear to fully saturated non-linear stage occurs very fast in this case. Growth rate of the mixing layer thickness is the highest as well as the linear growth rate (Michalke 1964). The vorticity is concentrated within the roll up and along the vortex blade. High level of disturbance kinetic energy enhances the entrainment process of the two flows across the mixing layer. At Froude number of  $Fr_c = 0.8$ , the hydraulic jumps begin to appear across the vortex. The shock discontinuity accompanied by eddy roll-up forms a shocklet structure.

Although the convective Froude number hasn't reached the critical level of 1, the supercritical behavior begins to appear and influence the vorticity distribution across the shocklet. This is consistent with observation in analogous flow of compressible gas by Sandham & Reynolds (1990). They have observed that the compressibility effects emerge in mixing layers even at moderate convective Mach numbers greater than 0.7.

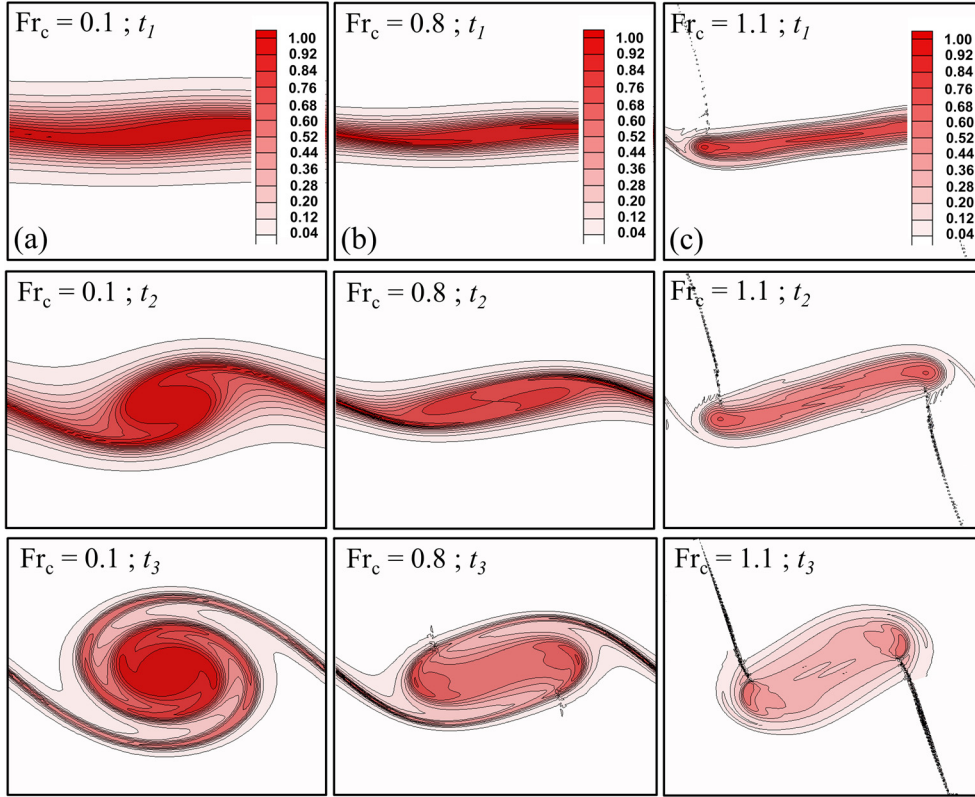


Figure 5-1: Vorticity evolution in the transition from linear to non-linear stages  $t_1$  to  $t_3$  for (a)  $Fr_c = 0.1$ , (b)  $Fr_c = 0.8$  and (c)  $Fr_c = 1.1$ .

This observation in mixing layers of lower convective Froude numbers demonstrates that although the convective Froude number describes the relative structure of mixing layer well, it does not necessarily explain the compressibility effect at subcritical convective Froude numbers. Furthermore at  $Fr_c = 1.1$ , both main stream and the convective Froude numbers become supercritical. This is where we start to observe the continuous formation of hydraulic jumps accompanied by eddy roll-up. Also structure of the eddy and shocklet evolves with convective Froude number. At low convective Froude numbers ( $Fr_c = 0.1$ ) the vorticity concentration profile at fully developed stage of  $t_3$  resembles the cat's eye vortex by Stuart (1967). However

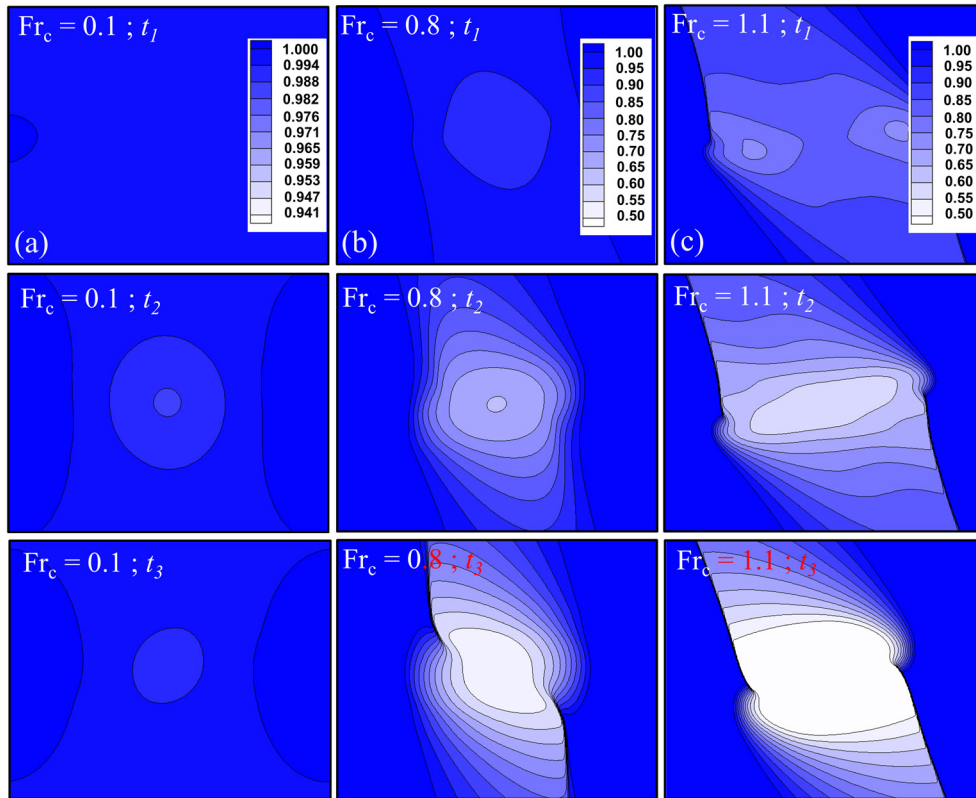


Figure 5-2: The relative depth ( $h/H_o$ ) evolution in the transition from linear to non-linear at stages  $t_1$  to  $t_3$  for (a)  $Fr_c = 0.1$ , (b)  $Fr_c = 0.8$  and (c)  $Fr_c = 1.1$ .

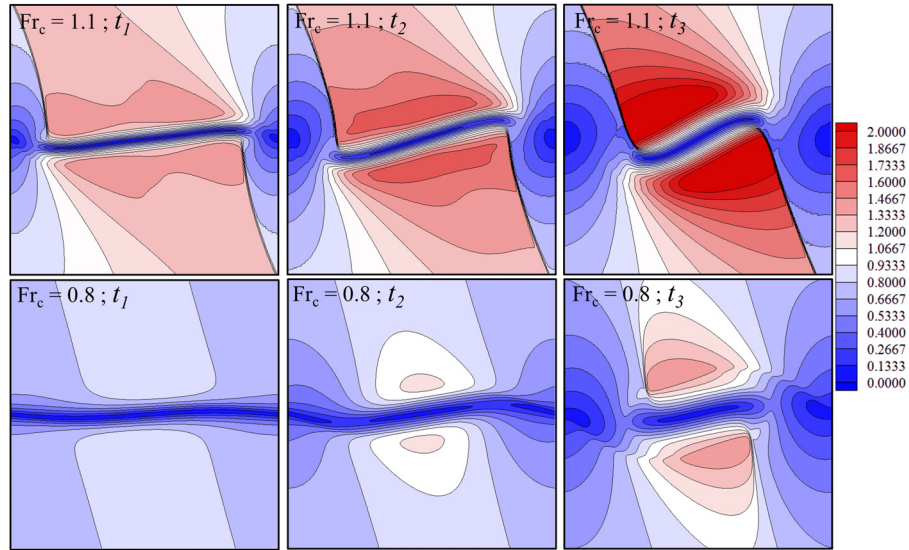


Figure 5–3: Evolution of local Froude number over transition from linear to non-linear instability. The top row identifies stages  $t_1$  to  $t_3$  in  $Fr_c = 1.1$  and the bottom row, identifies these stages in  $Fr_c = 0.8$ .

as the convective Froude number progressively increases, the shocklet stretches in the streamwise direction while compresses in the lateral direction. The shocklet elongation continues as the convective Froude number extends beyond critical level of  $Fr_c = 1.0$ . Figure 5–2 illustrates that the formation of shocklets also accompany pressure fluctuation. In three stages of development of a subcritical flow in Figure 5–2(a) the negligible depth variation from initial profile is just to maintain the rotation. However as convective Froude number rises, the pressure fluctuation from initial pressure increases. At  $Fr_c = 0.8$  and  $Fr_c = 1.1$  the water depth decreases as much as 50% and 75% of the initial water depth, respectively. The depth discontinuities that are evident in Figures 5–2 (b) and (c) are due to sudden change of local Froude number from supercritical (red in Figure 5–3) to subcritical (blue in Figure 5–3). Therefore the behaviour of the mixing layer cannot be explained solely through the

convective Froude number. The local Froude number impacts the evolution of the vortex and formation of vortex blades as it can be detected at  $Fr_c = 0.8$ .

## 5.5 Mixing Layer and Growth

The mixing layer thickness can be defined based on the two properties: i) the thickness according to the maximum slope, which initially defines the thickness of vorticity profile. Therefore thickness estimated from maximum slope which evolves in time, is called vorticity thickness:

$$\delta_\omega = \frac{U_1 - U_2}{\hat{U}_y} \quad (5.3)$$

where  $\hat{U}_y$  is  $\partial U / \partial y$  on the inflection point. ii) The momentum thickness: this shows the relative deficiency of momentum across the shear layer, due to velocity distribution with respect to the momentum generated by a flow with  $U_1 - U_2$  velocity. With the main flow velocity on each side of  $|U_1| = |U_2| = 0.5$ , momentum thickness is defined as:

$$\delta_\theta = \int_{y^-}^{y^+} \frac{U - U_2}{U_1 - U_2} \left( 1 - \frac{U - U_2}{U_1 - U_2} \right) dy = \int_{y^-}^{y^+} (0.5 + U)(0.5 - U) dy \quad (5.4)$$

However due to the initial distribution of our velocity profile, the momentum thickness starts from the value of  $\delta_{\theta o} / \delta_{\omega o} = 0.25$  in the linear stage. Therefore in order to maintain consistency between two initial values of vorticity and momentum thicknesses, momentum thickness is reported as  $4\delta_\theta$  instead, throughout this paper. Figure 5-4 shows the evolution of momentum and vorticity thicknesses in time, in subcritical and transcritical mixing layers. The normalized time is defined as  $t\hat{U}_y$ . The initiation

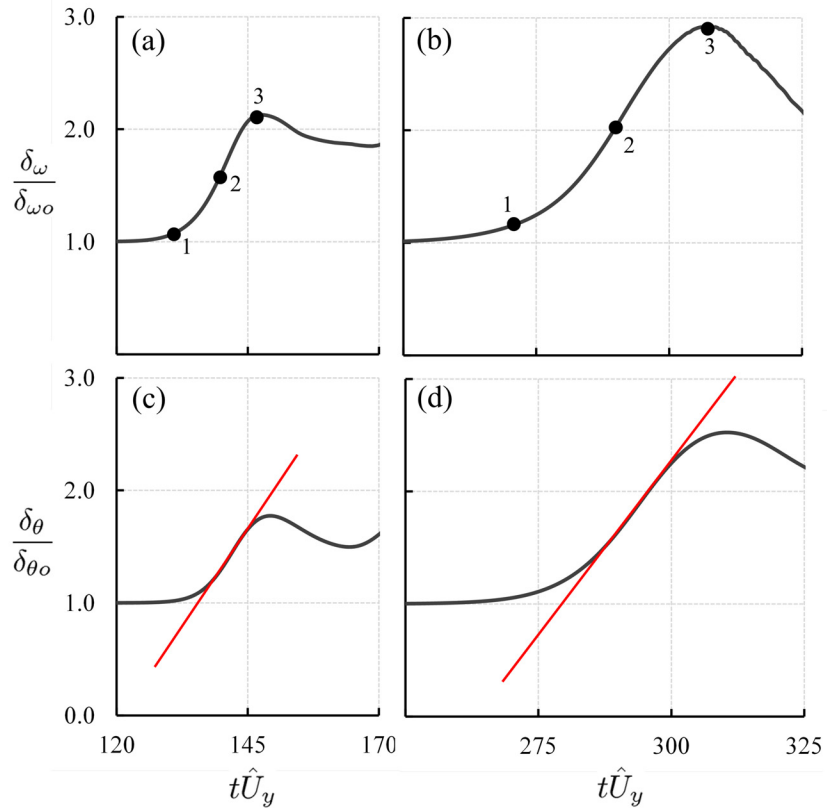


Figure 5-4: Vorticity thickness evolution for (a)  $Fr_c = 0.1$  and (b)  $Fr_c = 0.8$  and momentum thickness evolution for (c)  $Fr_c = 0.1$  and (d)  $Fr_c = 0.8$ . In (a) and (b) three points are marked that represent the initiation, inflection and saturation stages in non-linear development. In (c) and (d) the growth rate of momentum thickness is marked with red line. Growth rate of the momentum thickness,  $4\dot{\delta}_\theta$  drops from 0.076 to 0.061 from  $Fr_c = 0.1$  to  $Fr_c = 0.8$ .

of non-linear development depends directly on the linear growth rate (Sandham & Reynolds 1990). At  $Fr_c = 0.1$  the non-linear development starts earlier than  $Fr_c = 0.8$  as the linear growth rate in  $Fr_c = 0.8$  is about 2.4 times smaller than 0.1 (Pinilla & Chu 2008). The maximum linear growth rates for these convective Froude numbers don't occur at the same wave number either. At  $Fr_c = 0.1$  and 0.8 the maximum growth rates occur at approximately  $k_x = 2\pi/\lambda_x = 0.89$  and 0.53, respectively. The transition from linear to saturate non-linear is marked and later demonstrated with three stages: (1) initiation; (2) inflection and (3) saturation. These stages are the reference points to investigate the development of the mixing layer. Figure 5–4 (c) and (d) demonstrate the growth rate of momentum thickness ( $4\delta_\theta$ ). For  $Fr_c = 0.1$  and 0.8, growth rates for  $4\delta_\theta$  are 0.076 and 0.061. The growth rate of the momentum thickness in the quasi-incompressible reported by Pantano & Sarkar (2002) from DNS of incompressible gas at very low convective Mach number of 0.3 was  $\dot{\delta}_\theta = 0.0184$ . In the present analysis, growth rate of momentum thickness,  $\dot{\delta}_\theta$ , was measured to be  $= 0.0189$  and  $0.0180$  for  $Fr_c = 0.1$  and  $0.2$ , respectively. Also Vreman & Sandham (1996) reported  $\dot{\delta}_\theta = 0.073$  for  $Ma_c = 0.2$  with  $U_2 - U_1 = 2.0$ . Therefore the initial momentum thickness and momentum thickness growth rate by Vreman & Sandham (1996) is 4 times greater than results reported by Pantano & Sarkar (2002) and the present investigation. Also the fractional rate of vorticity thickness,  $\dot{\delta}_\omega/\delta_\omega$ , at  $Fr_c = 0.1$  in the limiting case where the dilation effect is negligible is comparable to the rate obtained from the laboratory experiments which were carried out in steady flow. The temporal variation of vorticity thickness, obtained from the present simulations may be related to the spatial development of the mixing layer in steady flow.

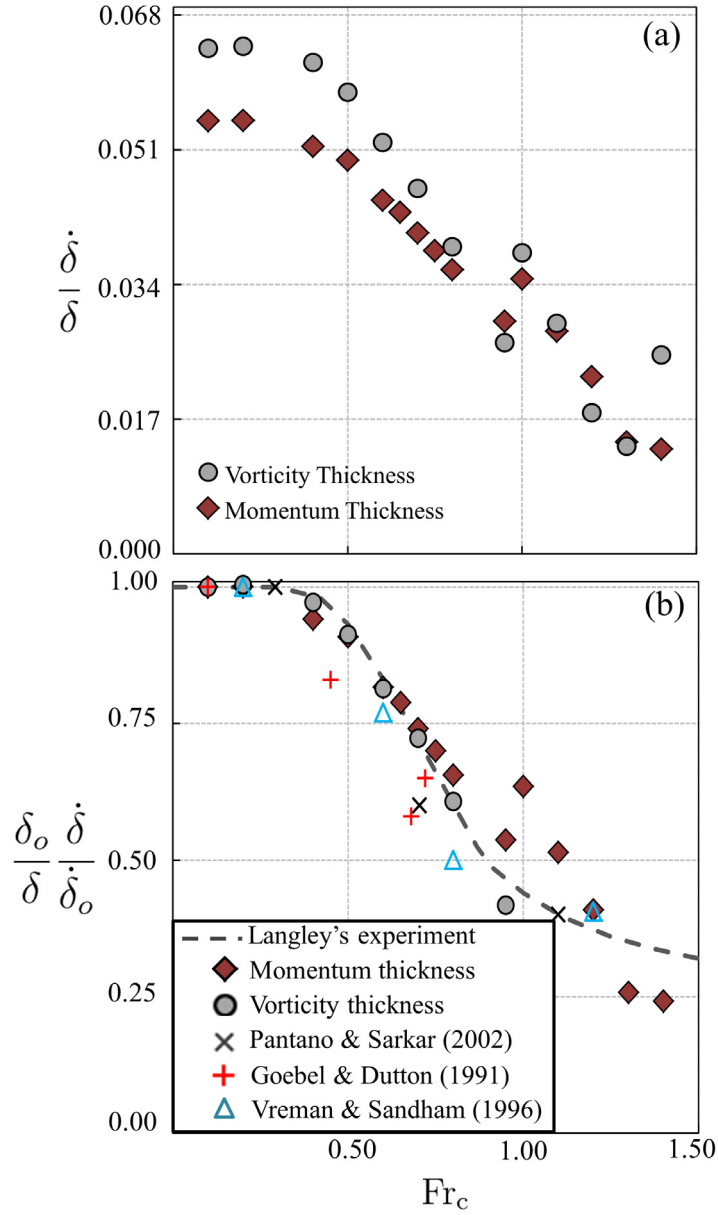


Figure 5-5: (a) Dependence of the fractional thickness growth rate with  $Fr_c$  for momentum,  $\delta_\theta$ , and vorticity thickness,  $\delta_\omega$ . (b) The ratio of the growth rate to dilation free growth rate, is plotted versus  $Fr_c$  and compared with experimental and numerical observations in flows with high Reynolds numbers in gas dynamics.

$$\begin{aligned}
\frac{1}{\delta_\omega} \frac{\partial \delta_\omega}{\partial(t\hat{U}_y)} &= 0.063 \\
\frac{1}{\delta_\omega} \frac{\partial \delta_\omega}{\partial x} \frac{\partial x}{\partial t} &= 0.063 \frac{U_1 - U_2}{\delta_{\omega o}} \\
\frac{1}{\delta_\omega} \frac{\partial \delta_\omega}{\partial x} \frac{U_1 + U_2}{2} &= 0.063 \frac{U_1 - U_2}{\delta_{\omega o}} \\
\frac{\partial \delta_\omega}{\partial x} &= 2 \times 0.063 \frac{U_1 - U_2}{U_1 + U_2} \frac{\delta_\omega}{\delta_{\omega o}}, \quad \left( \frac{\delta_\omega}{\delta_{\omega o}} \right)_2 = 1.6 \\
\frac{\partial \delta_\omega}{\partial x} &= 0.202 \frac{U_1 - U_2}{U_1 + U_2}
\end{aligned} \tag{5.5}$$

which is very close the following spreading rate obtained from laboratory experiment by Brown and Roshko (1974):

$$\frac{\partial \delta_\omega}{\partial x} = 0.188 \frac{U_1 - U_2}{U_1 + U_2} \tag{5.6}$$

The thickness of the mixing layer depends on the convective Froude number. As reported in compressible flow the thickness of the mixing layer decreases with convective Mach number according to both experimental and numerical investigations (see, e.g., Gatski & Bonnet 2013; Samimy & Elliott 1990; Pantano & Sarkar 2002). The similar behaviour is expected for open-channel free-surface mixing layer as seen in Figures 5–5(a) and (b). Growth rates of vorticity and momentum thicknesses decrease as the convective Froude number increases. This is likely due to the total energy dissipation and radiation dissipation at higher convective Froude numbers. The growth and development of momentum and vorticity thicknesses are influenced by the overall energy available to the mixing layer as well as the disturbance kinetic energy. The reduced thickness growth rate with Froude number in the current

simulation follows the trend observed in previous experimental and numerical investigations in gas dynamics. After validating our findings with available experimental and numerical data on the mixing layer thickness in gas dynamics, we perform analysis on the influence of flow discontinuity and dilation on the total and disturbances energy.

## 5.6 Kinetic and Potential Energy

The mechanical energy available in depth averaged shallow flow is considered in this section. For the analysis of the shallow flow, besides the mass and momentum conservation the use of energy equation is necessary. In inviscid continuous flow the total amount of energy is exchanged between total potential and kinetic energy. However in the event of the hydraulic jump, which is equivalent to shock wave in gas dynamics, the balance of energy doesn't hold and a part of the potential and kinetic energy is converted into internal energy. The energy equation can be derived from the momentum and mass conservation equations. Assuming  $\vec{U} = (u, v)$  and writing the  $x$ -momentum and  $y$ -momentum equations into one vector form and multiplying it by  $\vec{U}h$  we have:

$$\vec{U}h \cdot \frac{\partial \vec{U}}{\partial t} + \vec{U}h \cdot (\vec{U} \cdot \nabla) \vec{U} = -\vec{U}h \cdot \nabla gh \quad (5.7)$$

Also multiplying the continuity equation by  $gh$  we find that:

$$\frac{\partial}{\partial t} \left( \frac{gh^2}{2} \right) + \nabla \cdot [(\vec{U}h)(gh)] = \vec{U}h \cdot \nabla (gh) \quad (5.8)$$

considering the kinetic energy as  $K = \frac{u^2+v^2}{2}$ , Equation (5.7) transforms to:

$$\frac{\partial K}{\partial t} + \nabla \cdot [\vec{U}(K)] = -\vec{U} \cdot \nabla (gh) \quad (5.9)$$

Multiplying Equation (5.9) by  $h$ ,  $-\vec{U}h \cdot \nabla (gh)$  appears in both potential and kinetic energy equations. It represents the energy flux between kinetic and potential energies. Combining Equations (5.8) and (5.9) for potential and kinetic energies, respectively, gives:

$$\frac{\partial}{\partial t} \left( Kh + \frac{gh^2}{2} \right) + \nabla \cdot [\vec{U}h(K + gh)] = 0 \quad (5.10)$$

where total energy ( $E$ ) and hydraulic head ( $H_t$ ) are:

$$E = \frac{(u^2 + v^2)h}{2} + \frac{gh^2}{2} \quad (5.11)$$

$$H_t = \frac{(u^2 + v^2)}{2g} + h \quad (5.12)$$

Therefore the total energy ( $E$ ) is balanced with energy flux vector:

$$\frac{\partial E}{\partial t} + \nabla \cdot [\vec{U}h(gH_t)] = 0 \quad (5.13)$$

Knowledge of energy balance over the domain containing mixing layer helps studying the energy availability and energy flux, in the event of an eddy shocklet. Therefore the above equation over an interrogation zone with the area of  $A$  becomes:

$$\int_A \frac{\partial E}{\partial t} dA + \int_A \nabla \cdot [\vec{U}h(gH_t)] dA = 0 \quad (5.14)$$

The exchange of integral and derivative in the energy flux on the left hand side of Equation (5.14) is only possible on continuous flow field. However through the existence of discontinuity this exchange is only possible through the consideration of

an energy dissipation term. Hence by exchanging integral and derivative in Equation (5.14), using divergence theorem, we obtain:

$$\frac{\partial}{\partial t} \int_A E dA + \oint_s h(gH_t) \vec{U} \cdot \hat{n} ds = \int_A \epsilon dA \quad (5.15)$$

Considering the periodicity of the domain in longitudinal direction, Equation (5.15) can be written as:

$$\frac{\partial}{\partial t} \left( \int_{y^-}^{y^+} \int_0^{\lambda_x} E dx dy \right) + \left[ \int_0^{\lambda_x} gH_t v h dx \right]_{y^+} - \left[ \int_0^{\lambda_x} gH_t v h dx \right]_{y^-} = \int_A \epsilon dA \leq o \quad (5.16)$$

where  $\lambda_x$  marks the size of computational domain in  $x$ -direction and  $y^+$  and  $y^-$  mark the lateral integration limits. Energy is distributed throughout the computational domain including the mixing layer. However in the total energy balance equation, Equation (5.15), only the overall change in energy is tracable. The variation of total energy is mostly noticeable across the mixing layer (see Figure 5–7). Hence the energy drop should only be associated and averaged over the mixing layer thickness:

$$\frac{\partial \bar{E}}{\partial t} + \frac{\bar{P}_{y^+}}{\delta} - \frac{\bar{P}_{y^-}}{\delta} = \bar{\epsilon} \quad (5.17)$$

where  $P_y = gH_t v h$  and  $\delta = 4\delta_\theta$ . For any variable  $a$ ,  $\bar{a}$  is the average over mixing layer area or  $\bar{a}$  over the wave length.

Many of the finite-volume approximations that perform well in practice do not necessarily respect the energy dissipation statement in Equations (5.14) to (5.17), in other words they can be overloaded with an excessive amount of numerical dissipation near shocks, which leads to large numerical errors, particularly for long time integration. Hence, it is highly desirable to design a high-order stable finite-volume

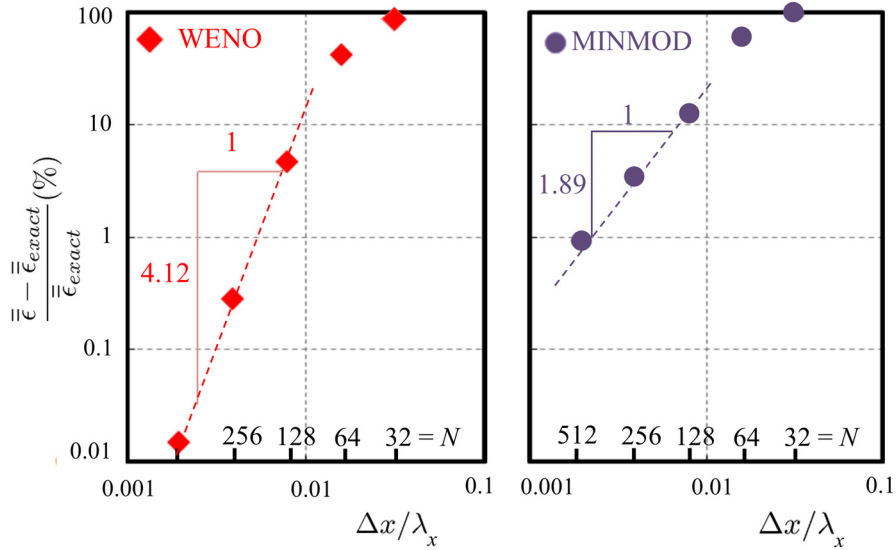


Figure 5–6: The error in energy dissipation using in  $Fr_c = 0.8$  using (a) 5<sup>th</sup> order WENO scheme and (b) MINMOD. WENO exhibits significantly lower level of numerical dissipation compared to MINMOD.

scheme which respects a *faithful* description of the energy balance of the shallow water system. In particular, they add a minimal amount of numerical dissipation which guarantees energy conservation in the smooth regime. In the current simulation the energy conservation is maintained and the level of energy dissipation is minimal, rapidly vanishing with grid refinement. A brief presentation of energy conservation in the present model is through the study of energy dissipation over flow discontinuity. This is demonstrated for transcritical  $Fr_c = 0.8$  where total energy dissipation starts to emerge due to occasional formation of hydraulic jumps. Using 5<sup>th</sup> order spatial interpolation of WENO, total overall energy dissipation for  $Fr_c = 0.8$  converges with more than 4<sup>th</sup> order of accuracy as shown in Figure 5–6.

All the components of Equation (5.15) are plotted in Figure 5–7 for  $Fr_c = 0.6$ , 0.8 and 1.1. In subcritical case of  $Fr_c = 0.6$  in Figure 5–7 (a) the total energy is

in balance with local energy fluxes in  $x$  and  $y$  directions. At  $Fr_c = 0.8$ , on the other hand, the imbalance of total energy and energy flux is noticeable. Energy flux becomes significant across the hydraulic jumps in stages  $t_2$  and  $t_3$ . The location of the hydraulic jump can be identified from Figures 5–2 (b) and (c). The energy dissipation therefore appears across the depth discontinuity. The same process is observed for higher convective Froude numbers as illustrated in Figure 5–7 (d). As the distribution of fluxes in Figure 5–7 shows, energy fluxes are transmitted mainly from the mixing layer. As the total energy flux appears only across the mixing layer, it has to be correlated to the properties of the mixing layer. The transmitted fluxes move with gravity wave speed of  $c$ . The intensity of the disturbance kinetic energy across the mixing layer depends on the intensity of the initial velocity difference. Using the velocity difference across the mixing layer ( $\Delta U = U_1 - U_2$ ), the normal variable representing energy flux as  $\overline{P}_y/H_o\Delta U^2 c$  is meaningful across the mixing zone. Following this normalization for  $\overline{P}_y$ , Equation (5.17) becomes:

$$\frac{1}{H_o\Delta U^2 c/\delta} \frac{\partial \overline{E}}{\partial t} + \frac{\overline{P}_{y^+} - \overline{P}_{y^-}}{H_o\Delta U^2 c} = \frac{\overline{\epsilon}}{H_o\Delta U^2 c/\delta} \quad (5.18)$$

As the convective Froude number rises, flow discontinuities appear as hydraulic jumps emitted from shocklets. These shocklets are initiated at the mixing layer. Therefore the energy dissipation is most significant adjacent to the mixing layer. Figure 5–8 studies the evolution of normalized energy equation in time for  $Fr_c = 0.8$ . Energy rates and dissipations are evaluated in three regions where  $|y^+| = |y^-| = \frac{5}{16}\lambda_x$ ,  $\frac{15}{16}\lambda_x$  and  $\frac{25}{16}\lambda_x$ . The energy fluxes however are plotted at the border of the interrogation zones at  $y^+$ . Although the energy rates and energy fluxes across these regions are

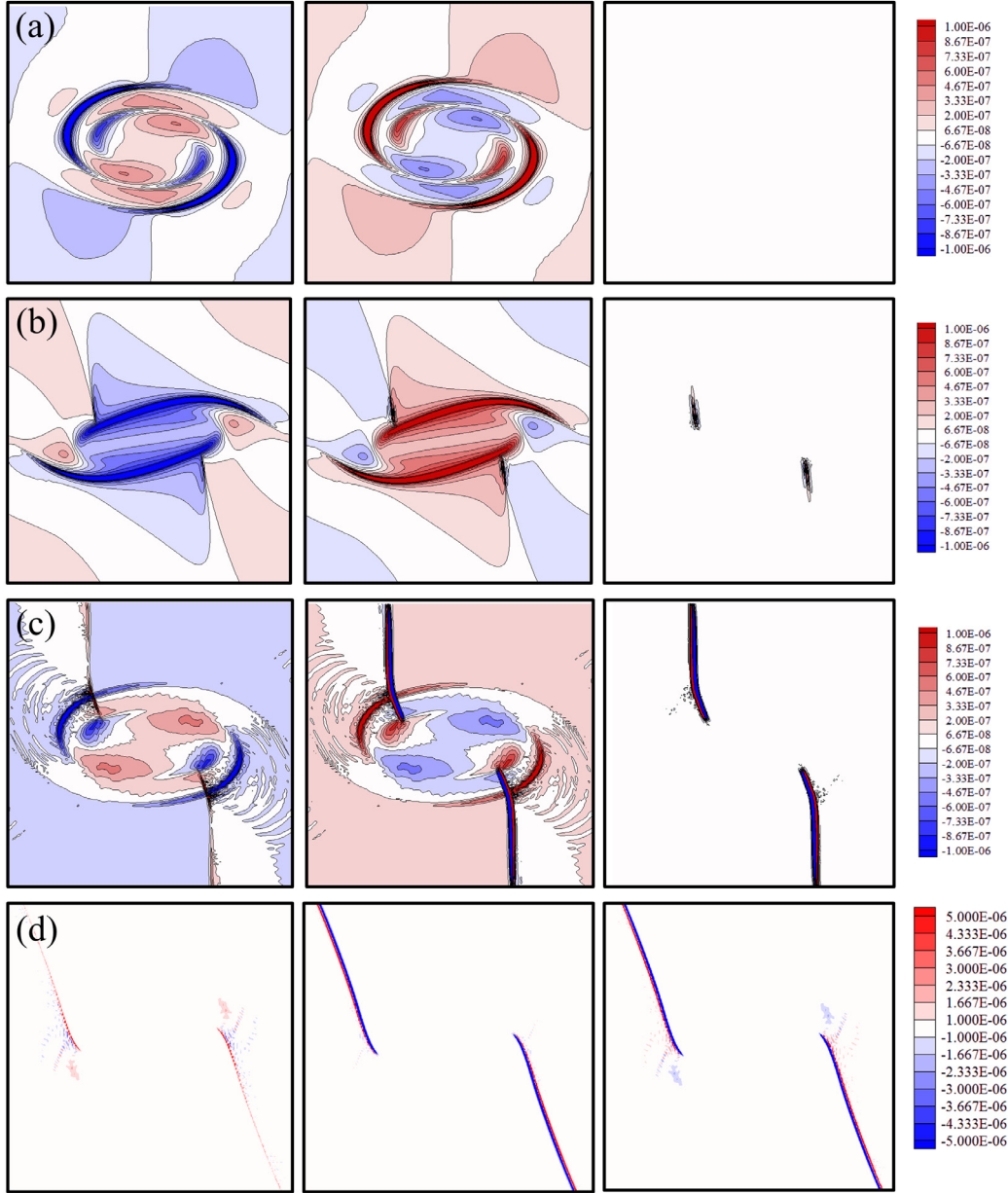


Figure 5–7: The distribution of three terms in Equation (5.15) for (a)  $Fr_c = 0.6$  at stage  $t_3$ , (b)  $Fr_c = 0.8$  at stage  $t_2$ , (c)  $Fr_c = 0.8$  at stage  $t_3$  and (d)  $Fr_c = 1.1$  at stage  $t_3$ . The integration is made over the area of a control volume with the area of  $\Delta x \Delta y$ . The left column represents the rate of change on energy ( $\frac{\partial}{\partial t} \int_A E dA$ ), centre column energy flux ( $\oint_s h(gH_t) \vec{U} \cdot \hat{n} ds$ ) and the right column energy dissipation ( $\int_A \epsilon dA$ ).

different, the energy imbalance, as it appears in the dissipation, is almost identical across different interrogation regions. The maximum energy dissipation occurs at stage  $t_3$  of the development when the shocklet is very strong.

According to Sandham & Reynolds (1991) only at  $\text{Ma}_c = 0.7$  mixing layer starts to emit shock waves. As can be seen in Figure 5–7(a), even at  $\text{Fr}_c = 0.6$ , the energy dissipation is zero, however as the convective Froude number exceeds 0.7 the energy dissipation begins to influence the total energy balance. The energy dissipation increases with convective Froude number in transcritical region with  $0.7 < \text{Fr}_c < 1$ , as shown in Figure 5–9. The energy dissipation reaches an almost constant level at supercritical mixing layer of  $\text{Fr}_c > 1$ . The energy dissipation is an energy sink, converting total energy to internal energy. The shortage of total energy influences the amount of energy that is available for the development of mixing layer. It is reported by Freund *et al.* (2000) and others that the linear growth rate of mixing layer is directly influenced by radiation dissipation. In the non-linear stage however the total energy dissipation also influences the overall energy balance and acts as sink to disturbance and mean potential and kinetic energies available in the system.

## 5.7 Disturbance Kinetic Energy

In shallow-water equations,  $u$ ,  $v$ , velocities in  $x$ - and  $y$ -directions, and  $h$ , the total depth, for the parallel shear flow consist of mean flow as  $U$ , 0 and  $H$  and perturbation from mean as  $u'$ ,  $v'$  and  $h'$ :

$$u = u' + U, \quad v = v', \quad , h = h' + H \quad (5.19)$$

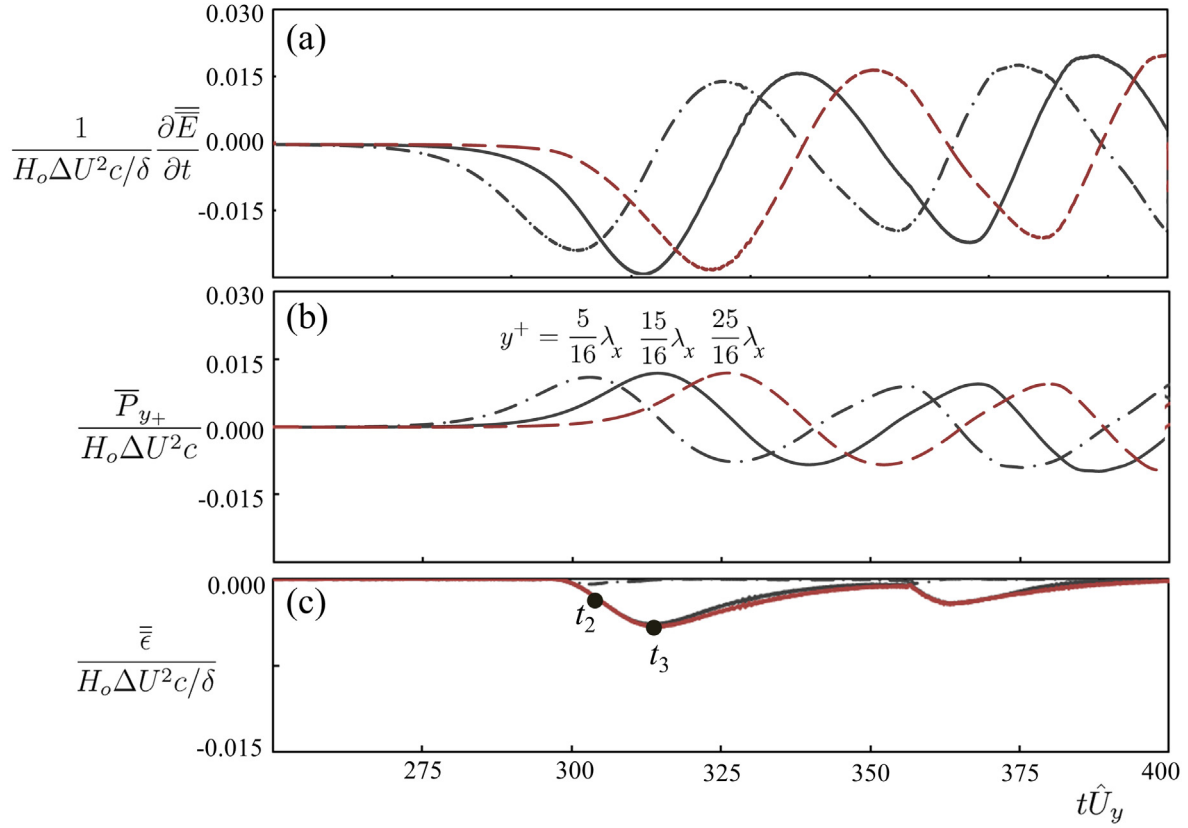


Figure 5-8: The temporal evolution of (a) normal energy rate; (b) normal energy flux and (c) the total energy dissipation as they appear in Equation (5.18) for  $Fr_c = 0.8$ . The interrogation regions are limited to  $|y^+|=|y^-| = \frac{5}{16}\lambda_x, \frac{15}{16}\lambda_x$  and  $\frac{25}{16}\lambda_x$ .

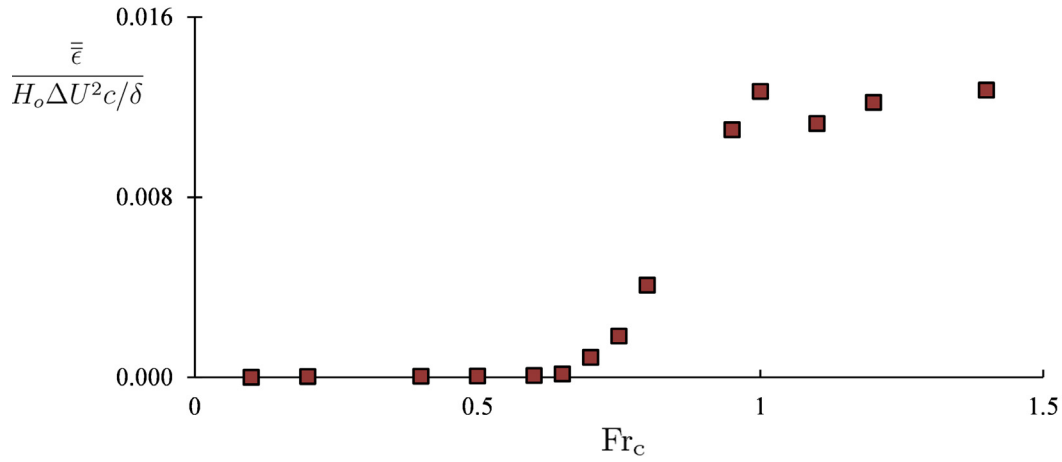


Figure 5-9: Dependence of peak energy dissipation on convective Froude number. The maximum dissipations plotted in this graph occur at the fully saturated stage of  $t_3$ . The maximum dissipation and the maximum thickness are synchronized and emerge simultaneously.

The total energy  $K$  consists of mean and disturbance kinetic energy,

$$K = K' + K_m \quad (5.20)$$

In this mixing layer, since  $v = v'$ , the mean energy only consists on  $x$ - component of the velocity. Using the averaged  $x$ -momentum equation,  $K_m$  takes the form

$$\frac{\partial K_m}{\partial t} + U \frac{\partial K_m}{\partial x} = -\frac{\partial U \overline{u'v'}}{\partial y} + \overline{u'v'} \frac{\partial U}{\partial y} \quad (5.21)$$

Subtracting Equation (5.21) from (5.9) and averaging over the wave length,  $K'$  can be expressed as:

$$\frac{\partial \overline{K'}}{\partial t} + u \frac{\partial \overline{K'}}{\partial x} + \frac{\partial U \overline{u'v'}}{\partial y} = \overline{S} - \overline{R} \quad (5.22)$$

where

$$\overline{K'} = \frac{\overline{u'u'} + \overline{v'v'}}{2}. \quad (5.23)$$

$$\overline{R} = g\overline{u'\frac{\partial h'}{\partial x}} + g\overline{v'\frac{\partial h'}{\partial y}}, \quad \overline{S} = -\overline{u'v'}\frac{\partial U}{\partial y} \quad (5.24)$$

The total energy as explained by Equation (5.17) comprises of kinetic and potential energy. The overall energy consideration proved that the rate of energy dissipation increases as the convective Froude number increases, making less energy available for mixing layer growth in the non-linear stage. This was through energy dissipation over discontinuity as flow locally changes state from subcritical to supercritical. The total kinetic energy on the other hand includes “mean kinetic energy” and “disturbance kinetic energy”. The production term,  $\overline{S}$ , shows the flux of energy between mean energy in Equation (5.21) and disturbance kinetic energy as in Equation (5.22). This production of energy however seems to be independent of convective Froude number and the compressibility has little to no impact on the energy flux from mean to disturbance kinetic energy. The production can be re-defined as following for the numerical simulation of temporal mixing layer at any moment:

$$\overline{\overline{S}} = \frac{1}{\lambda_x \delta_\omega} \int_{-\infty}^{\infty} \int_0^{\lambda_x} \left( -u'u'\frac{\partial u}{\partial y} - v'v'\frac{\partial v}{\partial y} \right) dx dy \quad (5.25)$$

$$\overline{\overline{R}} = \frac{1}{\lambda_x \delta_\omega} \int_{-\infty}^{\infty} \int_0^{\lambda_x} \left( gu'\frac{\partial h'}{\partial x} + gv'\frac{\partial h'}{\partial y} \right) dx dy \quad (5.26)$$

where  $\overline{\overline{S}}$  and  $\overline{\overline{R}}$ , are the disturbance energy production flux and radiation dissipation terms averaged over the thickness of the mixing layer at any instance directly extracted from direct numerical simulation. In higher convective Mach and Froude

numbers, we observe growth rate and the thickness growth decreasing with convective Froude number. This is directly related to the amount of energy available to the disturbances. According to Equation (5.22), the growth of disturbance kinetic energy in time is regulated by both shear production flux and radiation dissipation. Equation (5.22) shows that the disturbance energy rate increases as the production flux from mean flow increases and it drops as the radiation dissipation increases. The development and the balance of these two terms are presented in Figures 5–10 and 5–11. Figure 5–10 and 5–11 show the time dependant distribution of  $\overline{S}$  and  $\overline{R}$  for the linear to non-linear transition. The peak of the averaged energy production coincides with the maximum growth of the mixing layer at the inflection point of momentum and vorticity thicknesses at all Froude numbers. Since the initiation of mixing layer changes with linear growth rate, the delay in the initiation of non-linear development is simply due to smaller linear growth rate in larger convective Froude numbers (Lee *et al.* 1991). Figures 5–10 and 5–11 show that considerable amount of turbulence energy flux is consumed through dissipation dilation at  $Fr_c = 0.8$  and  $1.1$ .  $\overline{S}$  and  $\overline{R}$  are the averaged turbulence production and radiation dissipation through the computational domain directly extracted from direct numerical simulation. The total energy imbalance has shown that the total energy dissipation, in other word the compressibility effect, becomes important in even moderate convective Froude number of  $Fr_c = 0.7$ . Figure 5–7, shows that the total energy dissipation becomes significant in transcritical and supercritical Froude numbers of  $Fr_c > 0.7$ .

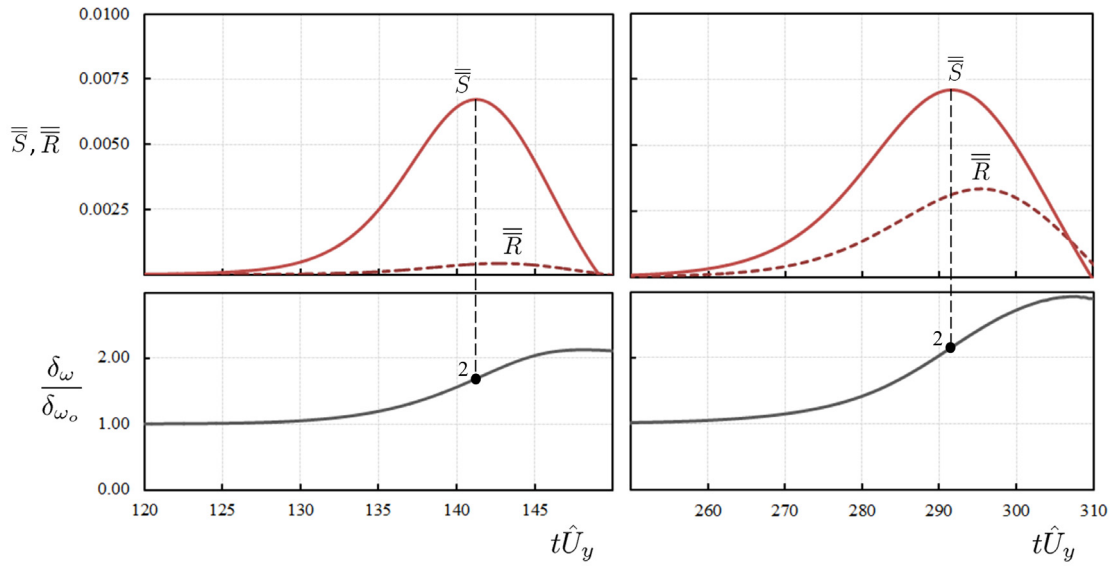


Figure 5–10: The production flux and radiation dissipation through transition from linear to non-linear instability. The level of production is constant in two convective Froude numbers, however the radiation dissipation increases from  $Fr_c = 0.1$  (left) to  $Fr_c = 0.8$  (right). The maximum production in both cases occur right at the inflection point ( $t_2$ ).

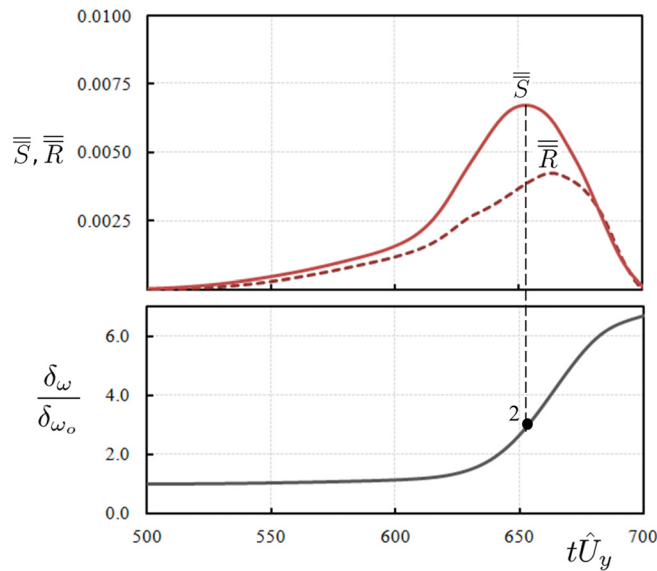


Figure 5–11: The production flux and radiation dissipation through transition from linear to non-linear instability for  $Fr_c = 1.1$ . The radiation dissipation increases further from  $Fr_c = 0.8$  to  $Fr_c = 1.1$ .

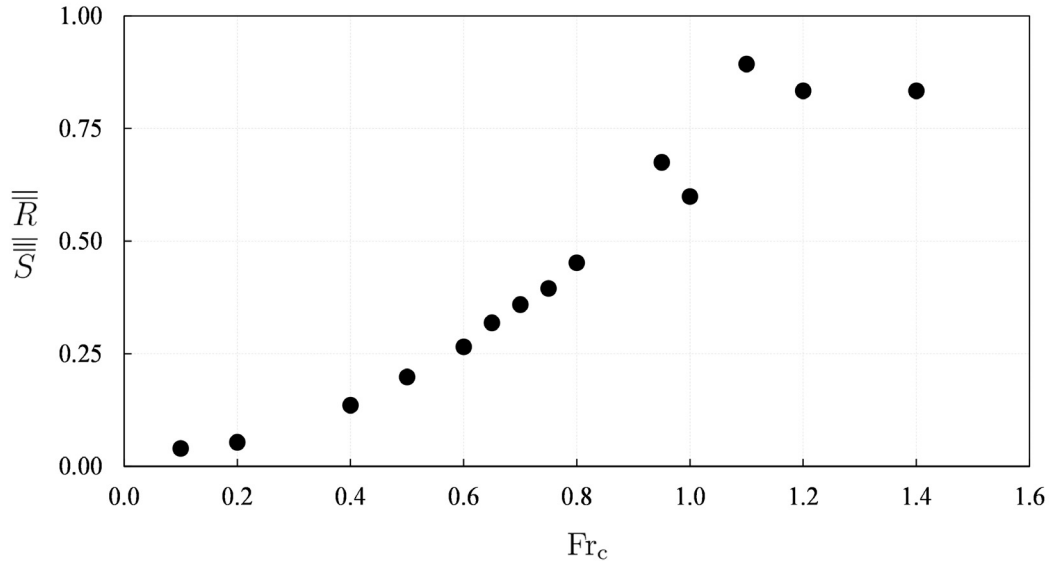


Figure 5–12: Dependence of the overall relative radiation dissipation at the inflection point of  $t_2$  on convective Froude number.

The highest shear production occurs at inflection point of non-linear development. Figure 5–12 illustrates the variation of radiation dissipation term to production flux at  $t_2$ . The radiation dissipation is continuously growing with convective Froude number. At  $Fr_c = 0.10$ , this term is negligible. The total energy at  $Fr_c = 0.6$  did not experience any energy dissipation, since the discontinuity only started to emerge at  $Fr_c = 0.7$ . However even at  $Fr_c = 0.6$  the magnitude of relative radiation dissipation term is significant. This suggests that the radiation dissipation is linked to the reduced growth rate observed in Figure 5–5. However the structure of the eddy is mostly influenced by the total energy dissipation. At  $Fr_c \geq 0.7$ , where the total energy dissipation is non-zero, shocklets-eddy forms. At  $Fr_c < 0.7$  on the other hand, despite evident levels of radiation dissipation, the structure of subcritical eddy remains unaffected.

## 5.8 Anisotropy

To further quantify the shock and eddy interaction, and to study the impact of energy sinks on the disturbances' magnitude, the normal Reynolds stresses in 2-dimensions are considered in this section. In the lateral exchange of momentum and entrainment across the mixing layer, the only active component is the  $\overline{v'v'}$ . The  $\overline{u'u'}$  normal stress does not contribute to the entrainment across the mixing layer. On the anisotropy of compressible flow there have been discrepancies in literature. While several studies (e.g., Samimy & Elliott 1990, Pantano & Sarkar 2002) have suggested that the anisotropy, expressed in terms of longitudinal versus transverse velocity fluctuations, is relatively constant over different Mach numbers, others studies (e.g., Goebel & Dutton 1991; Gruber *et al.* 1993) have actually shown a growth with Mach number. In gravity driven, geometry-induced mixing layer across a cavity with high Reynolds number, by Karimpour & Chu (2012) and Wang *et al.* (2013), the lateral normal stress reportedly drops significantly as the Froude number of the main flow increases. The inconsistency in results makes it necessary to study the anisotropy in supercritical shallow mixing layers.

In this study the transition from linear to fully non-linear stage is studied. Therefore eddies and shocklets have not reached quasi-steady state. Figure 5–13 (a) to (c) show the evolution of normal Reynolds stresses in a subcritical eddy of  $Fr_c = 0.1$ . Since the mixing layer thickness also evolves in time, the distance from mixing layer ( $y$ ) is normalized by the thickness at any instance ( $4\delta_{\theta t}$ ). This keeps the intensity of disturbances mostly confined between -0.5 and 0.5 on the vertical axis. From  $t_1$  in Figure 5–13 (a) to  $t_3$  in Figure 5–13 (c) the intensity of  $\overline{v'v'}$  is mostly larger

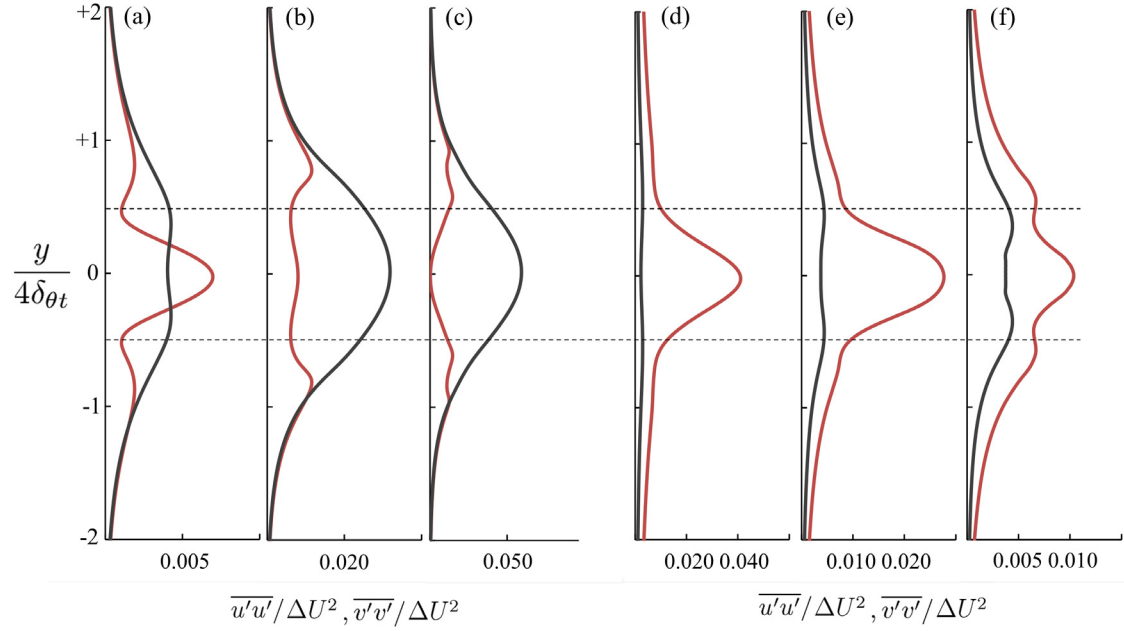


Figure 5–13: Distribution of normal Reynolds stresses,  $\overline{u'u'}$  (red lines) and  $\overline{v'v'}$  (black lines) for 3 stages of development of  $t_1$ ,  $t_2$  and  $t_3$  for  $Fr_c = 0.1$  in (a), (b) and (c) and  $Fr_c = 1.1$  in (d), (e) and (f).

than the intensity of  $\overline{u'u'}$ . Outside the mixing layer the disturbance approaches zero in the fully isotropic, mixing free region. However the same distribution in Figure 5–13 (d) to (e) for  $Fr_c = 1.1$ , suggests that across the mixing layer lateral normal stress is always smaller than longitudinal normal stress. Figure 5–14 shows the dependence of the relative averaged normal stresses to convective Froude number. As explained earlier the ratio of  $\overline{v'v'}/\overline{u'u'}$  is time and space dependant. In order to present the change of anisotropy with convective Froude number, the Reynolds stresses are averaged over the computational domain. The distribution of the normal stresses however is mainly across the mixing layer thickness as demonstrated in Figure

5–13. Therefore  $\overline{v'v'}$  and  $\overline{u'u'}$  mainly characterize the activities over the mixing layer. In Figure 5–14 the variation of the ratio of two averaged normal Reynolds stresses are plotted against convective Froude number. According to Figure 5–13, this distribution is also time dependant. In-order to express the time evolution of normal Reynolds stresses, the error bars over each Froude number represent the change of the anisotropy ratio in time from  $t_1$  to  $t_3$ . The strong change of the anisotropy tensor however cannot be compared to existing experimental or numerical data, since most of the existing data are reported in quasi-steady state. However the decreasing trend matches the trend observed in some existing experimental and numerical investigations including the results of Goebel & Dutton (1991); Freund *et al.* (2000) in gas dynamics and Karimpour & Chu (2012) in free surface shallow waters.

## 5.9 Conclusion

The transition of mixing layer from linear to non-linear instability is studied using DNS of shallow water equations. The numerical experiments cover convective Froude number of 0.1 to 1.4. The simulation revealed reduced growth rate for the transition which is in agreement with existing numerical and experimental data in temporally and spatially evolving mixing layers in gas dynamics. The total energy dissipation does not seem to impact the growth rate of the mixing layer thickness. However the growth rate is directly affected by the radiation which in disturbance kinetic equation operates as sink term. Furthermore total energy consideration suggests that this transition occurs with significant drop of total energy and rise of energy

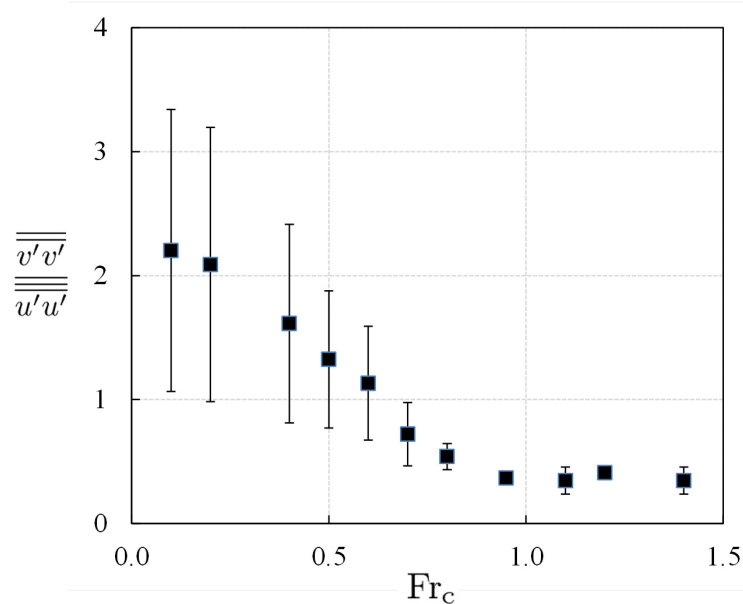


Figure 5–14: Variation of the ratio of normal averaged Reynolds stresses,  $\overline{\overline{v'v'}} / \overline{\overline{u'u'}}$  with convective Froude number.

flux. The hydraulic jumps extended from the eddy, appear in the mixing layer at intermediate Froude numbers starting from  $Fr_c \geq 0.7$ . Thus the eddy-shocklet pattern is observed even at transcritical convective Froude numbers, where the main stream Froude number and convective Froude number are subcritical. The analysis of the anisotropy on the other hand demonstrated a trend towards a highly anisotropic shocklet-eddy, when the flow is supercritical.

## CHAPTER 6 CONCLUSION

A robust finite volume method has been developed. This was to investigate the subcritical-to-supercritical transitions. The Weighted Essentially Non-Oscillatory scheme was implemented in this thesis which allowed the capture of flow discontinuity, without encountering either spurious oscillations or adding excessive numerical damping, which is detrimental to simulation of flow of complex patterns. The numerical accuracy was tested in mixing layer with eddy-shocklet interaction. The numerical accuracy achieved has shown significant improvement of WENO scheme over conventional TVD schemes. The numerical scheme can have infinite order but here designed to be spatially  $5^{th}$  order accurate, and locally drop to a minimum of  $3^{rd}$  order in case of discontinuity. As demonstrated in chapter 2 using WENO spatial reconstruction scheme, in the case of vortex-shocklet interaction, was reported to have an overall convergence rate of over 4. In the case of subcritical eddy, an order of nearly 5 has been reached. This has led to success in direct numerical simulations of a number of subcritical-to-supercritical transitions selected for investigation. The simulations of three problems have been validated by analytical solutions and available experimental data. These same computational problems have been mostly studied in subcritical regimes prior to this thesis. In the study of transverse dam-break waves, supercritical expansion fan was part of the solution in subcritical main flows. The

simulation results were expressed in terms of Ritter's similarity variable and validated with experimental data from Subramanya & Awasthy (1974) and Mizumura et al. (2003) in the subcritical and supercritical range.

In the study of linear instability, the direct numerical simulations have reproduced the classical results obtained using the normal mode approach. The direct numerical simulations have captured the modulation of the instability due to wave entrapment between the returning surfaces that are not describable by the normal mode approach. The extension of simulation from linear to non-linear instability also demonstrated substantial effects of compressibility on eddy structure and growth. Two kinds of energy dissipations in the non-linear development have been identified. Level of the radiation dissipation reduces gradually as the convective Froude number rises from 0.1 to 1.4. This is consistent with gradual reduction in mixing layer thickness growth rate. Moreover the eddy-shocklet structure appears once there is total energy dissipation through shocklets.

## **6.1 Contributions to Knowledge**

A reliable numerical method was developed for accurate and stable simulations of complex flows involved in supercritical to subcritical transitions. This method works equally well for subcritical and supercritical flows. Moreover this method has advantage over conventional approach in shallow flow simulations using the Riemann solver. It does not have the source term difficulty of the Riemann solver. Calculation can be carried out directly for flow over channel bottom topographic variation, without the modification of the numerical scheme. In addition to the development of the

reliable numerical method, the thesis has also made contributions to the modelling and analysis of high speed flows in interaction with low speed subcritical flow. To the best of our knowledge, the present investigation is the first comprehensive description of flow diversion from a main channel to the side using the Ritter's similarity variable covering a wide range of Froude numbers from subcritical to supercritical main flows. Furthermore, the direct numerical simulations have explained the hydrodynamic instability of shear flow beyond the range that can be analyzed by the classical method. Quantitative evaluation of energy dissipations due to wave radiation and formation of shock waves are given to explain the impact of compressibility on the development of non-linear instability.

## **6.2 Recommendations to Future Work**

In this thesis numerical method has been developed and applied to three supercritical to subcritical transitions in shallow flows. The extension of this method to non-uniform mesh with local refinement is the immediate future plan. Other future area of investigation is exploration of two phase flows simulations. In particular, our interest is to investigate the energy dissipation mechanism and air entrainment process associated with hydraulic jumps.

## REFERENCES

- [1] M. B. Abbott. An introduction to the method of characteristics. 1966.
- [2] N. J. Balmforth. Shear instability in shallow water. *Journal of Fluid Mechanics*, 387:97–127, 1999.
- [3] M. E. Barone, W. L. Oberkampf, and F. G. Blottner. Validation case study: Prediction of compressible turbulent mixing layer growth rate. *AIAA journal*, 44(7):1488–1497, 2006.
- [4] S. F. Birch and J. M. Eggers. A critical review of the experimental data for developed free turbulent shear layers. 1973.
- [5] W. Blumen, P. G. Drazin, and D. F. Billings. Shear layer instability of an inviscid compressible fluid. part 2. *J. Fluid Mech*, 71(2):305–316, 1975.
- [6] S. Bouhairie and V. H. Chu. Two-dimensional simulation of unsteady heat transfer from a circular cylinder in crossflow. *Journal of Fluid Mechanics*, 570:177–215, 2007.
- [7] P. Bradshaw. Compressible turbulent shear layers. *Annual Review of Fluid Mechanics*, 9(1):33–52, 1977.
- [8] G. L. Brown and A. Roshko. On density effects and large structure in turbulent mixing layers. *Journal of Fluid Mechanics*, 64(04):775–816, 1974.
- [9] C. E. Castro, E. F. Toro, and M. Käser. Ader scheme on unstructured meshes for shallow water: simulation of tsunami waves. *Geophysical Journal International*, 189(3):1505–1520, 2012.
- [10] V. H. Chu and R. E. Baddour. Turbulent gravity-stratified shear flows. *Journal of Fluid Mechanics*, 138:353–378, 1984.
- [11] V. H. Chu and C. Gao. False diffusion produced by flux limiters. *Computational Thermal Sciences*, 5(6), 2013.

- [12] V. H. Chu and G. H. Jirka. Surface buoyant jets and plumes. *Encyclopedia of fluid mechanics*, 6:1053–1083, 1986.
- [13] V. H. Chu and M. R. Vanvari. Experimental study of turbulent stratified shearing flow. *Journal of the Hydraulics Division*, 102(6):691–706, 1976.
- [14] A. Cortés, W. E. Fleenor, M. G. Wells, I. de Vicente, and F. J. Rueda. Pathways of river water to the surface layers of stratified reservoirs. *Limnol. Oceanogr*, 59(1):233–250, 2014.
- [15] G. de Vahl Davis. *Numerical methods in engineering & science*. Allen & Unwin London, 1986.
- [16] J. F. Debiève, P. Dupont, H. Laurent, M. Mena, and J. P. Dussauge. Compressibility and structure of turbulence in supersonic shear flows. *European Journal of Mechanics-B/Fluids*, 19(5):597–614, 2000.
- [17] P. G. Drazin and L. N. Howard. *Hydrodynamic stability of parallel flow of inviscid fluid*. Academic Press New Delhi, 1966.
- [18] J. B. Freund, Sanjiva K S. K. Lele, and P. Moin. Compressibility effects in a turbulent annular mixing layer. part 1. turbulence and growth rate. *Journal of Fluid Mechanics*, 421:229–267, 2000.
- [19] S. Fu and Q. Li. Numerical simulation of compressible mixing layers. *International journal of heat and fluid flow*, 27(5):895–901, 2006.
- [20] P. H. Gaskell and A. K. C. Lau. Curvature-compensated convective transport: Smart, a new boundedness-preserving transport algorithm. *International Journal for Numerical Methods in Fluids*, 8(6):617–641, 1988.
- [21] T. B. Gatski and J. P. Bonnet. *Compressibility, turbulence and high speed flow*. Academic Press, 2013.
- [22] R. Ghostine, J. Vazquez, A. Terfous, N. Riviere, A. Ghenaim, and R. Mose. A comparative study of 1D and 2D approaches for simulating flows at right angled dividing junctions. *Applied Mathematics and Computation*, 219(10):5070–5082, 2013.
- [23] S. G. Goebel and J. C. Dutton. Experimental study of compressible turbulent mixing layers. *AIAA journal*, 29(4):538–546, 1991.

- [24] M. R. Gruber, N. L. Messersmith, and J. C. Dutton. Three-dimensional velocity field in a compressible mixing layer. *AIAA journal*, 31(11):2061–2067, 1993.
- [25] A. Harten. High resolution schemes for hyperbolic conservation laws. *Journal of computational physics*, 49(3):357–393, 1983.
- [26] A. Harten, B. Engquist, S. Osher, and S. B. Chakravarthy. Uniformly high order accurate essentially non-oscillatory schemes, iii. *Journal of computational physics*, 71(2):231–303, 1987.
- [27] A. Harten, P. D. Lax, and B. V. Leer. On upstream differencing and godunov-type schemes for hyperbolic conservation laws. *SIAM review*, 25(1):35–61, 1983.
- [28] F. M. Henderson. Open channel flow, 1966.
- [29] A. J. Hogg and D. Pritchard. The effects of hydraulic resistance on dam-break and other shallow inertial flows. *Journal of Fluid Mechanics*, 501:179–212, 2004.
- [30] G. S. Jiang and C. W. Shu. Efficient implementation of weighted eno schemes. *Journal of computational physics*, 126(1):202–228, 1996.
- [31] S. Karimpour and V. H. Chu. Turbulence and waves in subcritical and supercritical shear flows. In *International Symposium on Shallow Flows*, 2012.
- [32] S. Karimpour and V. H. Chu. High-order interpolation schemes for capturing flow discontinuities. In *3rd International Conference on Computational Methods for Thermal Problems*, 2014.
- [33] S. Lee, S. K. Lele, and P. Moin. Eddy shocklets in decaying compressible turbulence. *Physics of Fluids A: Fluid Dynamics (1989-1993)*, 3(4):657–664, 1991.
- [34] B. Van Leer. Towards the ultimate conservative difference scheme. iv. a new approach to numerical convection. *Journal of computational physics*, 23(3):276–299, 1977.
- [35] S. K. Lele. Compressibility effects on turbulence. *Annual review of fluid mechanics*, 26(1):211–254, 1994.
- [36] B. P. Leonard. Universal limiter for transient interpolation modeling of the advective transport equations: the ultimate conservative difference scheme. *NASA Technical Memorandum*, 100916, 1988.

- [37] B. P. Leonard. The ultimate conservative difference scheme applied to unsteady one-dimensional advection. *Computer methods in applied mechanics and engineering*, 88(1):17–74, 1991.
- [38] B. P. Leonard and J. E. Drummond. Why you should not use hybrid, power-law or related exponential schemes for convective modelling there are much better alternatives. *International Journal for Numerical Methods in Fluids*, 20(6):421–442, 1995.
- [39] B. P. Leonard and S. Mokhtari. Beyond first-order upwinding: The ultra-sharp alternative for non-oscillatory steady-state simulation of convection. *International Journal for Numerical Methods in Engineering*, 30(4):729–766, 1990.
- [40] R. J. LeVeque. *Finite volume methods for hyperbolic problems*, volume 31. Cambridge university press, 2002.
- [41] H. W. Liepmann and A. Roshko. *Elements of Gasdynamics*. Courier Dover Publications, 2013.
- [42] J. A. Liggett. *Fluid mechanics*. McGraw-Hill Higher Education, 1994.
- [43] G. E. Likens. *Lake Ecosystem Ecology: A Global Perspective*. Academic Press, 2010.
- [44] C. C. Lin. On the stability of the laminar mixing region between two parallel streams in a gas. Technical report, DTIC Document, 1953.
- [45] X. D. Liu, S. Osher, and T. Chan. Weighted essentially non-oscillatory schemes. *Journal of computational physics*, 115(1):200–212, 1994.
- [46] L. M. Mack. On the inviscid acoustic-mode instability of supersonic shear flows. *Theoretical and Computational Fluid Dynamics*, 2(2):97–123, 1990.
- [47] S. Mahmodinia, M. Javan, and A. Eghbalzadeh. The flow field and free surface pattern of the submerged side weir with different lengths. *Arabian Journal for Science and Engineering*, 39(6):4461–4472, 2014.
- [48] R. W. Metcalfe, S. A. Orszag, M. E. Brachet, S. Menon, and J. J. Riley. Secondary instability of a temporally growing mixing layer. *Journal of Fluid Mechanics*, 184:207–243, 1987.

- [49] A. Michalke. On the inviscid instability of the hyperbolic tangent velocity profile. *Journal of Fluid Mechanics*, 19(04):543–556, 1964.
- [50] K. Mizumura, M. Yamasaka, and J. Adachi. Side outflow from supercritical channel flow. *Journal of Hydraulic Engineering*, 129(10):769–776, 2003.
- [51] J. Nycander and K. Döös. Open boundary conditions for barotropic waves. *Journal of Geophysical Research: Oceans (1978–2012)*, 108(C5), 2003.
- [52] C. Pantano and S. Sarkar. A study of compressibility effects in the high-speed turbulent shear layer using direct simulation. *Journal of Fluid Mechanics*, 451:329–371, 2002.
- [53] D. Papamoschou and A. Roshko. The compressible turbulent shear layer: an experimental study. *Journal of Fluid Mechanics*, 197:453–477, 1988.
- [54] C. E. Pinilla, S. Bouhairie, L. W. Tan, and V. H. Chu. Minimal intervention to simulations of shallow-water equations. *Journal of Hydro-environment Research*, 3(4):201–207, 2010.
- [55] C. E. Pinilla and V. H. Chu. Waves and bed-friction effect on stability of transverse shear flow in shallow waters. *Journal of Coastal Research*, pages 207–214, 2008.
- [56] A. Ritter. Die fortpflanzung der wasserwellen. *Zeitschrift Verein Deutscher Ingenieure*, 36(33):947–954, 1892.
- [57] P. L. Roe. Approximate riemann solvers, parameter vectors, and difference schemes. *Journal of computational physics*, 43(2):357–372, 1981.
- [58] P. L. Roe. Some contributions to the modelling of discontinuous flows. In *Large-scale computations in fluid mechanics*, volume 1, pages 163–193, 1985.
- [59] T. Rossmann, M. G. Mungal, and R. K. Hanson. Evolution and growth of large-scale structures in high compressibility mixing layers. *J. Turbulence*, 3(009):1–19, 2002.
- [60] M. Samimy and G. S. Elliott. Effects of compressibility on the characteristics of free shear layers. *AIAA journal*, 28(3):439–445, 1990.

- [61] N. D. Sandham and W. C. Reynolds. A numerical investigation of the compressible mixing layer, report no. TF-45, Thermosciences Division, Department of Mechanical Engineering, 1989.
- [62] N. D. Sandham and W. C. Reynolds. Compressible mixing layer-linear theory and direct simulation. *AIAA journal*, 28(4):618–624, 1990.
- [63] N. D. Sandham and W. C. Reynolds. Three-dimensional simulations of large eddies in the compressible mixing layer. *Journal of Fluid Mechanics*, 224:133–158, 1991.
- [64] T. Satomura. An investigation of shear instability in a shallow water. *J. Met. Soc. Japan*, 59:148–167, 1981.
- [65] C. W. Shu. Numerical experiments on the accuracy of eno and modified eno schemes. *Journal of Scientific Computing*, 5(2):127–149, 1990.
- [66] C. W. Shu. *Essentially non-oscillatory and weighted essentially non-oscillatory schemes for hyperbolic conservation laws*. Springer, 1998.
- [67] C. W. Shu. High order weighted essentially nonoscillatory schemes for convection dominated problems. *SIAM review*, 51(1):82–126, 2009.
- [68] C. W. Shu and S. Osher. Efficient implementation of essentially non-oscillatory shock-capturing schemes. *Journal of Computational Physics*, 77(2):439–471, 1988.
- [69] F. Stern, R. V. Wilson, H. W. Coleman, and E. G. Paterson. Comprehensive approach to verification and validation of cfd simulations part 1: methodology and procedures. *Journal of fluids engineering*, 123(4):793–802, 2001.
- [70] J. J. Stoker. *Water waves: The mathematical theory with applications*. 1957. Interscience, New York.
- [71] J. T. Stuart. On finite amplitude oscillations in laminar mixing layers. *J. Fluid Mech*, 29(Part 3):417–440, 1967.
- [72] K. Subramanya and S. C. Awasthy. Spatially varied flow over side-weirs. *Journal of the Hydraulics Division*, 98(1):1–10, 1972.
- [73] P. K. Sweby. High resolution schemes using flux limiters for hyperbolic conservation laws. *SIAM journal on numerical analysis*, 21(5):995–1011, 1984.

- [74] S. I. Takehiro and Y. Y. Hayashi. Over-reflection and shear instability in a shallow-water model. *Journal of Fluid Mechanics*, 236:259–279, 1992.
- [75] E. F. Toro. Riemann solvers and numerical methods for fluid dynamics: a practical introduction. 2009.
- [76] J. Vazquez, G. Kesserwani, and N. Riviere. Use of side-weir models and shallow water equations with TVD scheme for open channel bifurcations. In *11th International Conference on Urban Drainage*, Edinburgh, Scotland, 2008.
- [77] M. E. Vázquez-Cendón. Improved treatment of source terms in upwind schemes for the shallow water equations in channels with irregular geometry. *Journal of Computational Physics*, 148(2):497–526, 1999.
- [78] H. K. Versteeg and W. Malalasekera. *An introduction to computational fluid dynamics: the finite volume method*. Pearson Education, 2007.
- [79] A. W. Vreman, N. D. Sandham, and K. H. Luo. Compressible mixing layer growth rate and turbulence characteristics. *Journal of Fluid Mechanics*, 320:235–258, 1996.
- [80] C. B. Vreugdenhil. *Numerical methods for shallow-water flow*. Springer, 1994.
- [81] T. Wang, S. Karimpour, and V. H. Chu. Experimental study of the exchange process between the main flow and its side basin. In *35th IAHR World Congress*, 2013.
- [82] B. Yuan, J. Sun, D. Yuan, and J. Tao. Numerical simulation of shallow-water flooding using a two-dimensional finite volume model. *Journal of Hydrodynamics, Ser. B*, 25(4):520–527, 2013.